Analysis of Idle Power and Iron Loss Reduction in an Interior PM Automotive Alternator

by

Vlatka Životić-Kukolj

M.Eng.Sci. (Research) Electrical and Electronic Engineering,
Adelaide University, 2001

B.Eng (Hons) Electrical Power Engineering,
Zagreb University, 1986

Thesis submitted for the degree of

Doctor of Philosophy

in

School of Electrical and Electronic Engineering
University of Adelaide, Australia

2010

To my dear teachers…

Abstract

In recent years there has been considerable interest in high power automotive alternators. As part of earlier work, an interior permanent magnet machine had been built as a concept demonstrator for a 6 kW automotive alternator. Test results on this machine had shown good field-weakening performance but that the machine fell 16% short of the idle power requirement and had high iron losses.

This thesis describes the development of a finite-element model for this machine and how it was validated using experimental test results and used to examine the cause of the low idle power and high iron losses. A limited optimisation of the machine design to reduce iron losses was examined and demonstrated experimentally.

It was found that the cause of the low idle power was due to cross-saturation effects in the machine, particularly in the stator teeth. Both the finite-element analysis and experimental tests showed a substantial reduction in the *q*-axis inductance due to the presence of the magnet flux. It was predicted that the machine would have met the idle power requirement if saturation and cross-saturation had not been present.

The high iron loss during field-weakening was identified as being due to large amplitude, higher harmonic flux components caused by the interaction of the rotor barriers and the *d*-axis flux distribution. This was seen in the spatial airgap flux density and the time-varying stator tooth flux waveforms. The analysis also showed that eddy-current loss was dominant in this machine at higher speeds, and that under short-circuit conditions the majority of the iron loss was due to large thirteenth and eleventh harmonic flux density components. This was confirmed experimentally using the stator tooth flux waveforms and the total iron loss measurement.

A limited design optimisation was performed by examining three machine design changes to reduce the high stator iron loss under short-circuit conditions. Of these, increasing the stator slot opening using flat stator teeth offered the greatest calculated iron loss reduction (19%). This was tested experimentally by machining the stator teeth of the prototype machine. The measured iron loss reduction (21%) at high speed was comparable to the calculated effect, and the output power was shown to improve slightly.

The results of the detailed iron loss investigation in this thesis forms a basis for development for more general machine design approaches for reducing stator iron loss under field-weakening conditions in interior permanent magnet machines.

Statement of Originality

This work contains no materials which has been accepted for the award of any other degree or diploma in any university or other tertiary institution and, to the best of my knowledge and belief, contains no material previously published or written by another person, except where due reference has been made in the text.

I give consent to this copy of my thesis, when deposited in the University Library, being made available for loan and photocopying, subject to the provisions of the Copyright Act 1968.

I also give permission for the digital version of my thesis to be made available on the web, via the University's digital research repository, the Library catalogue, the Australasian Digital Theses Program (ADTP) and also through web search engines, unless permission has been granted by the University to restrict access for a period of time.

Signed Date: 5 March 2010

Acknowledgments

I would like to express my deepest gratitude and appreciation to my supervisors Dr Wen L Soong and Associate Professor Nesimi Ertugrul for their guidance, support and understanding throughout the progress of this project.

I would also like to thank C.Z. Liaw, D.M. Whaley, and the staff of the School of Electrical and Electronic Engineering's mechanical workshop for their technical support during the experimental testing and Professor T.J.E. Miller of the University of Glasgow for provision of the Polycor lamination data.

I would like to express my appreciation to all my friends and colleagues in the Power and Control System Group for their warm support and enjoyable company.

I would like to thank and express my deepest gratitude to all my dear teachers from my primary, secondary and tertiary education without whose help I would never be able to reach this educational level. I am deeply in debt to all of you and no money on this planet could pay for your contribution.

Lastly but not the least I would like to thank to my parents, my husband Radan and my daughters Dahlia and Nica for their love, patience and support.

Publications

V. Zivotic-Kukolj, W.L. Soong, N. Ertugrul, "Modelling of Saturation and Cross-Saturation Effects in an Interior PM Automotive Alternator," *Australasian Universities Power Engineering Conference (AUPEC 2004), Brisbane, Australia,* Sep-Oct 2004.

V. Zivotic-Kukolj, W.L. Soong, N. Ertugrul, "Investigation of Iron Losses in a High Flux Interior PM Automotive Alternator," *Australasian Universities Power Engineering Conference (AUPEC 2004), Brisbane, Australia,* Sep-Oct 2004.

V. Zivotic-Kukolj, W.L. Soong, N. Ertugrul, "Modelling of Saturation and Cross-saturation Effects in an Interior PM Automotive Alternator," *Australian Journal of Electrical and Electronics Engineering,* Vol 2, No 3, pp. 209 - 216, 2005.

V. Zivotic-Kukolj, W.L. Soong, N. Ertugrul, "Iron Loss Reduction in an Interior PM Automotive Alternator," *Conference Record of Industrial Application Society (IAS 2005), Hong Kong, China,* Vol 3, pp. 1736 – 1743, Oct 2005.

V. Zivotic-Kukolj, W.L. Soong, N. Ertugrul, "Iron Loss Reduction in an Interior PM Automotive Alternator," *IEEE Transactions on Industrial Applications,* Vol 42, No 6, pp. 1478 - 1486, Nov – Dec 2006.

Nomenclature

a, b	constants dependent on thickness and type of ferromagnetic material;
a_n, b_n	harmonic coefficients;
A_m	magnet area [mm^2];
A_{slot}	slot area [mm^2];
$B(t)$	flux density [T];
B_{pk}	peak value of flux density [T];
$B_{pk\,n}$	magnitude of n-harmonic component of the magnetic flux density [T];
B_r	equivalent remanence [T];
$B_r(t)$	radial component of the flux density [T];
$B_t(t)$	tangential component of the flux density [T];
C_e	eddy-current loss coefficient for sinusoidal flux density waveforms;
C_{e1}	eddy-current loss coefficient for arbitrary-shaped flux density waveforms;
C_h	hysteresis loss coefficient;
C_i	capacitance of the low-pass filter;
DC	direct current;
$e(t)$	induced search-coil voltage [V rms];
E	induced EMF due to magnets [V rms];
f	frequency [Hz];
$\varphi(t)$	flux in a tooth [Wb];
Ψ_m	magnet flux-linkage [Vs rms];
$g(t)$	periodic function of t with a period of T;
g"	effective air gap [mm];
γ	angle between the stator phase current phasor and q-axis;
$H(t)$	magnetic field [Wb];
$i(t)$	instantaneous current waveform [A];
$i_1(t)$	instantaneous current [A];
I	stator phase current [A rms];
I_d	d-axis component of stator phase current [A rms];
I_q	q-axis component of stator phase current [A rms];
I_0	rated phase current [A rms];

L	inductance [mH];
L_d	*d*-axis synchronous inductance [mH];
$L_{d(sat)}$	saturated value of the *d*-axis synchronous inductance [mH];
$L_{d(unsat)}$	unsaturated value of the *d*-axis synchronous inductance [mH];
L_{dmi}	intrinsic *d*-axis inductance [mH];
L_{end}	end winding inductance [mH];
L_m	magnetising inductance [mH];
L_q	*q*-axis synchronous inductance [mH];
$L_{q(sat)}$	saturated value of the *q*-axis synchronous inductance [mH];
$L_{q(unsat)}$	unsaturated value of the *q*-axis synchronous inductance [mH];
L_{slot}	slot-leakage inductance [mH];
λ_a	flux-linkage in phase *a* [Vs rms];
λ_b	flux-linkage in phase *b* [Vs rms];
λ_c	flux-linkage in phase *c* [Vs rms];
λ_{ph}	total flux-linkage per phase [Vs rms];
$\lambda(t)$	instantaneous flux linkage [Vs rms];
m	number of phases;
n	Steinmetz exponent (typically 1.6, but can vary between 1.6 and 2.3);
N	number of turns in the search coil;
ω	electrical angular speed [rad/s];
p	pole-pairs;
PM	permanent magnet;
P_{Cu}	copper loss [W];
P_e	eddy-current loss [W];
P_{Fe}	iron loss [W];
P_h	hysteresis loss [W];
P_{in}	input power [W];
P_{Mech}	mechanical loss [W];
P_{out}	output power [W];
R	resistance of the phase winding [Ω];
R_a	armature resistance or stator resistance per phase [Ω];
R_i	resistance of the low-pass filter [Ω];
$R_i\ C_i$	time constant of the low-pass filter;
t	time [sec.];

T	output phase torque [Nm];
Θ	rotor angle [rad];
$v(t)$	instantaneous voltage waveform [V];
$v_i(t)$	output of the integrator [V];
V	stator phase voltage [V rms];
V_0	rated phase voltage [V rms];
V_d	*d*-axis component of stator phase voltage [V rms];
V_q	*q*-axis component of stator phase voltage [V rms];

Contents

List of Figures

List of Tables

Chapter 1 Introduction

1.1 Increasing Automotive Electrical Power Needs

Proposed new features in cars such as active suspension systems and electro-mechanical valves have meant that the existing automotive alternator cannot satisfy the growing electrical power demands [1]. Table 1-1 presents the typical types of loads causing the rise in electrical power demands.

Table 1-1 Examples of the types of load causing the rise in electrical power demands [2].

NOTE:
This table is included on page 1 of the print copy of the thesis held in the University of Adelaide Library.

The automotive industry is currently looking into the development of low-cost high-power alternators in order to satisfy these projected electrical power demands of new-generation vehicles. A proposed specification for a high-power belt-driven automotive alternator is presented in Figure 1-1 assuming a 3:1 belt ratio [3]. It shows a linearly increasing output power from 4 kW to 6 kW as the alternator's speed increases from idle (1.8 krpm) to maximum operating speed (18 krpm). This is an extremely wide constant power speed range (CPSR) of 10:1. The new alternator should have high efficiency, the specification is for a 75% shaft-to-output efficiency, which is significantly higher than the 50% to 60% obtained with conventional alternators. It is also desirable to have low torque pulsations to minimize vibration and audible noise [4]

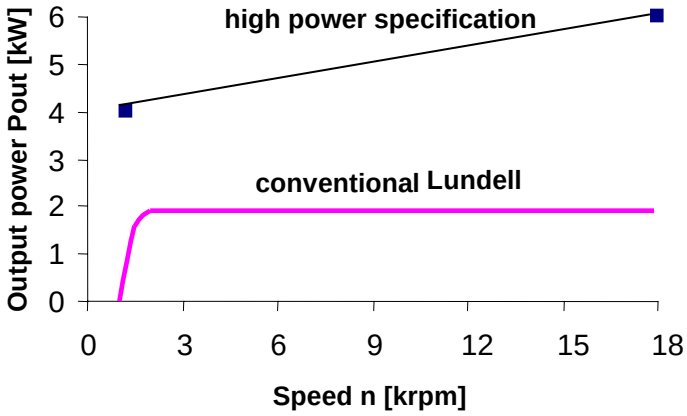

Figure 1-1 Output power characteristics versus speed of a typical Lundell alternator also showing the new high power specification.

The higher alternator output power will require an increase in the automotive electrical system voltage. It is commonly accepted that the maximum alternator output current should not exceed 150 A to limit copper losses and keep the cross-section area of the copper conductors to a reasonable value. Table 1-2 shows the maximum output powers for different combinations of DC load voltages and DC load currents. The present 14 V automotive system can carry about 2 kW with this limitation. To achieve the desired 6 kW of output power while keeping the current at 150 A will require a system voltage of at least 42 V.

Table 1-2 Maximum output power obtained with different combinations of DC load voltages and DC load currents.

Maximum value of DC load voltage [V]:	**Maximum value of DC load current [A]:**	**Maximum value of DC load output power [kW]:**
14	150	2.1
14	450	6.3
28	150	4.2
42	150	6.3

1.2 Higher Power Alternators

The most widely used automotive alternator is the Lundell (or clawpole-rotor) alternator. Figure 1-3 shows its constructional details. The rotor construction is relatively simple. It consists of a single coil enclosed between two iron pieces in the shape of claws forming the required

number of rotor poles. The DC field current produces a rotor electromagnetic field similar to the magnetic field of a permanent magnet. The stator has a standard three-phase stator winding.

NOTE:
This figure is included on page 3 of the print copy of the thesis held in the University of Adelaide Library.

Figure 1-2 Construction of the Lundell clawpole-rotor alternator [5].

Figure 1-3 presents a simplified circuit of an automotive alternator. When the rotor rotates it will induce AC voltages in the stator windings, and AC currents will flow in the 3-phase full-wave rectifier. The purpose of this rectifier is to convert the AC currents from the alternator into DC. The DC load voltage is monitored by a voltage regulator. If the DC voltage across the load increases, the voltage regulator decreases the value of the rotor field current and vice-versa.

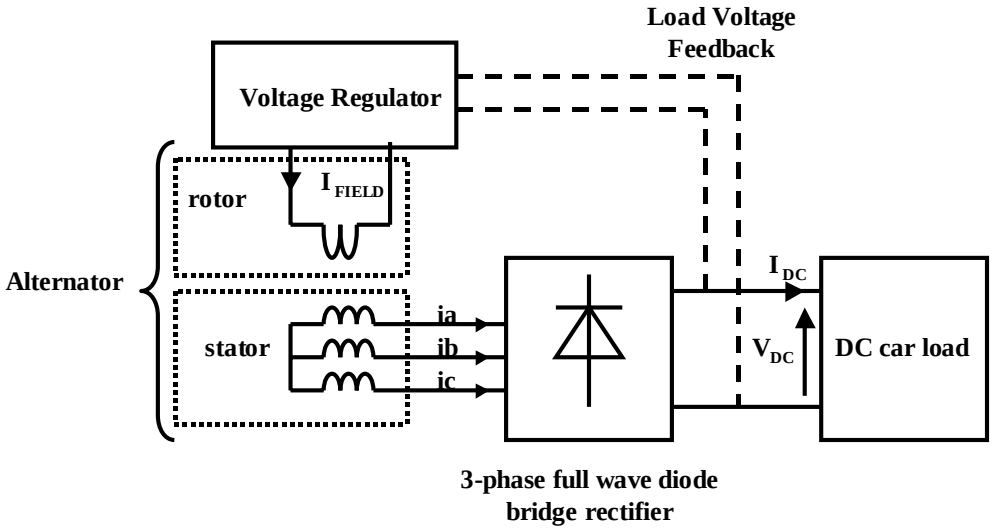

Figure 1-3 Simplified automotive alternator circuit.

The major advantages of this kind of alternator are its robust rotor design, low production cost and wide constant output power range. Its disadvantages include relatively poor efficiency (typically a maximum of 65%), limited output power at idle speed and limited life due to the use of slip-rings.

Figure 1-1 also showed the output power versus speed characteristic of an average Lundell alternator. It can develop a maximum output power of about 2 kW. It is not practical to design a Lundell alternator to the desired 6 kW output level due to scaling issues with the clawpole configuration and its poor efficiency.

Recently, research has been performed to find candidates to replace the Lundell alternator. Four different types of machines have been mainly considered:

1. Induction machine,
2. Switched-reluctance machine,
3. Surface permanent magnet machine and
4. Interior permanent magnet machine.

Induction machines are well understood and have relatively low production costs. Their main issue for this application is their limited constant-power speed range which is normally in the range 2:1 to 4:1. A design showing a 5:1 constant-power speed range (between 0.8 krpm and 4 krpm) at 4 kW constant output power has been demonstrated in [6] however this is still substantially below the 10:1 specification.

Switched-reluctance machines feature a low-cost rugged rotor construction and the potential to achieve wide constant-power speed ranges [7]. Issues include maintaining low output torque pulsations over a wide speed range, the requirement for thin laminations at high speeds, and their non-standard power electronic switch configuration. The torque ripple can be reduced by increasing the number of phases but this will increase the inverter cost [8].

Surface permanent magnet machines offer high efficiency and torque density but generally do not have wide field-weakening ranges due to the low inductance associated with their large effective magnetic air gap. Additional electronics such as a DC/DC converter can be used to vary the inverter DC link voltage to extend the field-weakening range however this increases the system cost and the losses [9, 10].

Interior permanent magnet machines are an attractive candidate for the high power automotive alternator due to their inherent capability for wide field-weakening operation. These machines use a combination of both magnet and reluctance torque and so can have high torque density [11]. Lovelace et al. examined the design of a high-power multiple-barrier interior PM alternator which could also act as a starter motor. They studied the modelling of magnetic saturation, and the machine and inverter costs optimization [12, 13, 14, 15]. At the same time Stumberger et al. [16, 17] performed the iron loss analysis on the single-barrier interior PM

machine. Later, in [18] a finite-element method based design and analysis were performed on an interior PM assisted multiple-barrier synchronous reluctance machine. Whether the machine has greater reluctance nature or permanent magnet nature depends on the rotor flux barrier geometry and amount of permanent magnet in the machine.

1.3 Concept Demonstrator Machine

The concept demonstrator is a high-flux multiple-barrier interior PM machine which uses rare-earth magnets (NdFeB). The machine is based on a commercial 415 V, 2.2 kW, 4 pole induction motor stator and uses a custom-designed rotor. A full description of its design will be presented in Chapter 2. Note that no finite-element analysis had been done previously on this machine during the design process.

Prior tests [19, 20] have shown two key issues with the machine with regards to the high power automotive alternator specification. Firstly, it did not meet the 4 kW idle power specification, this is thought to be due to a high degree of saturation and cross-saturation in this machine. Secondly, high iron losses under high-speed, field-weakening conditions were measured.

This thesis seeks to address these two issues using the following process:

- a finite-element model for the machine will be developed, and validated using the measured back-EMF, inductance saturation curves and performance characteristics;
- the finite-element model will be used to explore saturation and cross-saturation effects on the output power characteristic particularly in the idle-speed region, and
- the reason for the high iron losses at high speeds will be investigated along with methods for reducing these.

1.4 Literature Review and Problem Formulation

According to their rotor construction, permanent magnet (PM) machines are classified as either a surface or an interior PM machine [21]. Only interior PM machines will be considered here as surface PM machines are generally not suitable for wide field-weakening operation.

Interior PM machines are further differentiated into single-barrier and multiple-barrier types as mentioned previously in Section 1.2. One of the first examples of interior PM machines was the line-start, three-phase, single-barrier machine. It appeared in the late 1970’s and was a

modified form of a squirrel-cage induction machine with the aim of achieving higher efficiency [22]. Due to major developments in power electronics, variable-speed drives were then introduced which eliminated the need for the squirrel-cage and thus allowed greater optimization of the rotor geometry. Multiple-barrier interior PM machines have been introduced more recently. Their advantage lies in their higher saliency ratio and hence generally better performance, while the drawback is their relatively complex rotor structure which may lead to increased manufacturing costs.

Recent works related to interior PM machines have discussed the effect of saturation and cross-saturation effects on their performance [23–34]. Saturation is the phenomenon where current (or magnet flux) in the *d*- or *q*-axis reduces the inductance in the same axis, while cross-saturation is the phenomenon where flux in one axis produces a drop of the inductance in the other axis. Both phenomena depend on the non-linear *B*-*H* characteristic of the ferromagnetic material and the rotor and stator geometry.

The literature on saturation and cross-saturation in interior PM machines is largely focussed on several main areas:

- lumped-circuit and finite-element modelling methods for taking into account cross-saturation in the machine design and analysis [26, 27, 31];
- control algorithms to maximise the output torque and efficiency in the presence of cross-saturation [23, 24, 25, 28, 29, 32]; and
- the effect of cross-saturation on the performance of sensorless position control algorithms [30].

An example of the modelling methods is given in [34] where the analysis was focused on a modification of the conventional *d*/*q*-axis machine model in order to include the influence of cross-saturation by using current-dependent cross-coupling inductances. The model was evaluated experimentally on a single-barrier interior PM machine and a comparison of the finite-element derived model and the experimental results was performed. It was shown that in both axes, the cross-coupling inductance in some operating points can reach 20% to 40% of the self-inductance values. This will result in a significant impact on the machine performance.

In this thesis it is proposed to use finite-element analysis to investigate the influence of saturation and cross-saturation effects on the output power characteristic particularly at the idle speed. It is also proposed to investigate iron loss which is another significant concern for interior PM machines.

The presence of high iron losses in interior PM machines under field-weakening conditions was firstly analysed by Schiferl and Lipo [22]. They found that the air gap flux was very non-sinusoidal due to the combination of magnet flux harmonics and the armature MMF. Using finite-element analysis it was shown that these harmonic fields had a significant influence on stator core losses. They concluded that the air gap flux distortion is caused by the local saturation of rotor leakage flux paths due to the non-magnetic rotor flux barriers at low flux values (field-weakening conditions). As these barriers are necessary to force the magnet flux across the air gap to the stator, they concluded that the presence of high stator core harmonic fields are likely to be found in all interior PM machines.

Later researchers found similar results that the high iron losses in interior PM machines are caused by presence of high frequency harmonics in the air gap flux density waveform due to the rotor anisotropy. As the loss is due to harmonics, these iron losses are almost independent of the magnitude of the fundamental component of the air gap flux. The harmonic losses are strongly affected by the rotor geometry [35, 36]. As expected, it was found that the iron losses under field-weakening operation significantly increase with rotor speed and hence frequency [16, 22].

Significant research has been performed into the reduction of iron losses while preserving the maximum torque capability. In [37], an optimization process is described for the shape of the ends of the rotor barriers. Nearly 50% iron loss reduction was obtained without a significant drop of the maximum torque capability.

Han et al. [38, 39] described the trade-off between the reduction of iron losses and torque ripple for interior PM machines. It was shown that optimising the rotor design and the number of stator slots can produce significant reduction of iron losses in the machine, but was accompanied by increased torque ripple. In particular the use of fractional-slot distributed windings was proposed.

This concept of iron loss optimisation was subsequently investigated by a number of other researchers. Bianchi et al. [35] investigated changing the angular position and thickness of the rotor barriers on a single-barrier interior PM machine rotor. Seo et al. [40] compared integer versus fractional-slot distributed winding designs for a machine with a two-barrier rotor and found the total iron losses in the machine increased in the fractional-slot design. Pellegrino et al. [41] found that the number of stator to rotor slots should not be too different ($\left| n_s - n_r \right| > 2$) for low torque ripple and neither too close for low core losses.

The above researchers have examined optimising the stator and rotor geometry. Soong et al. [42] took a different approach by varying only the number of stator winding turns and magnet remanent flux density. They showed a trade-off between the high-speed iron losses versus low-speed current rating for a wide field-weakening range traction application.

In the above papers, generally the iron loss calculations are based on the finite-element method using information about the local flux density variation in each motor component [16,17, 18]. The total iron loss is calculated as the sum of the hysteresis, eddy-current, and in some cases excess/rotational losses obtained for each element over a full cycle of magnetic field variation in all parts of the machine iron [16]. The accuracy of the obtained results depends heavily on knowledge of accurate machine dimensions (in particular, the air gap) and material characteristics such as: the remanent magnetic induction B_r of the magnets and *B*-*H* characteristic of the laminated iron alloy used in the rotor/stator construction.

1.5 Key Contributions/Thesis Layout

The key contributions of this thesis are based on the detailed finite element modeling and experimental verification using the concept demonstrator prototype of:

- the saturation and cross-saturation effects on the idle power characteristics and
- the high iron loss during high-speed field-weakening operation.

In addition, the effect of three minor design changes on the iron loss was examined using finite-element analysis. The use of flat stator teeth (open stator slots) was found to be the most promising. This was tested experimentally and a significant iron loss reduction was obtained.

This thesis is organized as follows:

Chapter 1 presents an introduction and the problem definition related to the high power interior PM automotive alternator.

Chapter 2 covers related theory, test procedures and summarises the preliminary experimental findings of the concept demonstrator machine.

Chapter 3 describes the creation of the finite-element model and examines comparisons between the calculated and measured values of: back EMF, inductances in *d*- and *q*-axis, and the idle power of the interior PM prototype machine.

Chapter 4 uses the finite-element model to perform an iron loss analysis of the concept demonstrator machine. It includes background theory of the iron losses, comparison of the

measured and calculated tooth flux waveforms under open- and short-circuit conditions, calculation of iron loss in the stator teeth, and comparison with measured total losses.

Chapter 5 examines the effect of three minor changes to the concept demonstrator design on its open-circuit and field-weakening iron losses with the aid of finite element analysis. The design that achieves the most iron loss reduction (flat stator teeth) is further compared to the concept demonstrator results.

Chapter 6 describes the experimental modification of the stator laminations and the obtained measurements in order to confirm the iron loss reduction.

Chapter 7 summarises the key contributions and findings.

Chapter 2 Theory and Testing of Interior PM Prototype Machine

The previous chapter provided a brief overview of the design and development of automotive alternators and examined the different machine types capable of satisfying the modern car's high power demands. A literature review revealed the interior PM machine is the most suitable machine capable of satisfying such demands and discusses its design limitations. In this chapter, the modelling of the interior PM machine is presented, followed by a description of the concept demonstrator machine design and initial experimental findings including the detailed experimental testing procedures used in this and later chapters.

2.1 PM Machine Modelling

The conventional per-phase voltage and torque equations for the interior permanent magnet machine can be obtained from the phasor diagram presented in Figure 2-1,

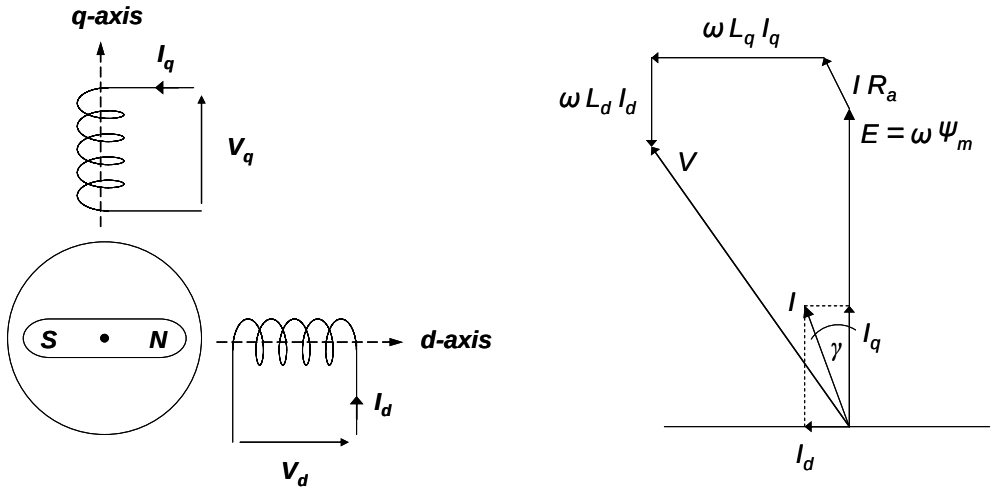

Figure 2-1 Interior permanent magnet machine phasor diagram.

where:

E	induced EMF due to magnets [V rms];
I	stator phase current [A rms];
R_a	armature resistance or stator resistance per phase [Ω];
L_d	*d*-axis synchronous inductance [H];
L_q	*q*-axis synchronous inductance [H];
V	stator phase voltage [V rms];
Ψ_m	magnet flux-linkage [Vs rms]

ω electrical angular speed [rad/s];

γ angle between the stator current phasor and *q*-axis;

The conventional per-phase *d*- and *q*-axis voltage equations can thus be found as:

$$V_d = - \omega L_q I_q + R_a I_d \quad (2\text{-}1)$$

$$V_q = \omega L_d I_d + \omega \Psi_m + R_a I_q \quad (2\text{-}2)$$

where:

V_d *d*-axis component of stator phase voltage [V rms];

V_q *q*-axis component of stator phase voltage [V rms];

I_d *d*-axis component of stator phase current [A rms];

I_q *q*-axis component of stator phase current [A rms];

The phase current *I* and phase voltage *V* should be smaller than the rated output phase current I_o and rated voltage V_o:

$$I = \sqrt{I_d^2 + I_q^2} \le I_0 \quad (2\text{-}3)$$

$$V = \sqrt{V_d^2 + V_q^2} \le V_0 \quad (2\text{-}4)$$

Note that the rated current depends on the motor winding thermal limit and the power electronic switch ratings, while the rated voltage is constrained by the motor winding insulation limit and the inverter DC bus voltage.

The output torque of the interior PM machine in terms of I_d and I_q is given by:

$$T = m p [\Psi_m I_q - (L_q - L_d) I_d I_q] \quad (2\text{-}5)$$

where:

m number of phases;

p number of pole-pairs;

From the phasor diagram it can be seen that the *d*-axis current is:

$$I_d = - I \sin \gamma \quad (2\text{-}6)$$

while the *q*-axis current is:

$$I_q = I \cos \gamma. \quad (2\text{-}7)$$

If equations (2-6) and (2-7) are substituted in the torque equation (2-5), this will result in the output torque being expressed in terms of *I* and γ (for a four-pole, three-phase machine):

$$T = 3 \times 2 \times \left[\psi_m I \cos\gamma - \frac{1}{2}\left(L_d - L_q\right) I^2 \sin 2\gamma \right] \quad (2\text{-}8)$$

In general it is desirable to operate the alternator to produce the maximum output power (and hence torque) at any speed, while keeping within the rated output current and voltage limits. At low speeds, the machine is operated with rated current I_0, at the current angle γ which produces the maximum torque. This is found using equation (2.8) however saturation has to be considered due to the fact that L_d is a function of I_d and L_q is a function of I_q. For each value of current angle γ, the stator currents in the *d*- and *q*-axes can be calculated from (2-6) and (2-7). By using the *d*- and *q*-axis inductance curves for the specific values of I_d and I_q, the inductances L_d and L_q can be found and their values substituted in equation (2-5) to calculate the torque. The above discussion considers saturation of an axis inductance due to current flowing in the same axis. Cross-saturation effects can also occur, where the axis inductance is affected by the current in the other axis. Thus in general, L_d and L_q are each a function of both I_d and I_q. This is discussed further in Section 3.3.

As the speed increases, the rated voltage limit becomes important and it will be necessary to increase the current angle to keep the terminal voltage within the required rated voltage limit. This will reduce the torque but not necessarily the output power as the speed is also increasing.

Once the torque is determined, the electrical output power for that speed can be obtained using the power-factor angle ϕ as:

$$P_{out} = mVI\cos\phi \quad (2\text{-}9)$$

This method of obtaining the maximum output power at a given speed will be used in Chapter 3 for calculating the output power at the idle speed.

2.2 Concept Demonstrator Machine Design

The concept demonstrator interior PM machine was designed by Soong et al. and preliminary testing performed earlier [19, 43, 44]. The machine is based on a commercial 415 V, 2.2 kW, 4 pole induction motor stator (see Figure 2-2a) and uses a custom-designed rotor (see Figure 2-2b). The rotor endplates have numerous holes to allow the rotor barriers to be filled with epoxy after assembly to prevent any movement of the rotor magnets.

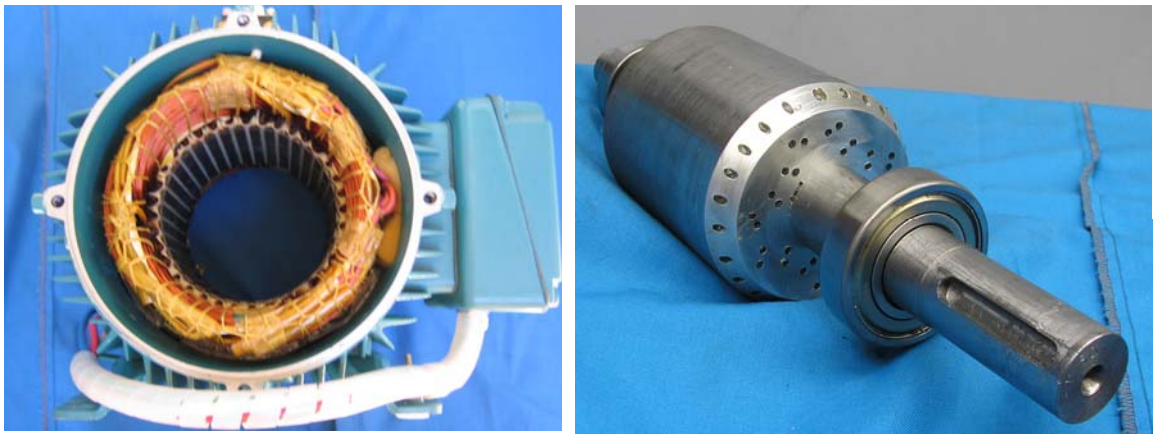

(a) (b)

Figure 2-2 a) Stator and b) rotor of the interior PM alternator.

A quarter of the rotor and stator lamination cross-section showing the location of the rare-earth rotor magnets is shown in Figure 2-3. The rotor has three flux-barriers per pole. Each rotor pole has ten small circular slot bridges which mechanically retain the magnets at high speed.

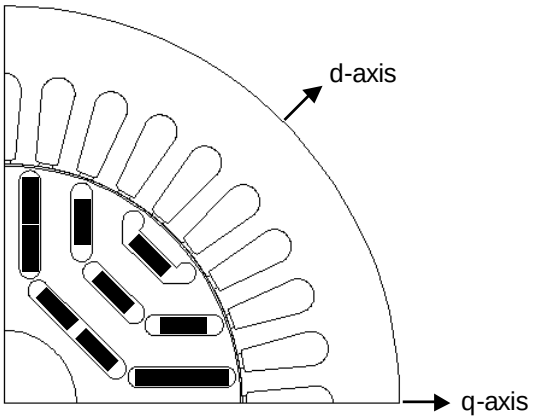

Figure 2-3 A quarter of rotor and stator lamination cross-section showing the location of the rare-earth rotor magnets.

The motor stack length is 95 mm, the stator outer diameter is 153 mm, the rotor diameter is 92 mm, and the air gap is 0.39 mm. The commercial induction machine stator used Polycor laminations. The custom-made rotor was constructed from Lycore 150 laminations due to the unavailability of Polycor. The detailed design information of the stator is presented in Table 2-1, and for the rotor in Table 2-2. The stator winding was a star-connected, single-layer concentric winding with 47 turns per coil.

Table 2-1 2.2 kW induction motor stator design information [44]

NOTE:
This table is included on page 14 of the print copy of the thesis held in the University of Adelaide Library.

Table 2-2 Design information for the three-barrier rotor.

Rotor Parameters	**Value**
Barriers per pole	3
Barrier thickness	4 mm
Inter-barrier iron thickness	6 mm
Lamination material	Lycore 150, 0.5 mm thick
Thickness of rotor bridges	0.6 mm

Originally the rotor was designed for ferrite magnets. It was tested initially as a pure reluctance machine as shown in Figure 2-4a and then with ferrite magnets as in Figure 2-4b. At a later stage the ferrite magnets were replaced with rare-earth magnets (NdFeB, grade N30) as shown in Figure 2-4c.

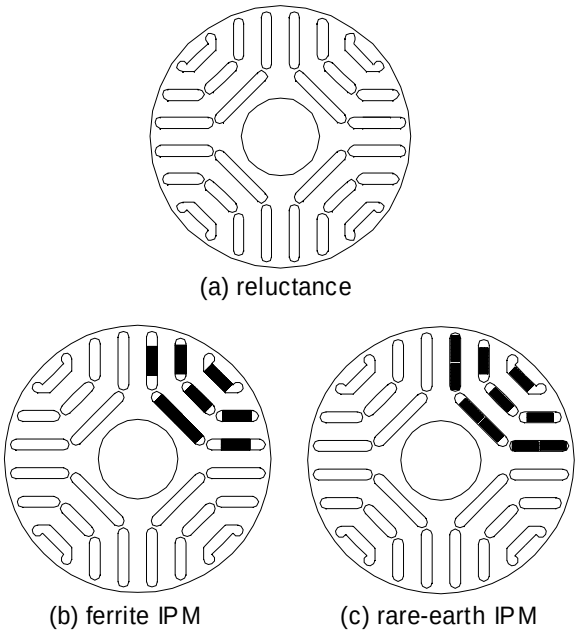

Figure 2-4 Cross-sections of the reluctance, ferrite and rare-earth PM rotors.

Table 2-3 Comparison of the properties of the three rotors.

Property	**Reluctance**	**Interior PM Ferrite**	**Interior PM NdFeB**
Magnet remanent flux density	-	0.4 T	1.1 T
Magnet dimensions	-	4 x 10 x 25 mm	3 x 9 x 20 mm
Magnets per pole	-	8	10
Magnet cross-sectional area per pole	-	320 mm^2	270 mm^2
Line back-EMF at 1,500 rpm	0V	83 V	271 V

From Table 2-3 it can be seen that the ferrite PM rotor uses 8 magnets per pole, while the rare-earth PM rotor uses ten smaller magnets per pole and has a somewhat smaller total magnet volume. Despite the smaller magnet volume, the higher flux density of the rare-earth magnets resulted in over three times the back-EMF voltage (271 V versus 83 V). The back-EMF is directly proportional to the air gap flux under open-circuit conditions. The air gap flux is equal to the flux produced by the rotor magnets, minus the rotor leakage flux. The rotor leakage flux is associated with the saturation of the rotor bridges and to a first approximation can be assumed to be fixed in magnitude. Thus doubling the magnet flux can result in a more than double increase in the air gap flux, and hence the back-EMF amplitude. The characteristics of the different rotor

types including the effect of cross-saturation on their inductance curves will be examined in Chapter 3.

The stator was constructed from 0.5 mm Polycor 0.3% silicon-iron laminations whose B-H curve is shown in Figure 2-5 [45]. The numerical values are provided in Appendix A. The rotor was constructed from 0.5 mm Lycore 150 laminations. Although the B-H curve for this material was not available, the Polycor B-H curve was used for the rotor. The assumption was made that both BH curves are similar. Later it was shown in Chapter 3 that the most saturated parts of the machine were the stator teeth and hence the BH curve for the rotor iron does not substantially affect the results. The loss data for Polycor was also provided in Appendix A. The loss data for Lycore 150 is not important as rotor losses were covered by this thesis.

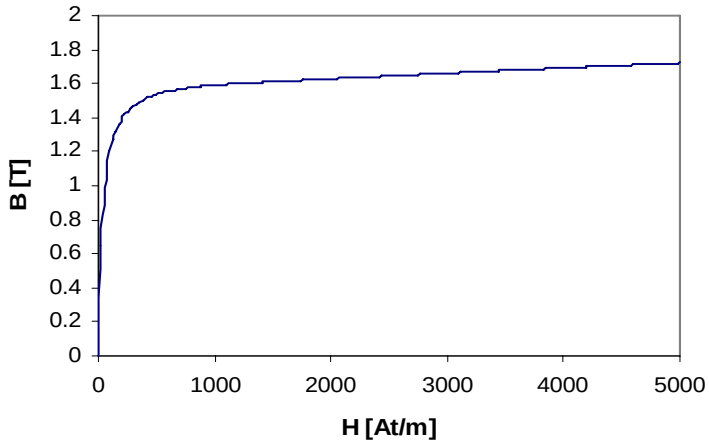

Figure 2-5 B-H curve of Polycor 0.3% silicon iron laminations used in the rotor and stator FEA modelling.

2.3 Concept Demonstrator Experimental Testing Procedure

The basic experimental test arrangement for the interior permanent magnet alternator is presented in Figure 2-6. The interior PM concept demonstrator is driven by two 5 kW, 1.5 krpm DC motors through a belt drive with adjustable gear ratios of 1:1, 1:2, and 1:4 which gave a maximum speed of 6 krpm.

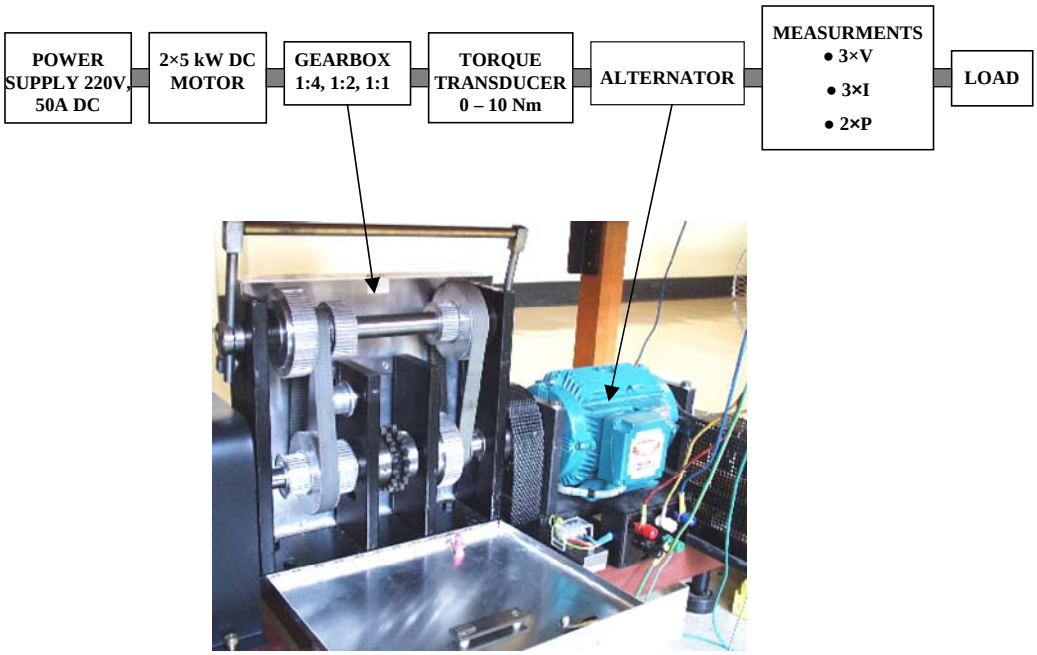

Figure 2-6 Basic experimental set-up for the interior permanent magnet alternator.

A 220-V/50-A variable DC power supply was used to drive the DC motors. The alternator torque was measured using a 25 Nm reaction torque transducer. The electrical instrumentation included: three voltmeters measuring the alternator output phase voltages, three ammeters measuring the line currents and two wattmeters measuring the total electrical power output. For the simulation of the electrical load on the alternator, three symmetrical variable-resistance load banks are connected to the alternators terminals.

2.3.1 Inductance Testing Procedure

Figure 2-7 presents the experimental set-up used for the *d*-axis and *q*-axis inductance measurements [46]. Ammeters are placed in series with each of the three machines phases. Two of the phases are connected together and the machine is driven by a single-phase 240 V autotransformer. To find the *d*- and *q*-axes of the machine, a low AC voltage is applied and the shaft of the machine is adjusted in position such that ammeters in the phases which are connected together read equal values. For a constant input voltage, the measured currents reach their maximum equal value for the specific rotor position when the *d*-axis inductance is measured; while the minimum equal value of the current belongs to the specific rotor position for the *q*-axis inductance measurement.

The rotor is positioned in the desired axis and clamped. The applied voltage is then set to such a value that gives the desired value of the stator peak current for both the *d*- and *q*-axis inductance measurements.

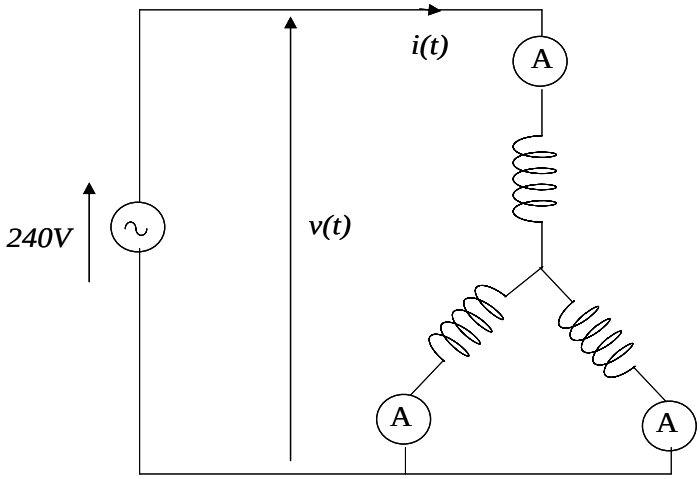

Figure 2-7 Experimental set-up for inductance measurements in *d*- and *q*-axes.

Figure 2-8 shows the typical inductance saturation curves for an interior PM machine. The *q*-axis inductance is high for small values of the *q*-axis current, while the *d*-axis inductance is small and nearly constant for all values of *d*-axis current.

The experimental method used for measuring the inductance saturation curves is based on the instantaneous flux-linkage. This involves uses a CRO to record the instantaneous current $i(t)$ and voltage $v(t)$ waveforms for several periods of the waveform at the rated value of stator current. The current measurements are obtained by using a Hall-effect current probe, while voltage measurements are obtained by using a 1:100 differential voltage probe (to prevent damage of the CRO caused by the high value of the measured voltage).

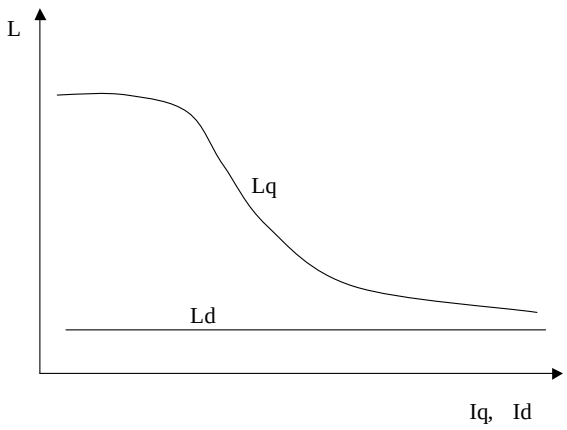

Figure 2-8 Typical inductance saturation curves $L_d=f(I_d)$ *and* $L_q=f(I_q)$.

Figure 2-9 presents the method used to obtain the flux linkage $\lambda(t)$ from the measured voltage $v(t)$ and current $i(t)$ assuming that the resistance R of the phase winding is known and constant.

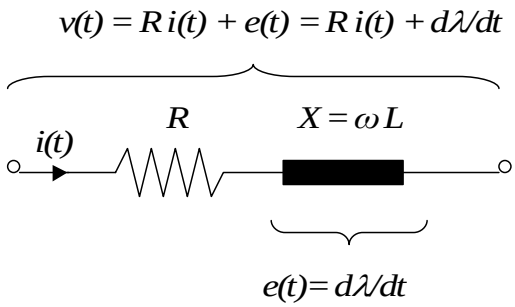

Figure 2-9 Method of obtaining flux linkage $\lambda(t)$ from the measured voltage and current waveforms.

The flux-linkage in each point of the measurement is calculated as an integral of the induced EMF across the inductance of the stator winding:

$$\lambda(t) = \int (v(t) - R\, i(t))\, dt \qquad (2\text{-}10)$$

As the flux linkage $\lambda(t)$ is proportional to the flux density $B(t)$ and the current is proportional to magnetic field $H(t)$, thus the shape of the $\lambda(t)$ versus $i(t)$ curve is equivalent to the shape of the B-H curve of the iron laminations used in the machine design. Their relationship is shown in Figure 2-10.

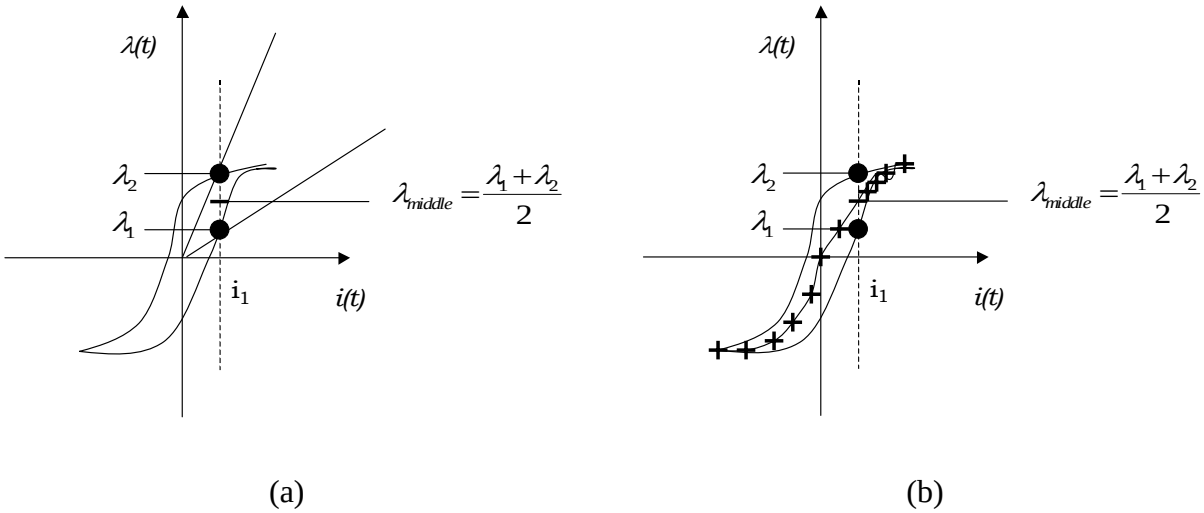

(a) (b)

Figure 2-10 a) Flux linkage versus current characteristic and b) a method of calculating the average value of the flux linkage for a non-linear B-H characteristic with iron loss.

The flux linkage versus current characteristics shows (see Figure 2-10a) that for the same value of current $i_1(t)$ there are two different values of flux linkage. The midpoint method is used

to calculate the average value of the flux linkage for the current i_1 – curve is presented in Figure 2-10b.

The inductance curve is obtained as the ratio of the instantaneous flux-linkage and the stator current. This inductance is the secant or large-signal inductance. As the inductance versus current characteristics shows in Figure 2-11, for the same value of current $i_1(t)$ there are two different values of inductance. Once again the midpoint method is used to calculate the average value of the inductance for the current i_1. To obtain more accurate values of the inductance for low values of stator current, a second flux-linkage test were performed using a current of about 25% of rated current.

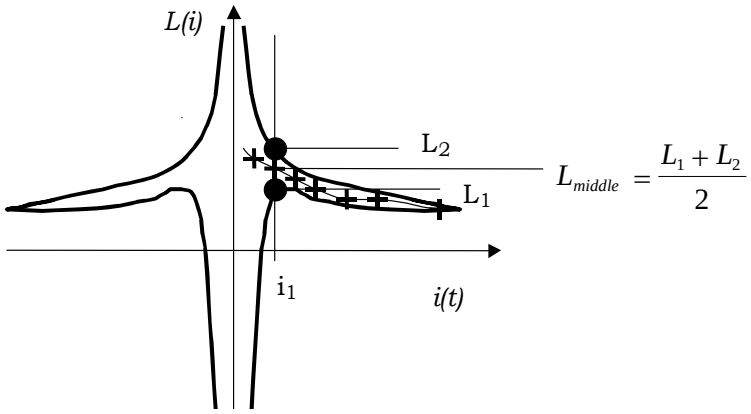

Figure 2-11 Inductances versus current characteristic of a machine for non-linear B-H characteristics with iron loss and the midpoint method of calculating the average inductance.

2.3.2 Output Power and Efficiency Testing Procedures

The open-circuit iron losses (and friction and windage losses) P_{Fe} are equal to the input mechanical power (P_{Mech}) when driving the machine under open-circuit conditions. Figure 2-12a graphically presents this condition.

The short-circuit iron loss measurement presented in Figure 2-12b is obtained by subtracting the copper losses (calculated from the measured stator current) from the input mechanical power required when driving the machine with the stator terminals short-circuited. In the literature this is sometimes referred to a forced-running short-circuit test. Under these conditions, the rotor magnets induce currents in the short-circuited stator winding which produces a flux opposing the rotor magnet flux. At high speeds ideally the stator and rotor flux should cancel one another, resulting in a nearly zero air gap flux and low iron loss. In practice this is not always the case as will be shown in the next section.

Under the resistive load operation presented in Figure 2-12c, the iron losses are obtained by subtracting the copper losses and the electrical output power from the input mechanical power required when driving the machine with the stator terminals connected to the resistive load bank. The efficiency is simply obtained as the ratio of the output and input power.

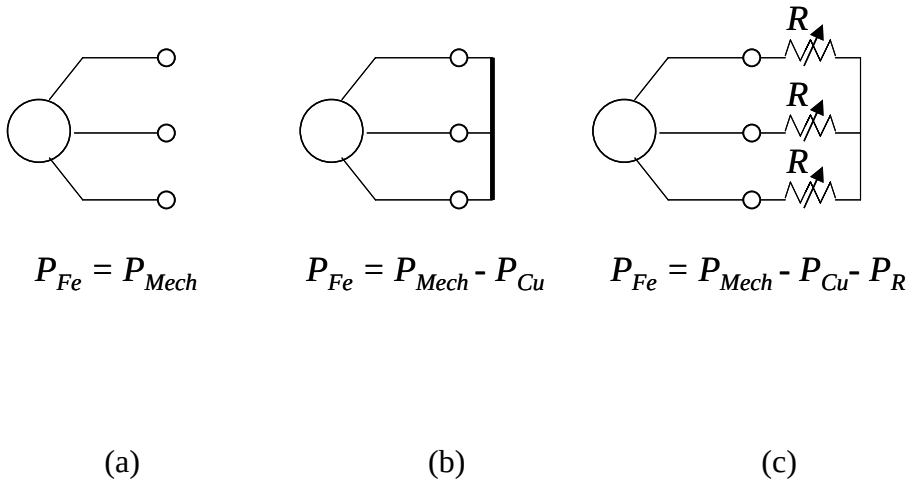

Figure 2-12 Methodology for the iron loss measurments under a) open-circuit (no load), b) short-circuit (field-weakening) and c) resistive-load operation.

2.4 Prior Machine Measurements

A proposed specification for this high-power belt-driven automotive alternator is a linearly increasing output power from 4 kW to 6 kW as the alternator's speed increases from idle (1.8 krpm) to maximum operating speed (18 krpm), assuming a 3:1 belt ratio [43]. Figure 2-13 shows a comparison of the calculated and measured output power versus speed characteristics of the interior PM alternator. The calculated output power versus speed curve was obtained using the analysis method described in Section 2.1. The measured output power shows a good correspondence with the calculated results and meets the high power alternator requirement apart from near the idle speed.

NOTE:
This figure is included on page 22 of the print copy of the thesis held in the University of Adelaide Library.

Figure 2-13 Output power of the interior PM alternator. Measured results (triangles) and calculated performance based on the measured equivalent circuit parameters (solid line) at rated voltage. The high-power alternator specification is also shown [43].

The machine is known to be highly saturated and this was expected to be one of the reasons for the reduced low-speed output power. The maximum speed of the measured results were limited by the 6 krpm dynamometer speed limitation, however the calculated failure speed of the rotor was also only about 12 to 15 krpm. This failure speed was roughly estimated based on an analytical calculation of the speed at which the stress in the rotor bridges would be equal to the yield stress value of the lamination material.

Experimental loss measurements were taken on the machine to examine the variation of iron losses with speed and operating conditions. Figure 2-14 shows the measured iron losses for the interior PM machine with a three-phase resistive load at rated voltage and one-third of rated voltage. Under these conditions, the machine acts like a constant-current source so the output voltage can be controlled by changing the load resistance. It is clear from the graph that the iron loss is not significantly affected by the output voltage and hence by the magnitude of the fundamental component of the flux. As will be shown later in this thesis, this is because the iron losses shown are largely due to harmonic air gap flux components. Note that the iron loss and the mechanical loss components are not separated. Given that the value of loss is far larger than would be expected from mechanical loss sources such as bearings and windage, it was assumed that the high loss was due to iron loss.

NOTE:
This figure is included on page 23 of the print copy of the thesis held in the University of Adelaide Library.

Figure 2-14 Measured losses for the interior PM machine. The total losses are shown at rated voltage. The iron and mechanical losses are shown at both rated and one-third rated voltage [43].

Figure 2-15 shows the measured iron and mechanical losses of the concept demonstrator machine as a function of speed under open-circuit, short-circuit and rated output voltage conditions.

NOTE:
This figure is included on page 23 of the print copy of the thesis held in the University of Adelaide Library.

Figure 2-15 Measured iron and mechanical losses as a function of speed under open-circuit, short-circuit and rated output conditions [43].

Figure 2-15 also shows that the iron losses under short-circuit conditions are roughly twice that under open-circuit conditions. This machine has a high inductance resulting in a short-circuit current which is equal to the rated current, which gives it a wide field-weakening range [19]. Particularly at higher speeds, the back-EMF is much greater than the output voltage and hence rated operation is close to the short-circuit condition. Thus the iron losses under rated conditions are close to the iron losses in short-circuit operation. This is opposite to conventional PM machines where the rated current is usually much smaller than the short-circuit current and hence where rated operation (and iron losses) are close to the open-circuit condition.

At 6 krpm, the iron loss and mechanical loss is about 800 W. As the outer surface of the rotor is smooth, it is assumed that the majority of this loss is iron loss, more specifically likely eddy-current loss due to the high fundamental frequency (200 Hz) at this speed. Assuming that this loss increases with square of frequency, this results in an extremely large estimated iron loss of about 7.2 kW at the maximum alternator operating speed of 18 krpm.

Figure 2-16 shows the machine's measured efficiency at rated output corresponding to the output power curve shown in Fig. 2-14. Below 2.5 krpm, the copper losses dominate and they are relatively constant, and thus as the output power increases with speed so does the efficiency. Above 2.5 krpm, the output power and copper loss are relatively constant and the drop in efficiency is due to the increasing iron losses.

NOTE:
This figure is included on page 24 of the print copy of the thesis held in the University of Adelaide Library.

Figure 2-16 Measured efficiency at rated output of the interior PM machine [43].

2.5. Conclusions

The preliminary study showed the following:

- The machine does not meet the idle-speed power requirement. This is likely due to a high degree of saturation and cross-saturation.

- A high iron loss during field-weakening operation was measured. The iron losses were comparable between the short-circuit and rated output voltage conditions and were approximately double the open-circuit losses. This is consistent with the literature review findings presented in Chapter 1 showing that the field-weakening iron losses are associated with the air gap flux density harmonics. This is because under the field-weakening operation the *d*-axis current is large.

No finite-element analysis has been performed previously for this machine design. In this thesis, finite-element analysis will be used to investigate the reasons for both the low idle-speed power and the high iron loss.

Chapter 3 Back EMF, Inductance and Idle Power of Interior PM Prototype Machine

The previous chapter covered the general machine theory that will be applied to the concept demonstrator (interior PM prototype) machine in this chapter. As finite-element analysis has not been performed on this machine before, in this chapter it will be used for the parameter prediction. The experimental findings presented in Chapter 2 revealed that the interior PM concept demonstrator machine did not meet the output power requirement at idle speed. This chapter will describe the finite-element modelling of the machine and examine the comparisons between the calculated and measured values of: back EMF, inductances in the *d*- and *q*-axes and the idle power of the interior PM prototype machine. The torque in this machine depends on the difference between the *q*- and *d*-axis inductances, the values of stator current and flux-linkage due to magnets. As the idle power is directly proportional to the torque, these parameters will be used for the idle power calculation.

3.1 Finite Element Modelling

Finite-element (FE) modelling is used to examine the flux distribution of the concept demonstrator machine. Due to symmetry reasons, only a quarter of the machine has been analysed. The Magsoft Flux2D package was used in the analysis [47] and the model presented by Figure 3-1 uses around 23,000 elements.

Figure 3-1 shows the FE analysis mesh - part of the air gap region of the concept demonstrator machine. The finest mesh elements are defined in the air gap itself. An uniform mesh spacing along the circumference allows rotation of the model using the sliding surface formed between the two layers of the mesh in the middle of the air gap. The average execution time varies between 30 minutes up to one and a half hours depending on the performed calculation type.

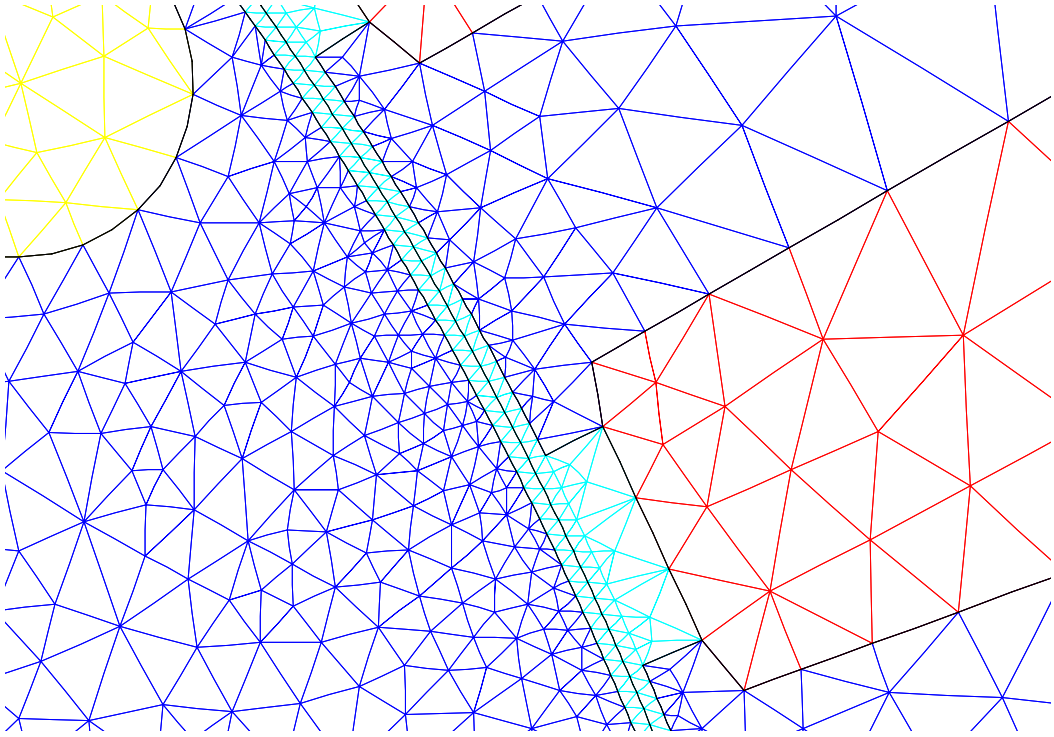

Figure 3-1 FE analysis mesh - part of the air gap region of the concept demonstrator machine.

The rare-earth magnets do not take up the entire area of the rotor slots (flux barriers) as shown in Figure 3-2 *Left*.

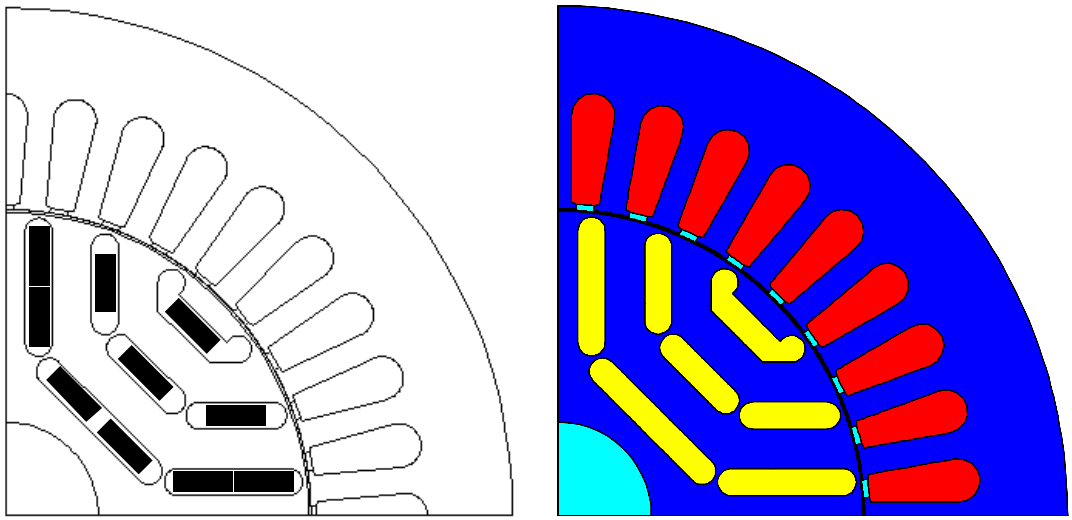

Figure 3-2 *Left:* quarter cross section area of the concept demonstrator machine with the real NdFeB magnets. *Right:* FE analysis quarter model of the concept demonstrator machine showing the assumption that the magnets occupied the whole rotor slot areas.

The magnets were modelled by reducing the magnet remanent flux density by the ratio of the magnet area to the slot area as it has been presented by Figure 3-2 *Right.* The magnet properties are as follows: sintered NdFeB blocks, remanent flux density 1.1 T and relative recoil

permeability μ_r = 1.05. A linear second quadrant de-magnetization characteristic was assumed. Table 3-1 provides detailed calculation of the equivalent magnet remanence for each rotor barrier.

Table 3-1 Calculated equivalent magnet remanence for each rotor barrier.

Magnet Location:	**Magnet Area A_m [mm^2]:**	**Slot Area A_{slot} [mm^2]:**	**Equivalent Remanence B_r[T]:**
Barrier 1	27	76.7	0.369
Barrier 2, Centre	27	58.0	0.487
Barrier 2, Outer	27	57.9	0.489
Barrier 3, Centre	54	98.5	0.574
Barrier 3, Outer	54	80.8	0.701

3.2 Back EMF

3.2.1 Finite Element Prediction

Calculation of the back EMF using the FE program package is performed in 360 steps by one-degree rotation (equivalent of one full electrical cycle) to obtain the back EMF waveform. Figure 3-3 presents flux plots of the concept demonstrator machine for three different rotor positions under the open-circuit condition. The flux in the machine is caused by the rotor magnets only.

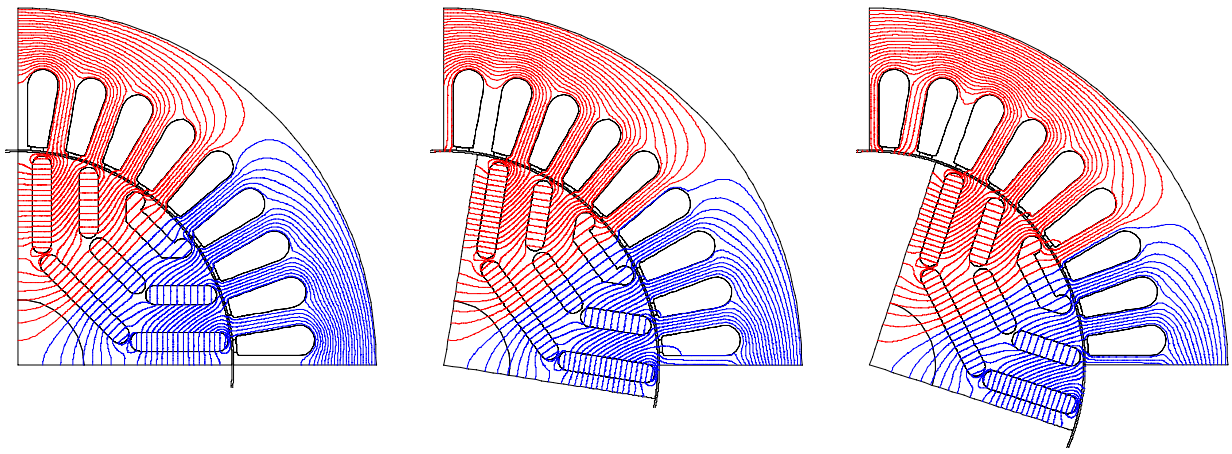

(a) (b) (c)

Figure 3-3 Flux plots of the concept demonstrator machine for three different rotor positions under open-circuit conditions: a) 0 degree, b) 10 degrees and c) 20 degrees.

Figure 3-4 presents the winding diagram for the concept demonstrator machine. Points 1 to 36 show the middle points of the stator slot-openings. Finite element analysis calculates the value of the vector potential at the middle points of the stator slot-opening for each time step (or for the specific rotor position described by the rotor angle). Each of the stator phase windings consists of six coils in series, forming four coil bands of three coils per band.

The flux-linkage of each coil, at each point in time, is calculated as the vector potential difference between the starting and the ending slots multiplied by the number of turns per coil (47 in this case). The total flux-linkage per phase is calculated as an algebraic sum of all six individual coil flux-linkages. According to Faraday's law the back EMF per phase is calculated as the rate of change of the total flux linkage per phase with time.

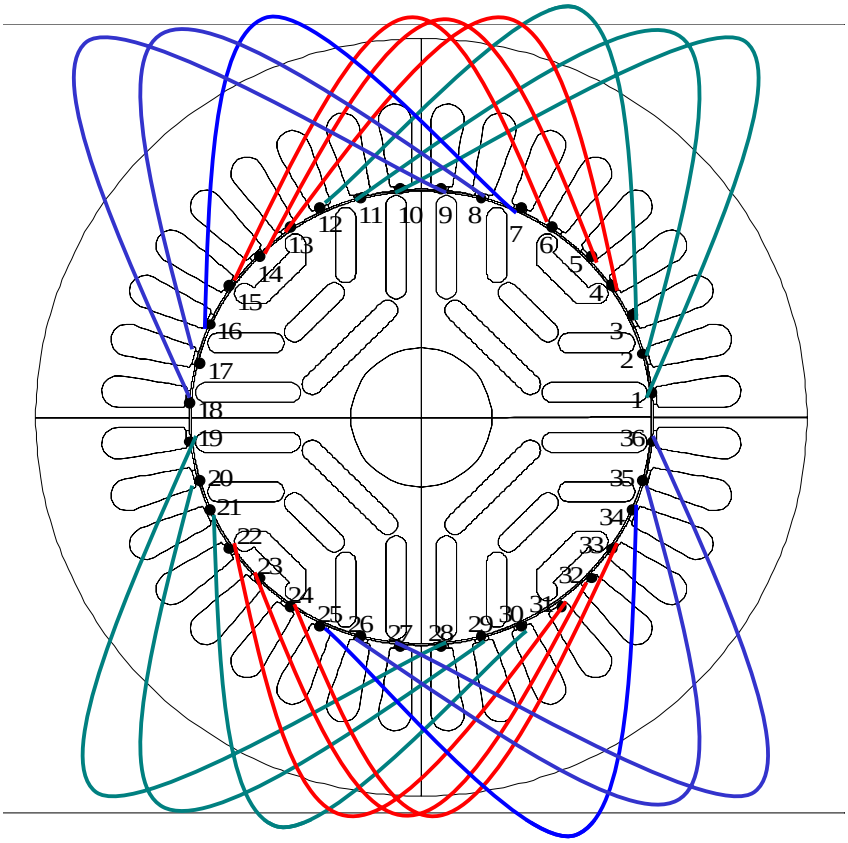

Figure 3-4 Winding diagram for the concept demonstrator machine. Points 1 to 36 show the mid-stator slot openings.

Under the open-circuit condition the stator current is zero. According to expression (2-2) the obtained EMF is equal to the q-axis voltage assuming R_a negligible. Dividing the value of the q-axis voltage by ω will give the flux-linkage due to the magnets Ψ_m, which is then used for the calculation of machine torque.

The finite-element radial air gap flux density of the concept demonstrator machine under the open-circuit condition at a certain rotor position is given in Figure 3-5. This shows a roughly trapezoidal distribution which is modulated by the stator slot openings.

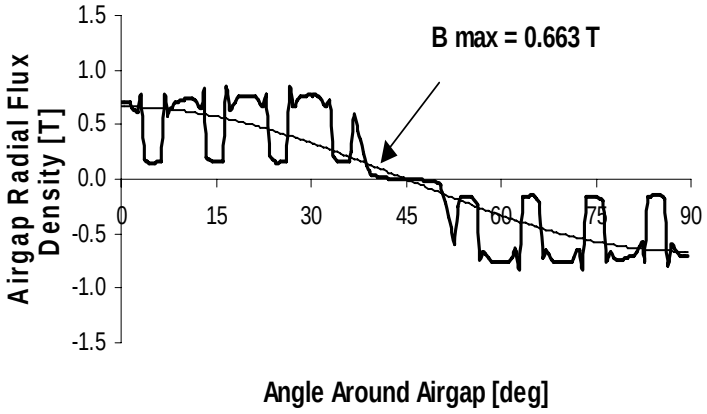

Figure 3-5 Finite-element air gap radial flux density of the concept demonstrator machine under the open-circuit condition.

The calculated waveforms of all three phase back EMFs for the concept demonstrator machine at 1500 rpm have been presented in Figure 3-6a. The line-to-line back EMF is calculated as a difference between two calculated phase back EMFs, see Figure 3-6b. The phase back EMF-s is mostly rectangular shaped, while the line-to-line EMF-s are more sinusoidal.

The frequency spectra comparison presented in Figure 3-6c shows that both waveforms have a dominant 1^{st} harmonic, where the ratio between the phase and line values is $\sqrt{3}$ as expected. For the phase back EMF the second largest harmonic is the 3^{rd}, followed by the 19^{th}, 15^{th}, 9^{th} and 11^{th}. The line back EMF waveform has no 3^{rd}, 9^{th} or 15^{th} harmonics as these are zero sequence components (triplens), while the second dominant harmonic is 19^{th} followed by 13^{th} and 11^{th}.

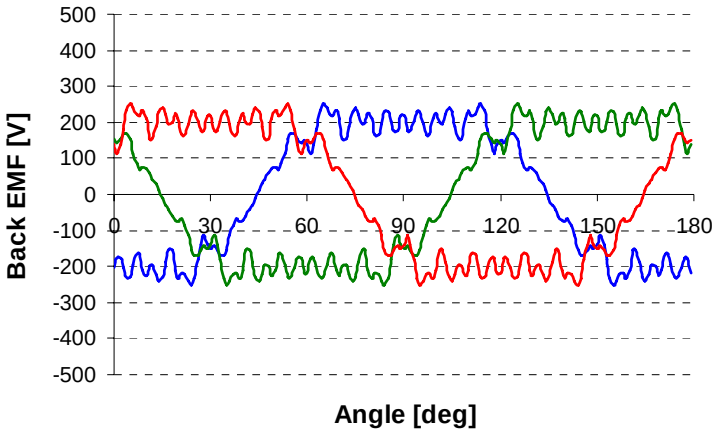

(a)

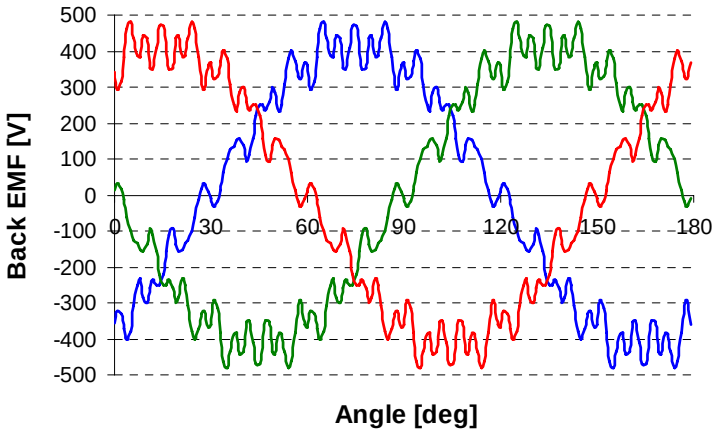

(b)

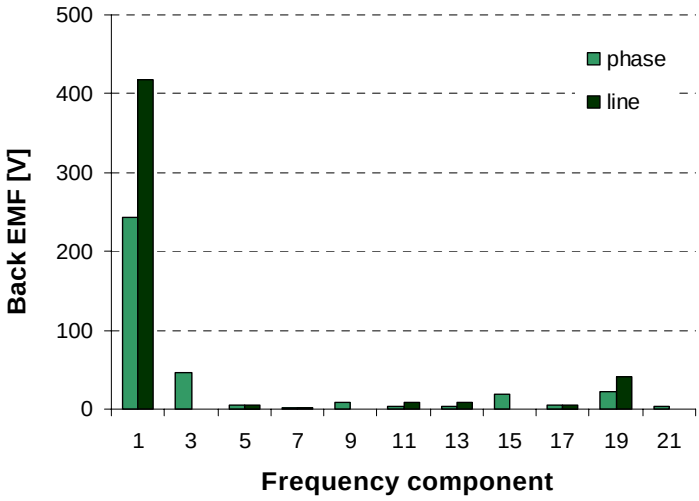

(c)

Figure 3-6 Calculated FEA back EMF-s for concept demonstrator machine at 1500 rpm: a) per phase, b) line to line and c) frequency spectra comparison per phase and line-to-line.

3.2.2 Comparison with Measurements

The concept demonstrator machine is run as an alternator at 1500 rpm under the open-circuit condition. A measured line-to-line back EMF waveform is obtained by use of 1:100 voltage probe connected across two stator phases allowing the CRO to record the waveform presented in Figure 3-7a. The previously calculated FEA prediction of the line back EMF waveform is compared to the measured one.

According to Figure 3-7a the presence of higher frequency harmonics is clear for both waveforms. The measured and calculated RMS results in Figure 3-7b show that the calculated value is around 10% higher compared to the measured one.

Figure 3-7c provides the frequency spectra comparison between the measured and calculated line waveforms with the highest peak of the 1^{st} harmonic followed by the 19^{th}. Note that the measured fundamental component is lower than the calculated one. The reasons for that could be: the actual air gap of the measured machine is slightly larger than assumed and/or that the remanent magnetism of the rotor magnets is lower than it has been assumed. The harmonic content of the measured back-EMF waveform is higher than calculated. This could be due to a non uniform air gap of the real machine or that the stator tooth are not perfectly uniformly spaced.

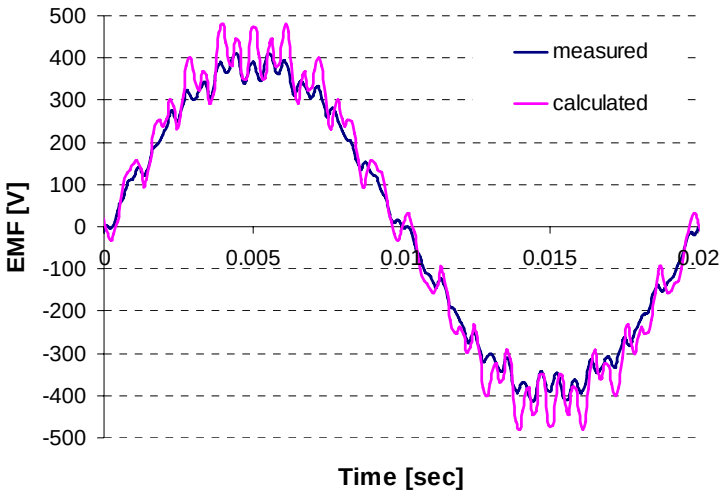

(a)

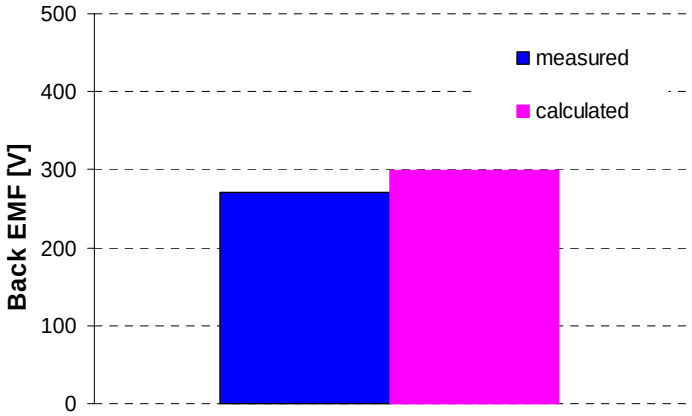

(b)

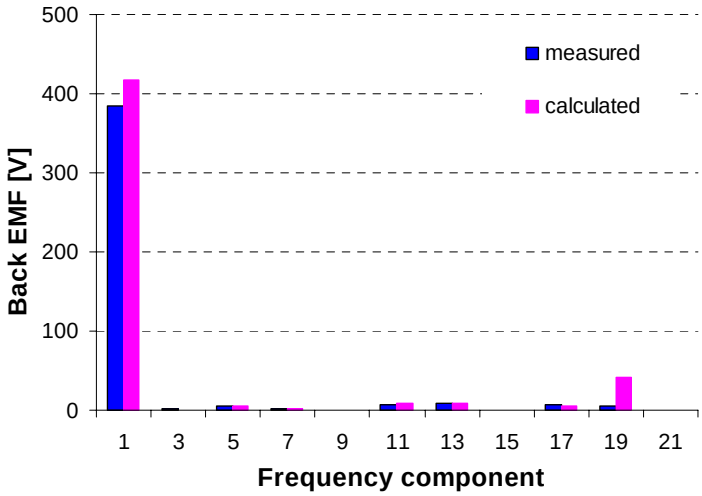

(c)

Figure 3-7 Measured and calculated (FEA) back EMFs for concept demonstrator at 1500 rpm. a) line-to-line, b) compared RMS values and c) frequency spectra comparison between measured and calculated line waveforms.

3.3 D- and Q-axis Inductances

In this section finite-element predictions of the *d*- and *q*-axis inductance curves are compared with the experimental measurements. Effects of saturation and cross-saturation on the reluctance and rare-earth rotor constructions have been examined.

Saturation is the phenomenon where current or flux in an axis reduces the inductance in the same axis, while cross-saturation is the phenomenon where flux in one axis produces a drop of the inductance in the other axis.

3.3.1 Finite-Element Predictions of the Inductance Curves

The calculated values of the *d*- and *q*-axis inductances (the secant or large-signal inductances) are both determined from the total flux linkage per phase for each case individually. The explanation of obtaining the total flux linkage per phase has already been presented in Section 3.2 as part of the back EMF calculation procedure. Figure 3-8 presents the finite element method used to determine the *d*- or *q*- axis inductance, by determining the stator flux linkages. Note phase *a* is connected in series with phases *b* and *c* in parallel. Note that the model uses a DC current source.

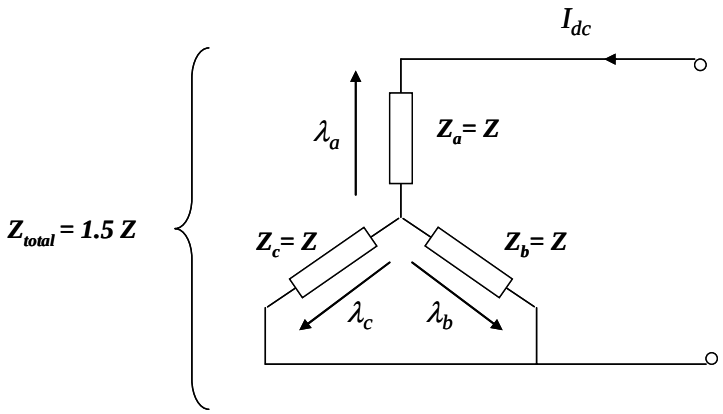

Figure 3-8 Calculated (FEA) method for obtaining the *d*- or *q*- axis inductances.

The total flux-linkage per phase is calculated by the following equation:

$$\lambda_{ph} = 1.5\left[\lambda_a - 0.5\left(\lambda_b + \lambda_c\right)\right] \tag{3-1}$$

Finally the *d*- or *q*-axis inductance is calculated as a ratio of the flux-linkage per phase and the DC stator current:

$$L = \lambda_{ph} / I_{dc} \tag{3-2}$$

3.3.2 Saturation Effects with Reluctance Rotor

The FEA flux plots and *d*- and *q*-axis inductance curves are obtained for four cases: no rotor, the solid rotor, the reluctance rotor in the *q*-axis and the reluctance rotor in the *d*-axis. Figure 3-9 presents the finite-element magnetic flux distribution for all four cases. For all cases presented the applied current to the stator winding was equal to the rated current (9.4 Arms).

The FEA flux plot for no rotor in Figure 3-9a shows the ideal flux distribution in the interior of the stator and shows the phenomena of stator slot leakage. The solid rotor flux plot in Figure 3-9b shows a similar flux distribution in the interior of the stator to the no rotor case. The level of stator slot leakage would be comparable to the no rotor case, however as the main flux is much larger in this case, the slot leakage becomes relatively smaller. Figure 3-9c and 3-9d show the flux plots for the reluctance rotor. The *q*-axis case shows a similar flux distribution to the solid rotor, except the rotor has approximately twice the flux density. The *d*-axis case shows that flux leakage through the rotor bridges contributes significantly to the *d*-axis flux linkage and hence *d*-axis inductance of the machine. The amount of rotor bridge leakage can be estimated from the flux plot. This has 25 flux lines and only roughly half of these pass through the rotor flux-barriers with most of the remainder passing through the rotor bridges. Thus the leakage flux is approximately equal to the magnetising flux under this condition.

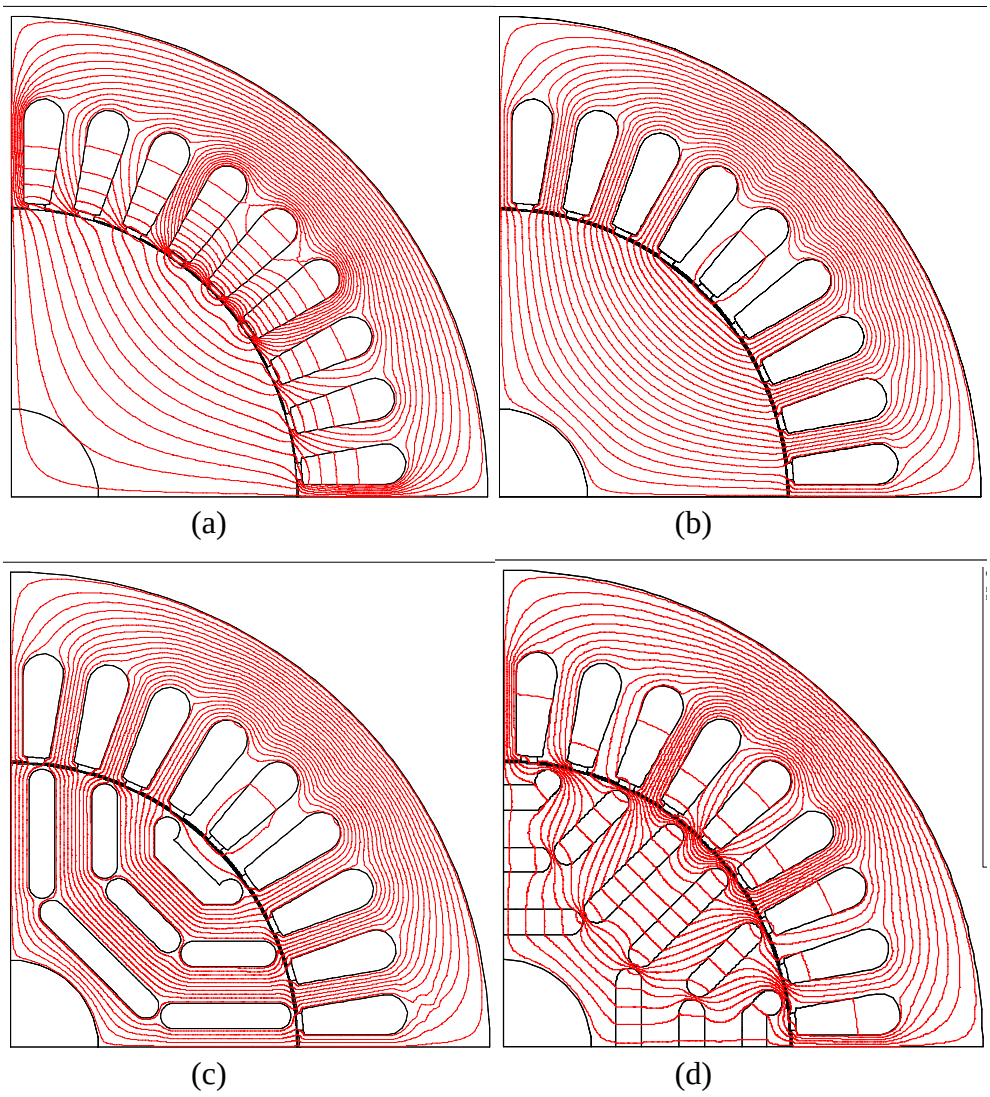

Figure 3-9 Finite-element magnetic flux distribution: a) no rotor, b) solid rotor, c) with reluctance rotor (no magnets) in *q*-axis and d) with reluctance rotor (no magnets) in *d*-axis.

Figure 3-10 *(upper)* presents the calculated flux linkage versus stator current characteristic for the reluctance rotor machine. The flux linkages per each phase (λ_a, λ_b and λ_c) are determined as a function of the stator current using the FEA results (vector potentials). As the stator current is the only cause of the magnetic field in the reluctance machine it is expected that the λ_b and λ_c will be identical due to the parallel connection between these two phases and their symmetry. From the λ_a, λ_b and λ_c curves the total flux linkage $\lambda_a - ½ (\lambda_b + \lambda_c)$ curve is obtained and as it has been described in Section 3.3.1 the *q*-axis inductance characteristic is produced and is presented in Figure 3-10 *(lower)*.

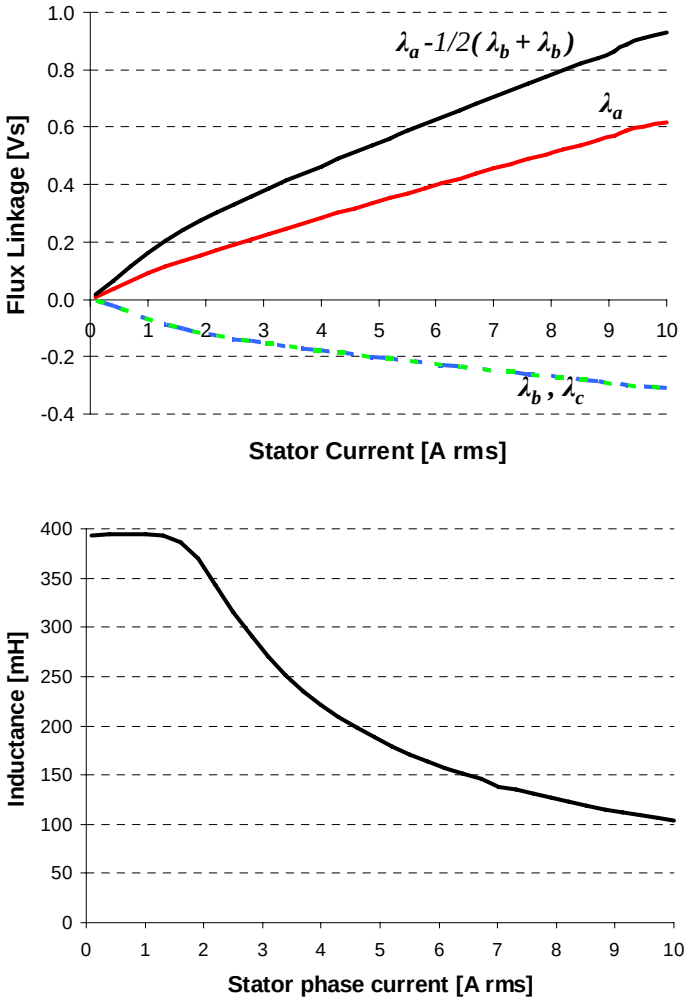

Figure 3-10 Reluctance rotor. *Q*-axis flux linkages *(upper)* and inductance *(lower)* versus stator current characteristic.

Figure 3-11 and Table 3-2 present a comparison of the inductances from analytical, finite-element analysis and experimental tests. The analytical values were obtained using the standard analytical machine inductance equations given in [46].

Figure 3-11 shows the finite-element calculated saturation curves for each of the four simulated cases. The curves for the solid rotor and the *q*-axis of the reluctance rotor are very close despite the higher rotor flux density in the reluctance rotor case. This implies that most of the saturation in this machine occurs in the stator. The *d*-axis inductance curve starts off at a high value due to the rotor slot bridges, but these rapidly saturate as the current increases. The inductance with no rotor is much smaller than the saturated *d*-axis inductance case due to the rotor bridge leakage described previously. The FEA results show a good match with the experimentally obtained measurements.

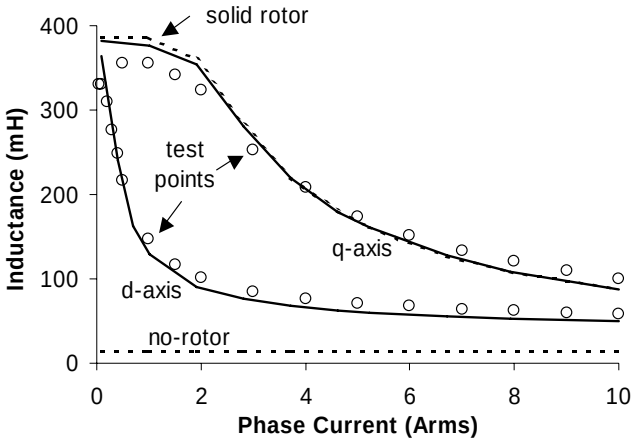

Figure 3-11 Calculated (FE) values of *d*-axis and *q*-axis inductance saturation curves for the concept demonstrator machine with no rotor, with solid rotor and for the *d*- and *q*-axes of the reluctance rotor. The measured data for the reluctance rotor are also shown (circles).

Table 3-2 Comparison of inductances from analytical, finite-element analysis and experimental tests. The analytical and FEA results do not include the end-winding inductance.

Case:	**Analytical**	**Finite Element**	**Experimental**
no rotor	14.5mH	14.2mH	19.8mH
end-winding			5mH
D-axis : 9.4A (reluctance)	27mH	51mH	59mH
D-axis : 9.4A (rare-earth)		48mH	54mH
Q-axis unsat (reluctance)	379mH	383mH	355mH
Q-axis unsat (rare-earth) cross-saturation		354mH	312mH
solid rotor	379mH	386mH	

Table 3-2 shows that the analytical value for the inductance with no rotor and no end-windings is 14.5mH. This is very similar to the FEA value of 14.2mH corresponding to the flux plot in Figure 3-9a). The inductance of the stator without a rotor was measured as 19.8mH. The difference between the measured inductance without the rotor and the analytically/FEA calculated inductance with no rotor and no end-windings is due to the end-winding leakage inductance. From this, the end-winding inductance was estimated to be about 5mH.

The iron in the reluctance rotor reduces the reluctance of the rotor *d*-axis flux path and hence the analytical *d*-axis inductance (27mH) is about twice the value with no rotor. The analytical *d*-

axis inductance does not include the effects of the rotor slot bridge leakage. From Figure 3-9d) this was shown to be comparable to the *d*-axis magnetising inductance and so it was not surprising that the finite-element *d*-axis inductance (59mH) is approximately double the analytical value. The finite-element value is about 8mH lower than the measured value but part of this difference is due to the estimated 5mH of end-winding leakage inductance.

The solid rotor predictions for the analytical (379mH) and the finite-element case (386mH) match well. For the *q*-axis case with the reluctance rotor, the measured unsaturated inductance (355mH) is about 8% lower than the FEA and analytical predictions. This is probably caused by slight errors in the air gap length.

To observe the impact of saturation on the stator and rotor, FEA was used to analyse the following four cases:

- no rotor or stator saturation,
- rotor saturation but no stator saturation,
- stator saturation but no rotor saturation, and
- both stator and rotor saturation.

In the four cases above, the non-saturating parts of machine were modelled by a magnetic material with a constant permeability equal to the maximum permeability of Polycor, while the full BH characteristic for the Polycor was used to model the saturating parts of the machine.

The results are shown in Figure 3-12. The curves for stator saturation only, and for both stator and rotor saturation are very similar. This confirms that most of the saturation takes place in the stator. The measured points show a reasonable correspondence with the calculated curve.

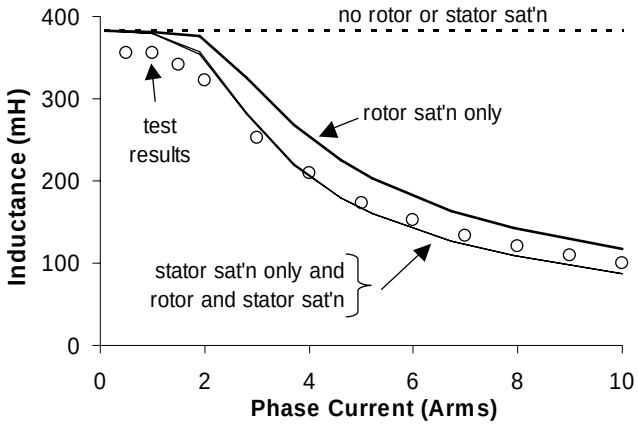

Figure 3-12 Effect of saturation of the rotor and stator on the *q*-axis inductance saturation curve of the reluctance machine.

3.3.3 Saturation and Cross-Saturation with Rare-Earth Magnet Rotor

The previous FEA analysis was done without rotor magnets for the reluctance rotor. Simulations were also performed to investigate the effect of the rare-earth magnets in the interior PM rotor on the *q*- and *d*-axis saturation curves. Figure 3-13 shows flux plots for the rare-earth PM rotor and the corresponding air gap radial flux density plots (only for cases a and b), for a) with no stator currents, b) with rated stator current in the d-axis and c) with rated stator current in the *q*-axis. Figure 3-13a corresponds to the open-circuit condition, while Figure 3-13b to the field-weakening operation. The *d*-axis flux plot in Figure 3-13b shows significant leakage flux in the vicinity of the air gap. This results in the presence of high frequency air gap flux density harmonics, which are evident in the air gap radial flux density plot in Figure 3-13b. The presence of such harmonics is the possible cause of the high iron losses measured under the field-weakening conditions. In Figure 3-13c the flux distribution is the combination of the *d*-axis magnet flux and *q*-axis stator flux.

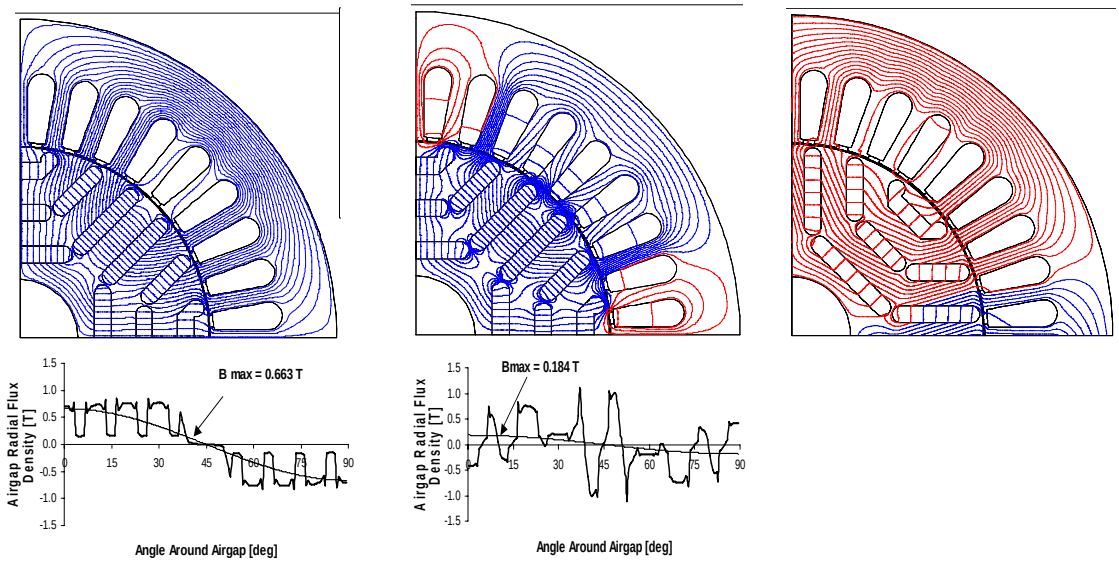

a) b) c)

Figure 3-13 Finite-element flux distribution of the rare-earth rotor and air gap radial flux density flux plots (only cases a and b) for a) with no stator current, b) with rated stator current in the d-axis (de-magnetizing case) and c) with rated stator current in the q-axis as used to model cross-saturation in the machine

Figure 3-14 presents the three phase flux linkage versus *d*-axis stator current characteristics for the rare-earth rotor machine. The phase flux linkages show an offset (stator current equal zero) due to the *d*-axis magnet flux – Figure 3-14 *(upper)*. The offset was removed and the result shown in Figure 3-14 *(lower)*. The total flux linkage is then calculated using λ_a-½(λ_b+λ_c).

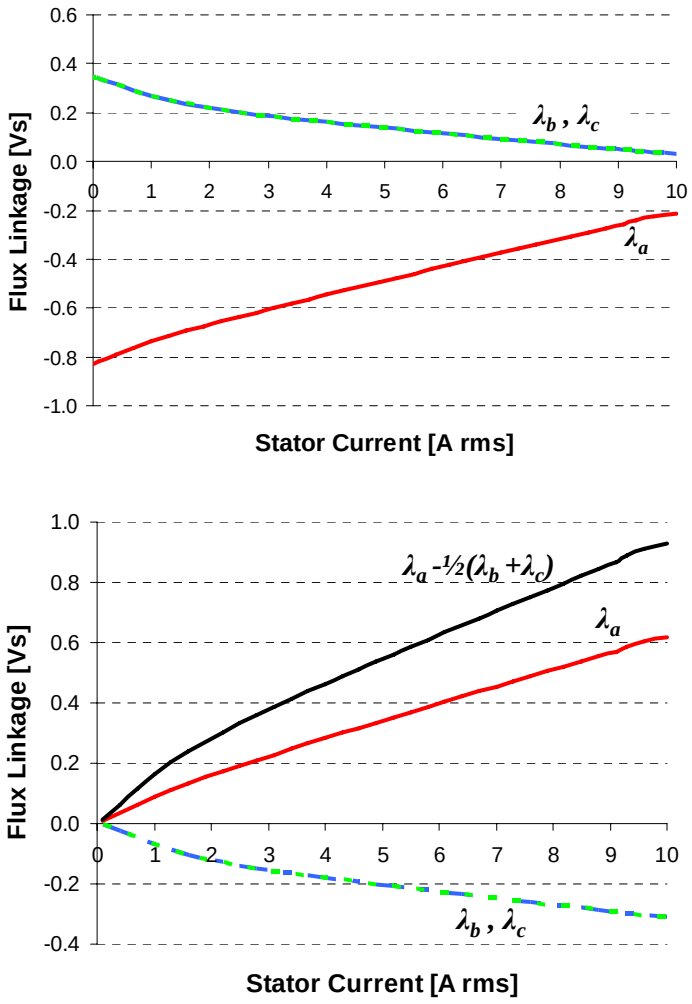

Figure 3-14 Phase flux linkages versus *d*-axis stator current characteristic for the rare-earth rotor machine with *(upper)* original curves *(lower)* with offset removed and *d*-axis flux linkage calculated.

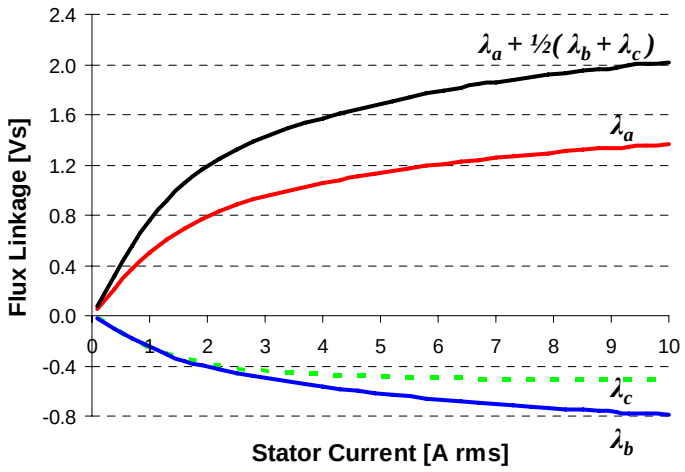

Figure 3-15 Phase flux linkages versus *q*-axis stator current characteristic for the rare-earth rotor machine.

Figure 3-15 shows the *q*-axis phase flux-linkages versus *q*-axis current in the presence of the *d*-axis magnet flux. It is noticeable that the flux linkages in the *b* and *c* phases are nearly the same for the stator currents up to 1.8 A. Above 1.8A the flux linkage in phase *c* becomes different in value than the phase *b* and at rated current this difference reaches approximately 0.3 Vs. This can be explained by cross-saturation caused by the interaction of two magnetic fields: the *d*-axis rotor magnets field and the *q*-axis stator current electromagnetic field. The presence of the permanent magnet field causes the flux linkage in phase *c* to saturate much earlier than phase *b.*

Figure 3-16 shows the calculated interior PM machine *d*- and *q*-axis inductance curves taking into account the rare-earth magnet flux. Comparing these with the calculated reluctance curves, it can be seen that there is significant cross-saturation on the *q*-axis results, especially at low currents. This cross-saturation is likely to be due to saturation in the stator teeth. The *q*-axis experimental results follow the general trend of the calculated curve but have a significantly lower unsaturated inductance and a higher saturated inductance. The *d*-axis results show that the PM flux saturates the rotor bridges and so reduces the *d*-axis inductance substantially at low currents. The *d*-axis experimental results match well with the finite-element predictions.

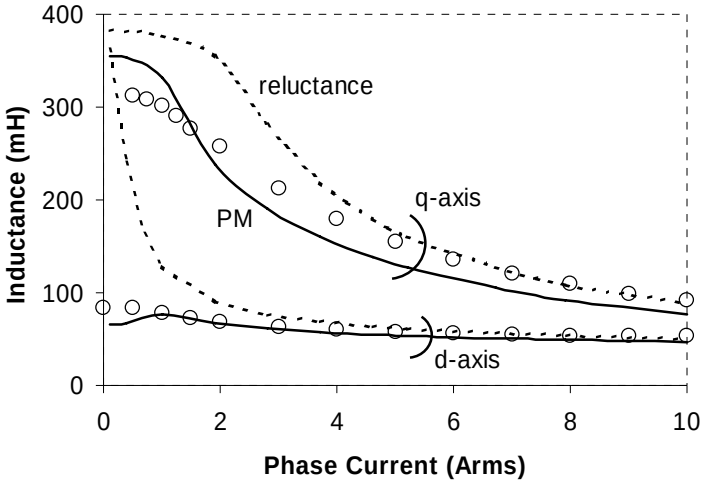

Figure 3-16 Interior PM machine *d*- and *q*-axis inductance measurements (circles) and calculated results for PM rotor including cross-saturation (solid lines) and reluctance rotor (dashed lines).

The above results have shown that the FEA method is a useful mathematical tool for the parameter and performance prediction of this type of machine.

3.4 Idle Power Characteristics

At the idle speed of 1.8 krpm (assuming a 3:1 belt ratio), the interior permanent magnet automotive alternator should be capable of producing 4 kW output power. Unfortunately measurements reveal that the machine felt short by 14.5% to satisfy this requirement. To investigate this issue the *q*- and *d*-axis inductance curves are used to calculate the output power characteristic versus speed to explore the impact of the saturation and cross-saturation on the machine performance.

The calculated output power versus speed characteristics for four *q*-axis saturation cases based on the measured inductance curves shown in Figure 3-17:

- no saturation or cross-saturation (uses a constant value of L_q equal to the reluctance rotor's unsaturated L_q),
- saturation but no cross-saturation (uses reluctance rotor's L_q curve),
- cross-saturation but no saturation (uses a constant value of L_q equal to the rare-earth rotor's unsaturated value of L_q) and
- finally both saturation and cross-saturation (uses rare-earth rotor's L_q curve).

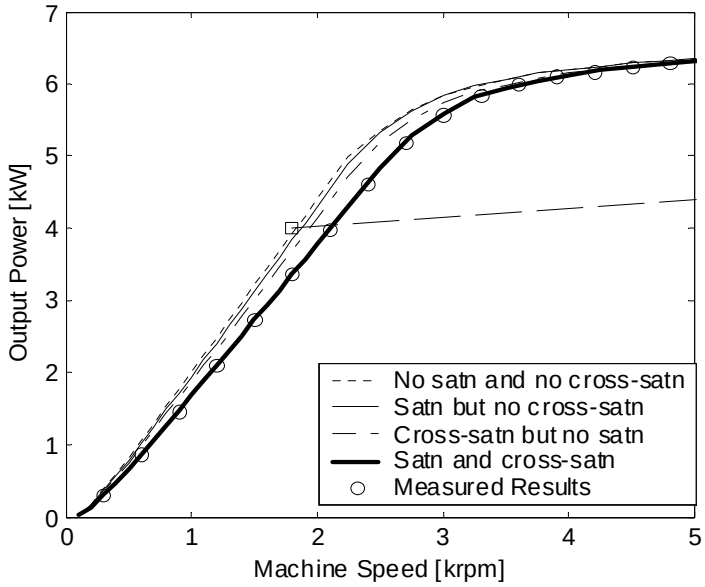

Figure 3-17 Calculated effect of saturation and cross-saturation on the interior PM machine's low-speed (0 to 5krpm) output power characteristics. The measured results (circles) for the machine are also shown. The long dashed line shows the alternator requirement.

The measured saturating *d*-axis curve for the rare-earth rotor was used for all four cases. The calculated output power was obtained from the inductance saturation curves and rare-earth rotor magnet flux using the standard *d*- and *q*-axis interior PM machine equations assuming a limited output voltage and current [43]. The calculated output power at 1,800 rpm for the four cases is shown in Table 3-3.

Table 3-3 Calculated output power at 1,800 rpm for the four cases shown in Figure 3-16, and the reduction in output power compared to the ideal case.

Saturation	**Cross-saturation**	**Calculated Output Power at 1,800 rpm**	**Reduction in Output Power**
no	no	3.93kW	0% (ref)
yes	no	3.83kW	2.5%
no	yes	3.69kW	6.1%
yes	yes	3.36kW	14.5%

Figure 3-16 shows that the measured results (circles) match well with the calculated result (thick solid line). With no saturation and no cross-saturation the alternator output power should be very close (3.93kW) to the requirement. From Table 3-3, cross-saturation has a larger effect

(6.1%) in reducing the low-speed output power than saturation (2.5%), however when both forms of saturation are present, the net reduction in output power (14.5%) is substantially greater than simply the sum of the two effects.

3.5 Conclusions and Findings

In this chapter, finite-element modelling was used as a tool to calculate the line and phase back EMF waveforms and the *d*- and *q*-axis inductance curves of the concept demonstrator machine. To take into account the fact that the magnets do not fill the rotor slots, the magnet remanent flux density was reduced by the ratio of the magnet area to the slot area. The inductance curves were used to provide insight into the saturation and cross-saturation effects and how these affect the idle power of the machine. The calculated results were compared with previously measured machine parameter/performance characteristics and the following conclusions were obtained:

- The measured fundamental back-EMF component is lower (10%) than calculated. This could be due to difference in the machine air gap length and/or to the fact that the remanent magnetism of the rotor magnets is lower than has been assumed.
- The harmonic content of the measured back EMF waveform is higher than calculated. This could be due to non-uniform air gap length of the real machine and/or the fact that the stator teeth are not exactly uniformly spaced.
- As the inductance curves for the solid rotor and the *q*-axis reluctance rotor are very close, most of the saturation in this machine likely occurs in the stator.
- The *d*-axis reluctance rotor inductance curve starts off at a high value due to the non-saturated rotor bridges, and then with increasing stator current rapidly drops due to saturation of the rotor bridges.
- The *q*-axis interior permanent magnet rotor inductance curve shows saturation caused by *q*-axis stator current and cross-saturation caused by *d*-axis rotor magnet flux.
- The *d*-axis interior permanent magnet rotor inductance curve shows saturation of the rotor bridges caused by the rotor magnets.
- With no saturation and no cross-saturation the alternator should be very close (3.93kW) to the idle-speed output power requirement. Although cross-saturation has a larger effect (6.1%) in reducing the low-speed output power than saturation (2.5%),

the overall effect of both forms of saturation resulting in a net output power drop of 14.5%. This is substantially greater than the simple sum of the two effects (8.6%) and is caused by the non-linear nature of the phenomena.

This chapter presented a comparison between the measured and FE calculated parameter/performance characteristics of the concept demonstrator machine and provides understanding of the saturation and cross-saturation effects. The following chapter will cover the iron loss analysis of the interior PM prototype machine.

Chapter 4 Iron Loss Analysis of Interior PM Prototype Machine

The previous chapter covered the comparison between the calculated (FEA) and measured values of back EMF and inductances in the *d*- and *q*-axes and discussed the idle power issues related to low speed operation of the concept demonstrator machine. This chapter examines the iron loss analysis using the finite-element model. It includes:

- background theory of the iron losses,
- comparison of the measured and calculated tooth flux waveforms under open and short-circuit conditions,
- calculation of iron loss in the stator teeth, and
- comparison with measured total losses.

4.1 Machine Losses

There are three major components of power losses in electrical machines: copper loss, iron losses and mechanical losses.

Copper loss is caused by the flow of the stator current through the stator winding resistance. It is related to current and hence torque. The effect of copper loss is reflected in increased temperature of the stator winding.

Iron losses are caused by changing electromagnetic flux in a ferromagnetic material and they are speed (frequency) related. To the first approximation they are not affected by current.

Copper and iron losses are generally the two dominant loss mechanisms. Under rated operating conditions the iron loss is generally approximately equal to the copper loss.

Mechanical losses consist of two components: friction and windage losses. Friction loss is caused by the friction in bearings and rotating seals, while windage loss is the power loss associated with moving air in the machine, particularly due to cooling fans attached to the rotor.

4.1.1 Iron Losses

The theory of electro-mechanical energy conversion [48] describes two different types of iron loss components: hysteresis loss and eddy-current loss. Although the rotational and excess losses are also known as iron losses, they will not be considered in this research.

4.1.1.1 Hysteresis Loss

In 1892, C. P. Steinmetz proposed an empirical formula for the calculation of hysteresis loss [48], which was deduced from a large number of experimental measurements and observations. According to his findings, the hysteresis loss P_h in a magnetic material for a sinusoidal flux density waveform is given by:

$$P_h = C_h f \left(B_{pk}\right)^n \tag{4-1}$$

where:

C_h hysteresis loss coefficient;

B_{pk} peak value of flux density [T];

f frequency [Hz];

n Steinmetz exponent (typically 1.6, but can vary between 1.6 and 2.3);

From equation (4-1) it follows that the hysteresis loss is directly proportional to applied frequency and roughly proportional to the square of the peak value of the machine flux density. Note that the Steinmetz exponent is not a constant. To a first approximation it can be described as a linear function of the peak value of the machine flux density B_{pk} according to [49]:

$$n = a + bB_{pk} \tag{4-2}$$

where:

a, b constants dependent on thickness and type of ferromagnetic material;

So, a new expression for hysteresis loss is:

$$P_h = C_h f \left(B_{pk}\right)^{a+bB_{pk}} \tag{4-3}$$

4.1.1.2 Eddy-current loss

One of the characteristics of ferromagnetic materials is that they generally conduct electricity. If the magnetic flux in a ferromagnetic material is time varying, it will induced a voltage in it. This voltage will cause the flow of eddy currents within the material in such

direction that will produce a flux component that will oppose the change in the applied magnetic flux. As the ferromagnetic material has finite resistance, energy will be dissipated due to ohmic loss. This loss is called eddy-current loss and it can become the major component of total machine losses for high-speed machines. The standard equation for the eddy-current loss P_e caused by a sinusoidal flux density waveform is given by:

$$P_e = C_e f^2 B_{pk}^2 \tag{4-4}$$

where:

C_e eddy-current loss coefficient.

As the flux density waveform in the interior PM alternator is generally non-sinusoidal in nature, the eddy-current loss will be determined by two different methods: The *dB*/*dt* method and the Fourier series analysis method is presented in Figure 4-1.

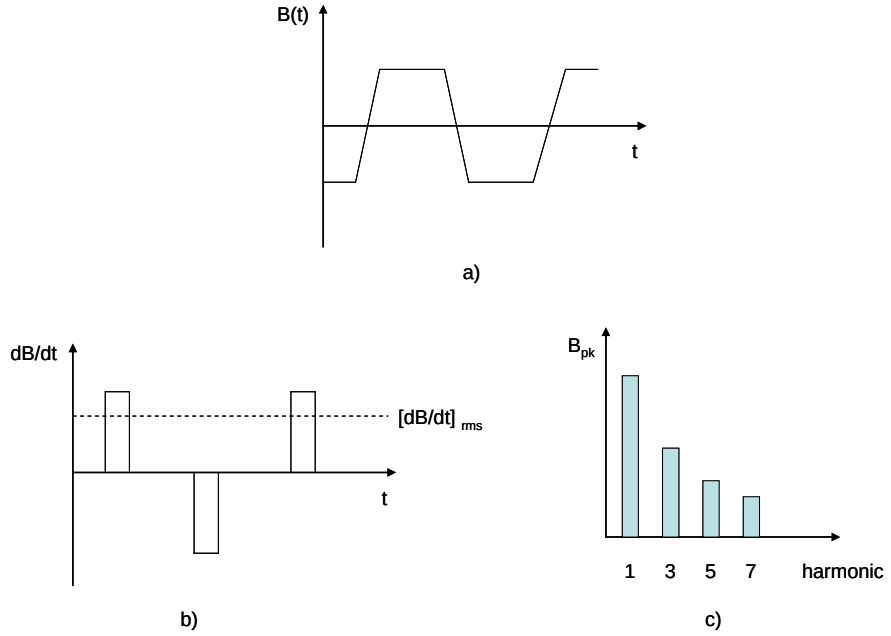

Figure 4-1 a) Example non-sinusoidal flux density waveform and eddy-current loss calculation by: b) *dB*/*dt* method and c) Fourier series analysis method.

dB/dt Method

The eddy-current loss could be briefly described as a resistive loss in conductive ferromagnetic materials due to changing magnetic fields. As the resistive loss is proportional to $e^2(t)$, it is also proportional to $[dB/dt]^2$. Therefore the average power loss is proportional to the square of the RMS value of *dB*/*dt*.

A sinusoidally-varying flux density can be expressed as:

$$B(t) = B_{pk} \sin(2\pi ft) \tag{4-5}$$

The first derivative of $B(t)$ is:

$$dB(t)/dt = 2\pi f B_{pk} \cos(2\pi ft) \tag{4-6}$$

which has an RMS value of:

$$\left[dB(t)/dt\right]_{rms} = 2\pi f/\sqrt{2} \times B_{pk} \tag{4-7}$$

From (4-7) B_{pk}^2 could be expressed as:

$$B_{pk}^2 = \left[dB(t)/dt\right]_{rms}^2 \times \frac{1}{2\pi^2 f^2} \tag{4-8}$$

If the value of B_{pk}^2 expressed by (4-8) is now substituted in (4-4) it follows:

$$P_e = \frac{C_e}{2\pi^2}\left[dB(t)/dt\right]_{rms}^2 \tag{4-9}$$

If a new eddy-current loss coefficient $C_{e1} = \frac{C_e}{2\pi^2}$ is introduced, the expression for eddy-current loss will be:

$$P_e = C_{e1}\left[dB(t)/dt\right]_{rms}^2 \tag{4-10}$$

Please note that C_{e1} is a constant and (4-10) can be used for arbitrary-shaped flux density waveforms $B(t)$.

Fourier Series Analysis Method

Using Fourier series analysis it is known that any periodic function in time $g(t)$ can be expressed as a sum of sine and cosine functions starting from the *1*-st up to the *n*-th harmonic, where $n \to \infty$ as follows:

$$g(t) = \frac{a_0}{2} + \sum_{n=1}^{\infty}\left[a_n \cos(2\pi fnt) + b_n \sin(2\pi fnt)\right] \tag{4-11}$$

If $g(t)$ is a periodic function of t with a period of *T*, then the harmonic coefficients a_n and b_n are:

$$a_n = \frac{2}{T}\int_0^T g(t)\cos(2\pi fnt)dt \tag{4-12}$$

$$b_n = \frac{2}{T}\int_0^T g(t)\sin(2\pi fnt)dt \tag{4-13}$$

where $n=1, 2, \ldots$

From equation (4-4) it follows that the eddy-current loss is proportional to both B_{pk}^2 and f^2. So if the magnetic flux density waveform $B(t)$ is known, then according to (4-12) and (4-13) it is possible to calculate the magnitude of each individual harmonic component of the magnetic flux density $B_{pk\,n}$ where:

$$B_{pk\,n} = \sqrt{\left(a_n^2 + b_n^2\right)} \tag{4-14}$$

The total eddy-current loss can then be calculated as the sum of the eddy-current losses for the each of the flux density harmonic components.

4.2 Open- and Short-Circuit Stator Tooth Flux Waveforms

To better understand the stator iron losses, the magnetic flux variation in the stator teeth was examined using both finite-element analysis and experimental measurements.

4.2.1 Finite Element Predictions

Figure 4-2 is a diagram showing a quarter of the cross-section area of the concept demonstrator machine. Points 1 to 10 are the middle points of the stator slot openings. Finite-element analysis is used to calculate the vector potential at each of the points for a particular moment in time, while the loops represent the flux in each stator tooth. The tooth flux is calculated as the difference between the vector potential values in the stator slot openings on each side of the tooth. The magnetic flux density $B(t)$ is then calculated as the tooth flux divided by the cross-section area of the tooth.

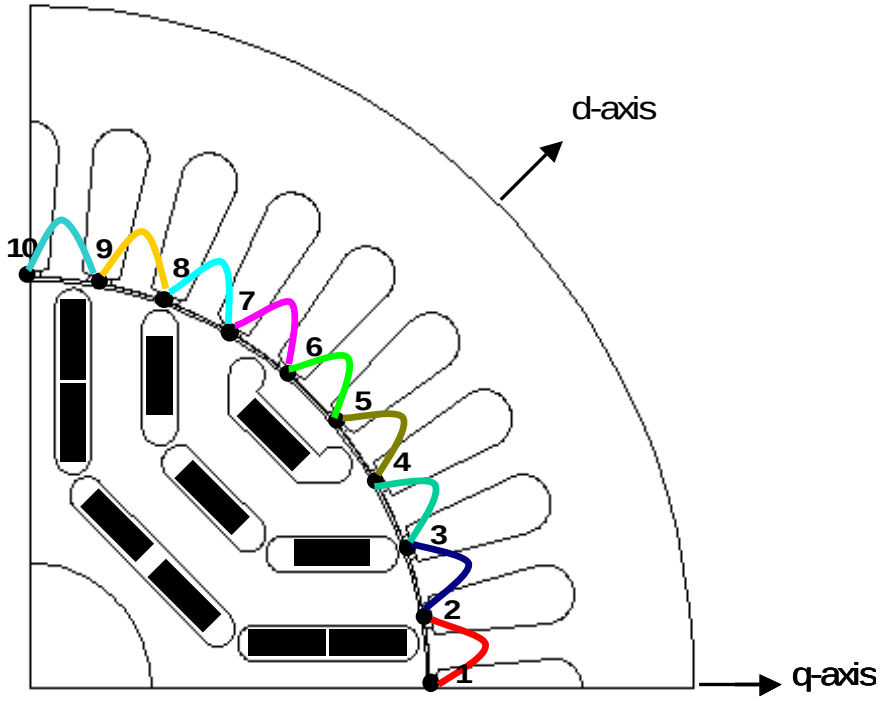

Figure 4-2 Diagram showing a quarter of the cross-sectional area for the concept demonstrator machine. Points 1 to 10 are the mid-stator slot openings.

The finite-element analysis was done for two operating conditions. Under the open-circuit condition there is no stator current, so the flux in the machine is due to the rotor magnets only. On the otherhand the short-circuit condition models having all three phases shorted across the machine terminals and the resultant flux is produced by two opposing flux components:

- flux caused by the negative *d*-axis rated stator current (9.4A) and
- flux due to the rotor magnets.

The short-circuit condition corresponds to field-weakening operation. In the finite-element-analysis it is modelled by using I_d= -9.4 A and I_q= 0 A. This operating condition was obtained as follows. In the quarter machine model (see Fig. 4-3), the middle three slots correspond to the phase A winding and the outer three slots on each side to the B' and C' windings. The phase A winding current was set to $\sqrt{2}$ ×9.4 A while B' and C' windings each carried half of this value. Finally the rotor was positioned as shown in Fig. 4-3b.

The stator tooth flux waveform was calculated using the finite-element package by rotating the rotor in 1° (mechanical) steps. Figure 4-3 shows flux plots for the open and short-circuit cases using the rotating finite-element model for a particular rotor position.

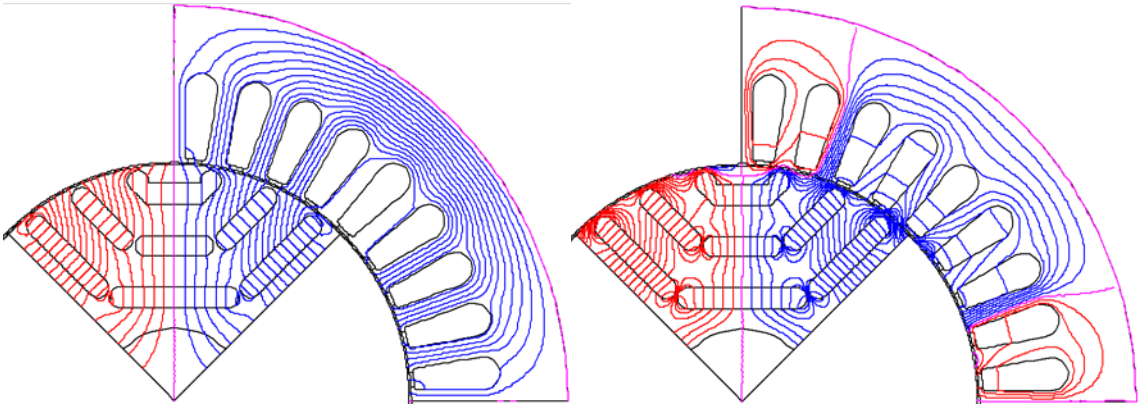

(a) Open-circuit case (b) Short-circuit case

Figure 4-3 The rotating FEA models used in the simulations.

4.2.2 Experimental Measurements

The variation of the stator tooth flux density under open-circuit and short-circuit conditions was measured using a search coil wound around a stator tooth. To obtain the stator tooth flux associated with the air gap flux, it is important to insert the search coil as close as possible to the air gap. The location of the search coil is illustrated in Figure 4-4a.

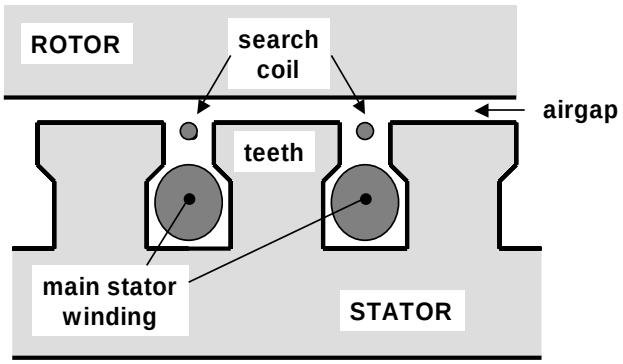

a)

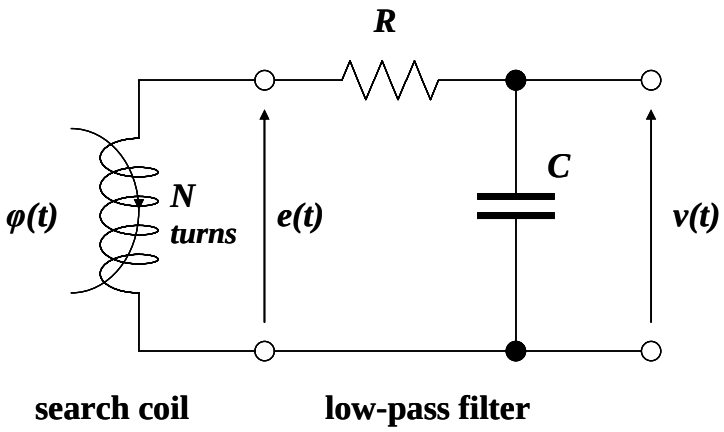

b)

Figure 4-4 a) Diagram showing the location of the stator tooth flux search coil and b) method for obtaining the tooth flux waveform using low-pass filter with cut-off frequency of 5 Hz.

The search coil spans a single stator tooth and consists of five turns of fine wire. The stator tooth flux waveform was obtained by integrating the search-coil induced voltage. This was performed using a resistor-capacitor first-order low-pass filter whose cut-off frequency of 5 Hz is much lower than the 50 Hz fundamental frequency. From Figure 4-4b follows:

$$v_i(t) = \frac{1}{R_i C_i}\int e(t)dt = \frac{N}{R_i C_i}\varphi(t) \tag{4-15}$$

where:

$v_i(t)$ output of the integrator,

$R_iC_i = 0.033$ s time constant of the low-pass filter, and

N number of turns in the search coil (in this case $N=5$).

So the flux in the tooth is equal to:

$$\varphi(t) = v_i(t)\frac{R_i C_i}{N} \tag{4-16}$$

4.2.3 Comparison of Calculated Results and Measurements

Figure 4-5 shows shaded flux density plots for a particular rotor position for the open- and short-circuit cases. Note that this rotor position is different to that shown in Figure 4-3. The lighter shading (actually red in colour) corresponds to regions of highest flux density. Figure 4-5a shows that under open-circuit conditions, the highest flux densities occurs in the stator teeth, in parts of the stator back-iron and in some of the rotor barriers. Figure 4-5b shows that under short-circuit conditions, the flux in the machine is much lower in general, however there are still high flux densities around the immediate vicinity of the air gap and in two of the stator teeth in each pole. The high flux densities in the saturated rotor bridges are also evident.

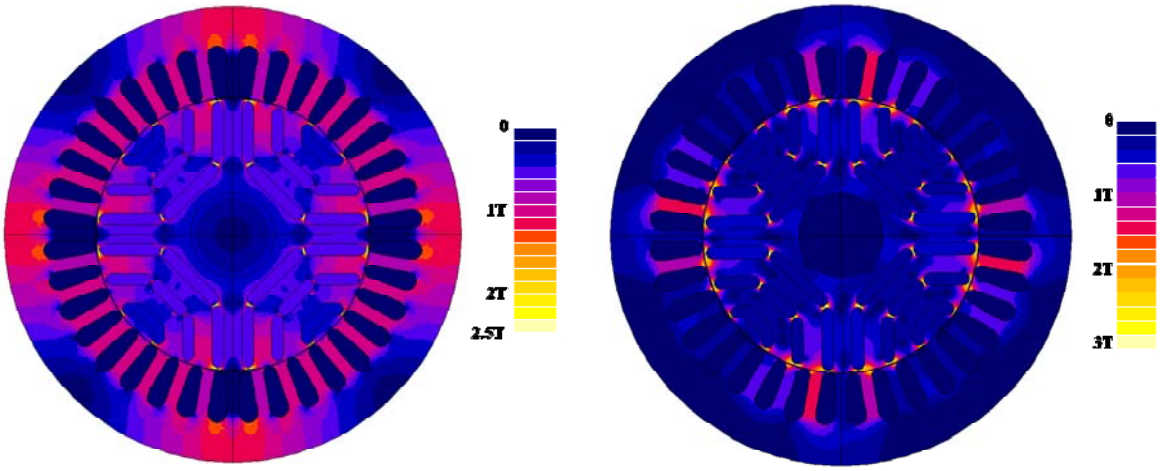

(a) Open-circuit case (b) Short-circuit case

Figure 4-5 Flux density distribution of the concept demonstrator. a) Open-circuit and b) short-circuit (field-weakening) conditions.

Figure 4-6 shows a comparison of the measured and the calculated search coil voltage and tooth flux for the open-circuit and short-circuit cases respectively at 1,500 rpm (50 Hz). In the open-circuit case in Figure 4-6, the measured flux waveform is roughly rectangular and shows a significant asymmetry. This is likely to be due to either an asymmetrical magnetization/placement of the rotor magnets, or local de-magnetization due to the field-weakening operation. Avoiding de-magnetization is important in this machine, which is operated near the short-circuit condition, and it is planned to investigate this issue further in the future. Apart from this asymmetry, the magnitudes and shapes of the calculated waveforms match well with the measured results.

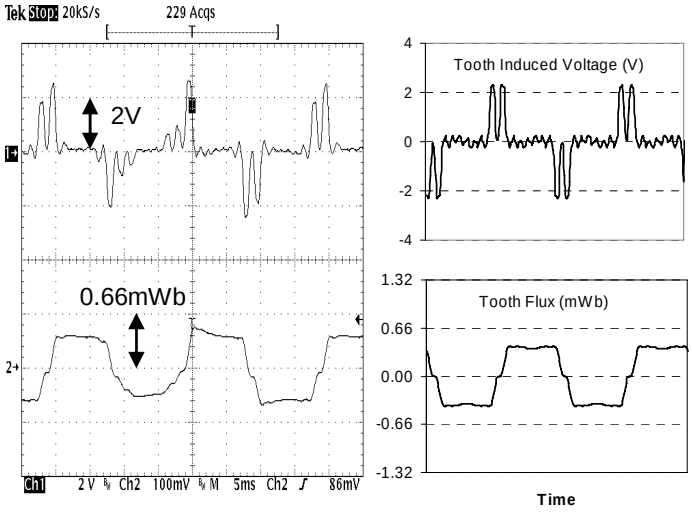

Figure 4-6 Open-circuit case. Search coil induced voltage (upper graphs) and corresponding stator tooth flux waveform (lower graphs) at 1,500 rpm. Measured (left) and calculated from finite-element analysis (right).

In the short-circuit case in Figure 4-7, ideally the tooth flux should be zero. In practice, the fundamental component of the tooth flux is reduced significantly compared to the open-circuit case, however there are now large harmonic components present. These components are particularly apparent in the induced voltage waveform. The high amplitude of these harmonic flux components is likely to cause high iron losses in the stator teeth. The finite-element results again show a good correspondence with the measured results both in magnitude and waveform shape.

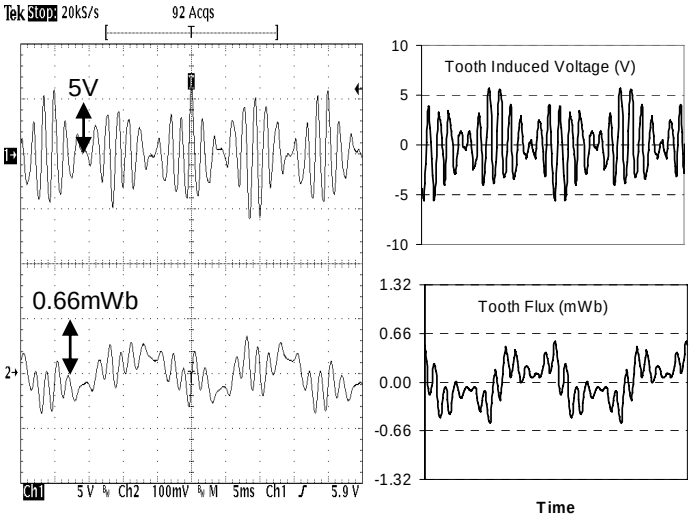

Figure 4-7 Short-circuit case. Search coil induced voltage (upper graphs) and corresponding stator tooth flux waveform (lower graphs) at 1,500 rpm. Measured (left) and calculated from finite-element analysis (right).

The calculated stator tooth flux ϕ waveforms in Figures 4-6 and 4-7 were divided by the area of the tooth A to obtain the tooth flux density $B = \phi/A$ waveforms in Figure 4-8 for the open and short-circuit cases. These waveforms were used in the next section to calculate the iron loss in the stator teeth.

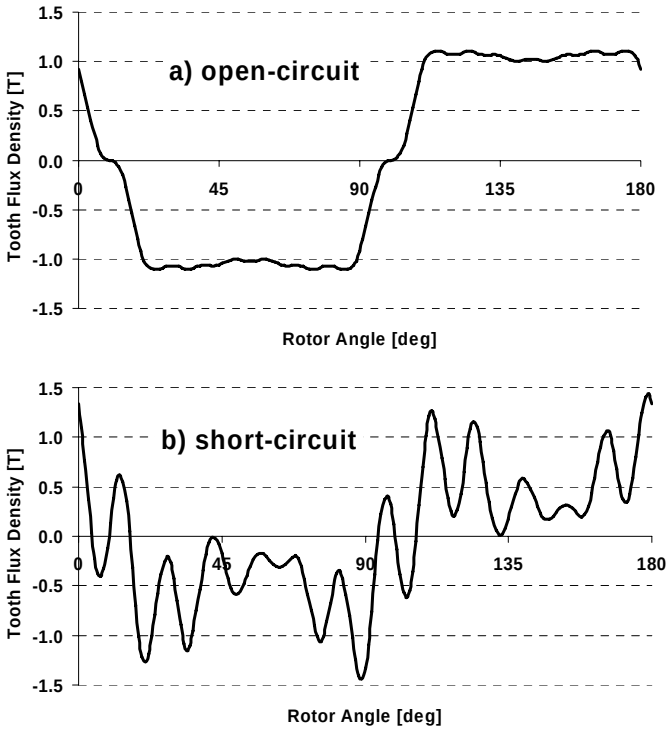

Figure 4-8 Calculated a) open-circuit and b) short-circuit tooth flux density versus time (rotor angle).

4.3 Stator Teeth Iron Loss

The majority of iron losses in synchronous machines normally occur in the stator, as ideally the rotor does not see a changing magnetic field. From Figure 4-5b (short circuit case) it could be seen that the majority of the high flux density regions are concentrated in and around the stator teeth. So FEA is used to calculate the iron loss in particular for these regions of the stator.

4.3.1 Finite Element Predictions

From the calculated stator teeth flux density waveforms, the maximum and minimum peak values are determined and their difference is divided by two in order to obtain the peak value. The peak values of all stator teeth are then averaged. This is used in the equation (4-4) in order to calculate the hysteresis loss in each stator tooth. The total hysteresis loss in the stator teeth is found by multiplying this by the mass of one tooth and the total number of stator teeth

The derivative of $B(t)$ in time can be written as:

$$\frac{dB(t)}{dt} = \frac{dB}{d\Theta} \times \frac{d\Theta}{dt} = \frac{dB}{d\Theta} \times \omega = 2\pi f \times \frac{dB}{d\Theta} \tag{4-17}$$

If the equation (4-16) is squared, it follows:

$$\left[\frac{dB(t)}{dt}\right]^2 = \omega^2 \left[\frac{dB}{d\Theta}\right]^2 = 4\pi^2 f^2 \left[\frac{dB}{d\Theta}\right]^2 \tag{4-18}$$

From the calculated $(dB/dt)^2$ waveform for each stator tooth the average value of $(dB/dt)^2$ is determined. This is repeated for each stator tooth and the results averaged. This value is used in equation 4-10 in order to calculate the eddy-current loss in the stator teeth. It is important to emphasize that the iron loss calculations are only performed for the stator teeth and not for the rest of the machine.

4.3.2 Comparison of Calculated Results and Measurements

The iron loss in the stator teeth was calculated using the tooth flux density waveforms in Figure 4-8 and equation (4-10) for both the open and short-circuit cases. Figure 4-9 presents a comparison of the calculated iron loss in the stator teeth with the measured total iron and mechanical losses for the concept demonstrator machine. Under open-circuit conditions, the calculated stator tooth losses make up only 30% of the total losses. This is not surprising as in Figure 4-5a, the stator yoke shows high magnetic flux density and hence iron loss. Under short-circuit conditions the calculated stator loss is close to the measured losses. Figure 4-5b shows that this is reasonable as the flux density in the stator yoke is much smaller than in the teeth.

It was found that the eddy-current loss was dominant in this machine at higher speeds. At 6,000 rpm (200 Hz), the hysteresis loss was about 10% of the total loss under open-circuit conditions and only about 2% of the total loss under the short-circuit conditions.

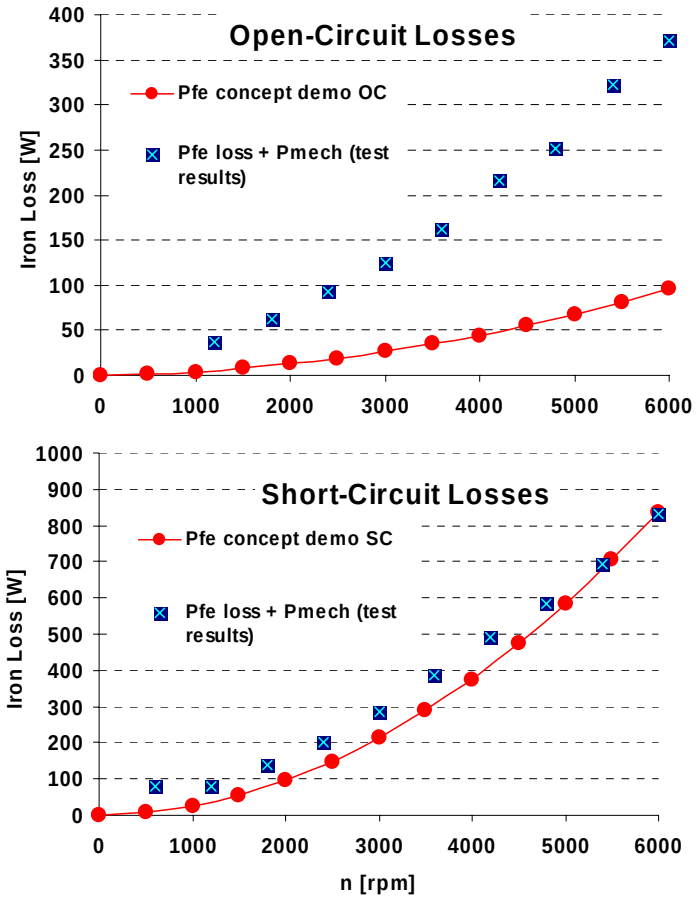

Figure 4-9 Comparison of measured iron and mechanical loss (squares) and calculated finite-element stator tooth losses (lines) versus speed for the concept demonstrator.

An alternative method for calculating the iron loss is to perform a Fourier series analysis of the stator tooth flux density waveforms shown in Figure 4-8 to obtain the amplitude of each flux density harmonic component. Equation (4-14) can then be used to calculate the iron losses for each harmonic. This has the advantage of showing the relative contributions of the different frequency components to the stator tooth iron loss.

The frequency spectrum of the tooth flux density and the eddy-current loss for each harmonic at 6,000 rpm (200 Hz), are shown in Figures 4-10 and 4-11 for the open-circuit and short-circuit cases respectively. Only the eddy-current loss is considered as the earlier analysis showed that this is much larger than the hysteresis loss at higher speeds. Note that only odd harmonics are present due to the symmetry of the waveforms.

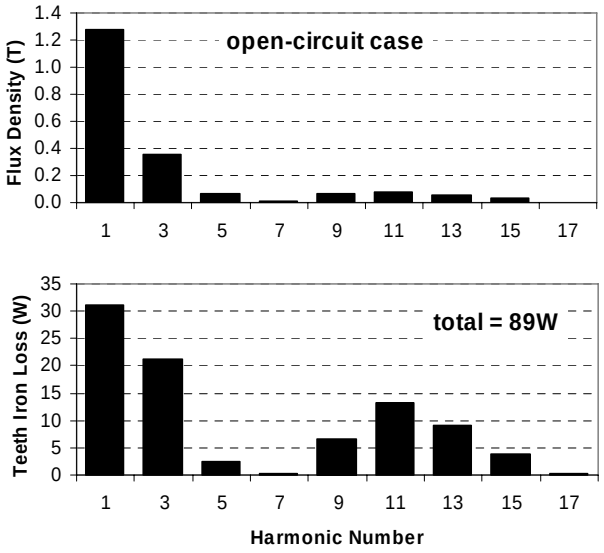

Figure 4-10 Open-circuit case. Harmonic components of the calculated tooth flux density waveform (upper) and the teeth eddy-current iron loss at 6,000 rpm (lower).

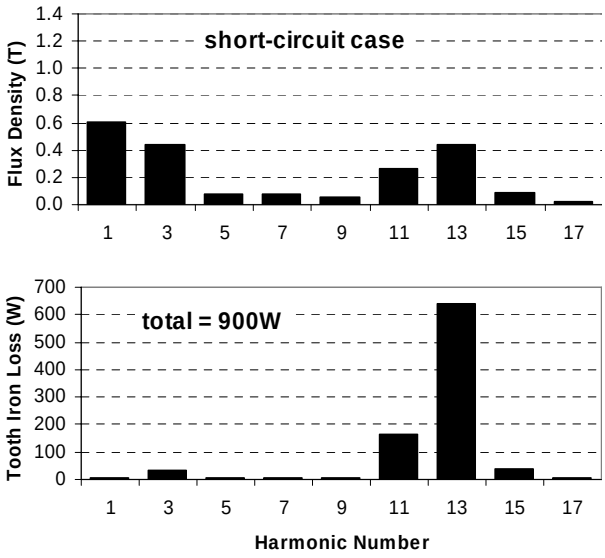

Figure 4-11 Short-circuit case. Harmonic components of the calculated tooth flux density waveform (upper) and the teeth eddy-current iron loss at 6,000 rpm (lower).

Figure 4-10 shows that under open-circuit conditions the tooth flux density waveform has a predominant fundamental component while the other harmonics are relatively small in amplitude. From equation (4-4) the eddy-current iron loss is proportional to both flux density squared and frequency squared. Thus low amplitude, higher harmonic components can still produce significant iron losses due to their high frequency. This can be seen in Figure 4-10 where though the fundamental iron loss is the largest component, it only makes up one third of the total eddy-current losses and that the 3^{rd}, 9^{th}, 11^{th}, 13^{th} and 15^{th} harmonic iron loss components are significant. The total calculated eddy-current loss of 89 W using harmonic

analysis is comparable to the calculated eddy-current iron loss of 86 W using the *dB*/*dt* formula in equation (4-10).

Figure 4-11 shows under short-circuit conditions, that the fundamental component of the tooth flux density is halved, while the higher harmonic components increase in amplitude. In particular, the 13th flux density harmonic becomes almost comparable in magnitude to the fundamental component. As the eddy-current loss is proportional to frequency squared, this results in an extremely large iron loss due to this harmonic. It is responsible for nearly two-thirds of the total eddy-current loss. Again, the total calculated stator tooth eddy-current loss of 900 W using harmonic analysis is comparable with the calculated eddy-current iron loss of 820W using the *dB*/*dt* formula in equation 4-10.

4.4 Conclusions and Findings

In this chapter the background theory of iron losses was presented followed by a comparison of the measured and calculated tooth flux waveforms and eddy-current loss in the stator teeth under open- and short-circuit conditions. The main results were as follows:

- The measured tooth flux search coil waveforms under open- and short-circuit conditions were compared to the finite-element predictions and showed a good match.
- The calculated tooth flux waveforms were then used to estimate of the eddy–current losses in the stator teeth with both *dB*/*dt* and Fourier spectra analysis methods.
- Under open-circuit conditions, the calculated stator teeth iron loss was only about 30% of the total losses, but the calculated short-circuit stator-tooth losses were much closer to the measured total losses.
- The presence of high-frequency harmonic components of the tooth flux density waveform is directly related to the high eddy-current loss in this machine under short-circuit conditions.

The following chapter will use finite element analysis as a tool to predict the parameters and performance of three modified machine designs based on the concept demonstrator with the aim to find the best solution for eddy-current loss reduction under field-weakening operation.

Chapter 5 Finite-Element Analysis of the Three New Designs

The analysis described in previous chapters has revealed that the reason for high iron losses in the concept demonstrator machine during field-weakening is the presence of high-frequency flux density harmonic components, particularly in the stator teeth. It was experimentally confirmed that under field-weakening conditions, the iron loss in the machine at high speeds could be reasonably accurately estimated from the stator tooth flux density waveform. The eddy-current loss was found to be much larger than the hysteresis loss due to the high frequencies considered.

In this chapter the effect of three design changes to the concept demonstrator design with the aid of FEA will be observed and their impact on the field-weakening iron loss will be calculated. These changes affect the stator winding, stator tooth and rotor barrier design. Figure 5-1 illustrates these three design modifications from left to right as follows:

1. FLAT STATOR TEETH. The tips of the stator teeth were cut in a manner to form flat-sided teeth in an attempt to reduce the zigzag leakage flux. This means that the stator slot openings were widened to an 'open slot' configuration as is shown in Figure 5-1a.

2. NEW ROTOR DESIGN. The size and shape of the smallest and the closest rotor barrier to the air gap was changed to allow space for an additional magnet to be inserted as shown in Figure 5-1b. The positions of the other rotor barriers were slightly modified in the process. The aim was an improvement of the shape of the air gap flux distribution due to the rotor magnets.

3. IDEAL STATOR WINDING. The existing concept demonstrator design is based on a three-phase single-layer stator winding. In an attempt to improve the stator *d*-axis armature reaction air gap flux density distribution, the effect of using a nine-phase single-layer winding was tested. In this winding, the electrical phase angle of the stator current waveform changes 20º between every slot as shown in Figure 5-1c.

The aim was to use finite-element analysis to investigate how each of these changes would affect the machine parameters like the back-EMF, and the open- and short-circuit iron losses.

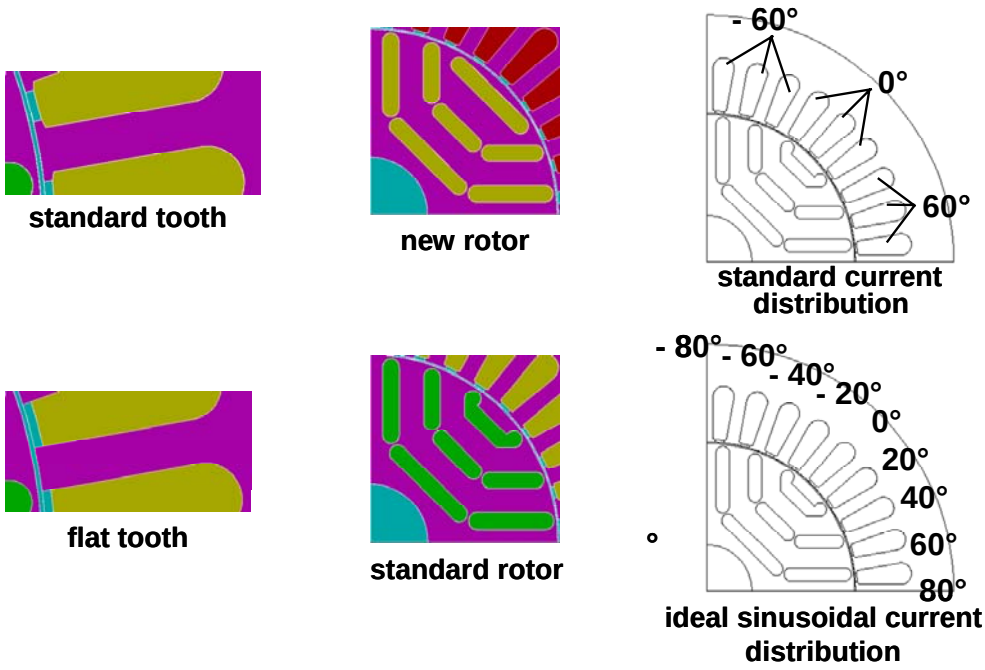

a) b) c)

Figure 5-1 Three proposed design changes to the concept demonstrator machine: a) Flat teeth (open slots), b) new rotor and c) 9-phase sinusoidal current distribution.

5.1 Back-EMF Analysis

Figure 5-2 presents the phase back-EMF waveforms and their frequency spectra for the concept demonstrator, new rotor and flat stator teeth designs.

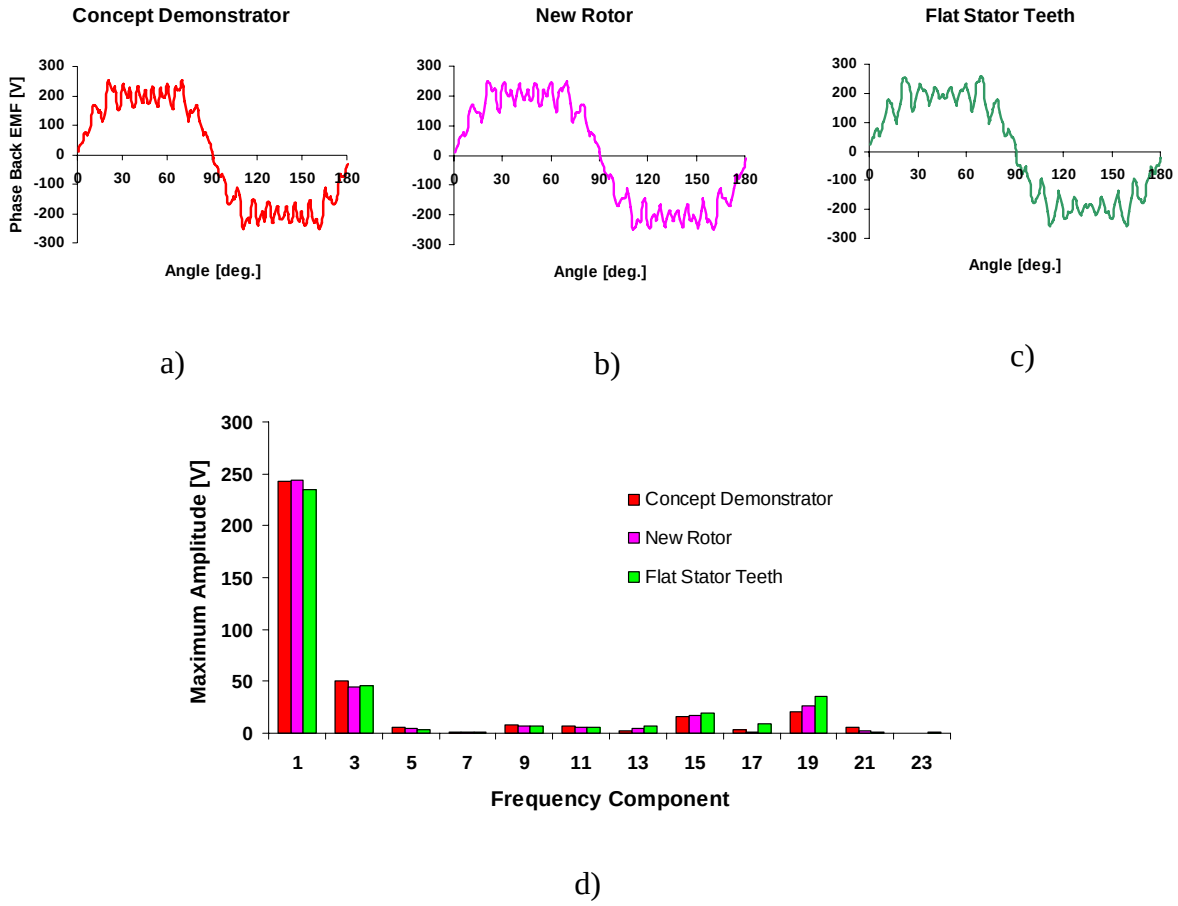

Figure 5-2 Calculated back EMF waveform for a) concept demonstrator, b) new rotor, c) flat stator teeth and d) frequency spectra for three designs.

As the new stator winding machine has a nine-phase stator, it is difficult to compare its back-EMF waveform with the other three-phase machines and so it is not shown. The frequency analysis of the back EMF shows that there are no major changes in the amplitudes of the frequency components for all three designs. This analysis also reveals the following:

- the fundamental component of the back EMF for the new rotor design is slightly higher in comparison to the concept demonstrator and flat stator teeth designs,
- the most dominant harmonics apart from the fundamental one are the 3rd, 19th and 15th harmonics for all three designs, and
- the 19th and 15th harmonic have the highest amplitude for the flat stator teeth design.

5.2 Open-Circuit Iron Loss Performance

Figure 5-3 shows the flux plots, the air-gap radial flux distribution, the tooth flux density versus time waveforms, the flux density spectra and the iron loss spectra for the three new

designs under open-circuit conditions. As for the third case – the ideal sinusoidal winding stator current is zero, so this case is actually equivalent to the concept demonstrator in open-circuit operation.

The finite-element flux plots for the three designs under the open-circuit condition are not significantly different. The radial air gap flux density graphs show a largely rectangular waveform, which is modulated by the slot openings and are similar to the concept demonstrator case. The fundamental components of the air gap flux density waveforms have similar amplitudes (0.65-0.67 T) in all three designs. Note that cutting the tips of the stator teeth has increased the width of the stator slot openings, which increases the depth of the dips and the peak values of the radial flux density at the teeth edges. The tooth flux density waveforms as a function of time are rectangular shaped with some small differences around their flat tops. The calculated flux density frequency spectra all show a dominant fundamental component with relatively small harmonics.

The eddy-current loss is proportional to both the flux density squared and frequency squared; so the low-amplitude higher harmonic components can still produce significant iron losses due to their high frequencies. This can be seen in Figure 5-3 where though the fundamental iron loss is the largest amplitude component, and it only makes up only roughly one third of the total eddy-current losses for all three machine designs. The second most significant flux density frequency component is the 3^{rd} harmonic, followed by the 11^{th}, 13^{th} and 9^{th} harmonic components. The total eddy-current losses at 6000 rpm are shown in Figure 5-3 for each design. Two eddy-current loss figures are provided, the first based on the harmonic analysis and the second (in brackets) based on the *dB*/*dt* method. Both methods give comparable results.

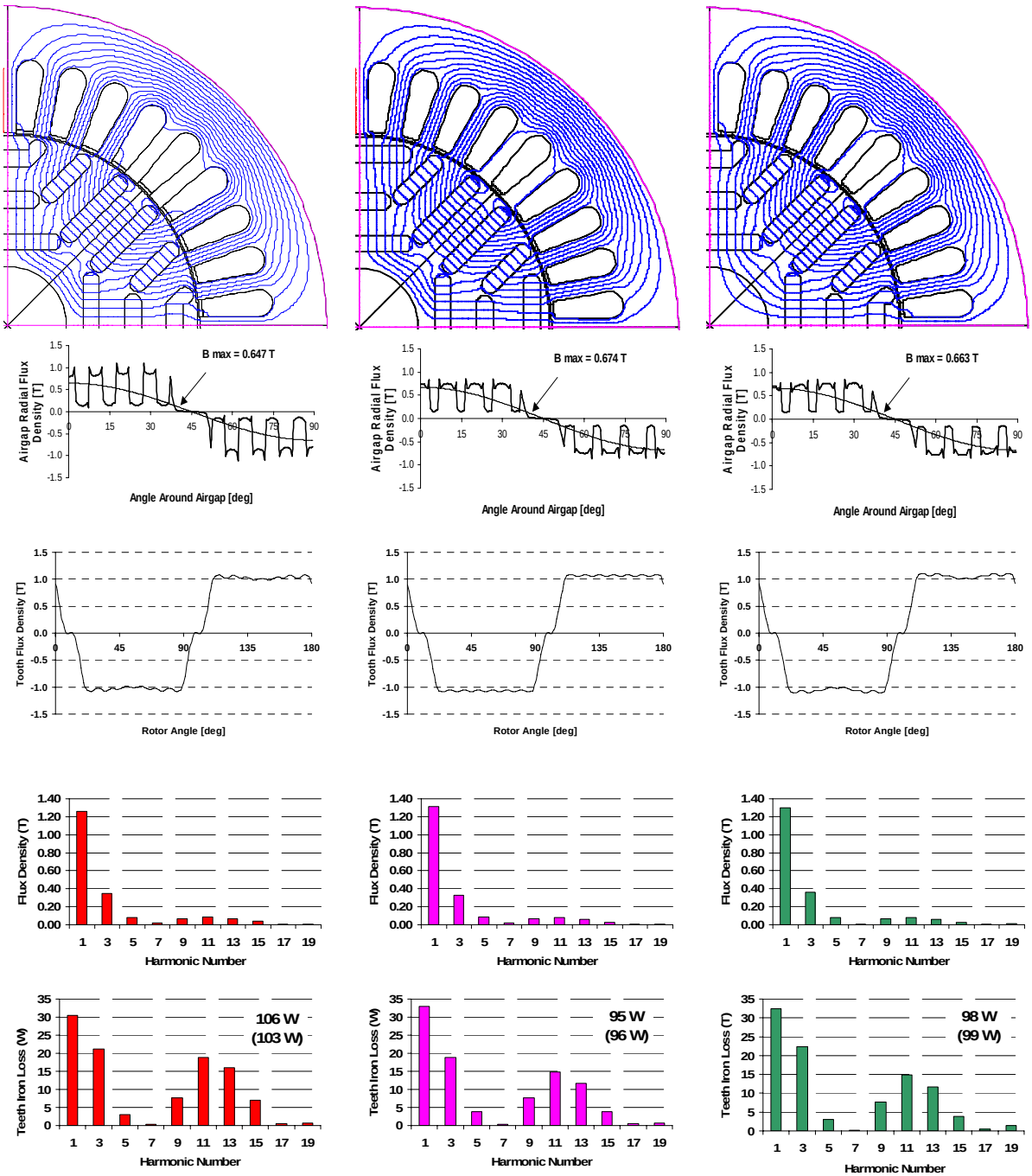

(a) Flat tooth stator (b) New rotor design (c) Ideal stator winding

Figure 5-3 Open-circuit performance. Comparison of a) flat tooth stator, b) new rotor design, and c) ideal stator winding designs. FEA flux plots (top), air gap radial flux distribution with fundamental component, tooth flux density as a function of rotor angle, harmonic components of the calculated tooth flux density and harmonic components of the calculated teeth eddy-current loss at 6000rpm.

Figure 5-4 presents a comparison of the calculated iron loss between the new designs and the concept demonstrator under open-circuit condition using the *dB*/*dt* calculation method. There are only slight differences between the open-circuit iron losses.

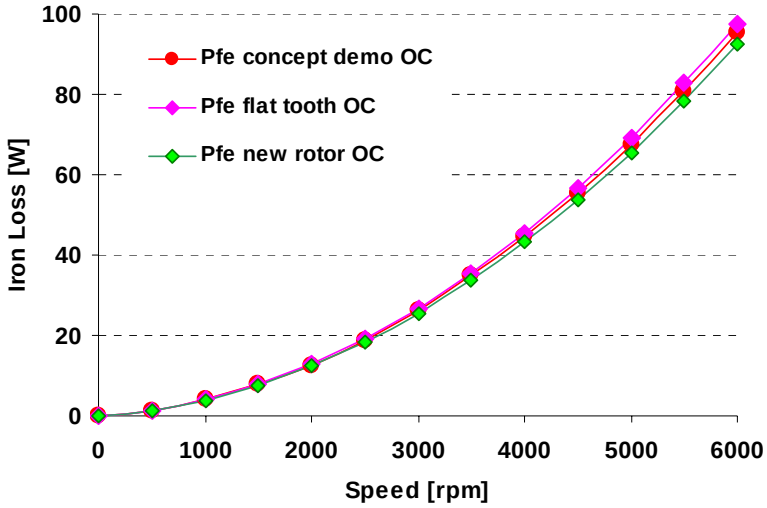

Figure 5-4 Open-circuit case. Comparison of the calculated stator tooth iron loss between two of the new designs with the calculated concept demonstrator result.

Compared to the concept demonstrator, the flat stator teeth case shows slightly higher iron loss and the new rotor design shows slightly lower iron loss. The ideal stator winding design has identical losses to the concept demonstrator under open-circuit condition and is not shown.

5.3 Short-Circuit Iron Loss Performance

Figure 5-5 shows the flux plots, the air-gap radial flux distribution, the stator tooth flux density versus time waveforms, the flux density spectra and the iron loss spectra for the flat-tooth, new rotor and ideal stator winding designs under short-circuit conditions. Figure 5-6 shows a similar comparison between the flat-tooth stator and the concept demonstrator machine. All the short-circuit finite-element flux plots of the four designs under the short-circuit condition show signs of high saturation in the rotor bridges, in the vicinity of the air gap on the rotor side, and through some of the stator teeth. Note that the flux lines through the stator teeth are differently distributed for all four cases, and the most even distribution of the flux lines is obtained for the flat stator teeth design. This may be due to reduced leakage flux.

The radial air gap flux density graphs all show large amplitude harmonics similar to the concept demonstrator case. The fundamental component of the flux density is much lower compared to the open-circuit case: for the flat rotor teeth design it is 0.191 T, for the new rotor design it is 0.226 T and for the ideal stator winding it is 0.175 T. As was found with the concept demonstrator design, under field-weakening conditions the air gap radial flux density distribution of all three designs shows large peaks in the vicinity of 45°. The tooth flux density waveforms as functions of time also show large amplitude harmonics with distinctive differences in the waveform shapes between 40º to 80º and 130º to 170º. These differences are reflected in their calculated frequency spectra. The fundamental component is dominant in the flux density spectra of the new rotor and flat teeth designs, while the third harmonic component is dominant for the ideal stator winding. Although the flat tooth flux density harmonics spectrum is similar in shape to the concept demonstrator one, it shows slightly lower harmonics amplitudes. For the new rotor design the 3^{rd}, 11^{th} and 13^{th} flux density harmonics are significantly smaller while remaining harmonics are larger. The ideal stator winding design has the factor of three reduction in the fundamental component, while other components show only small changes in amplitude.

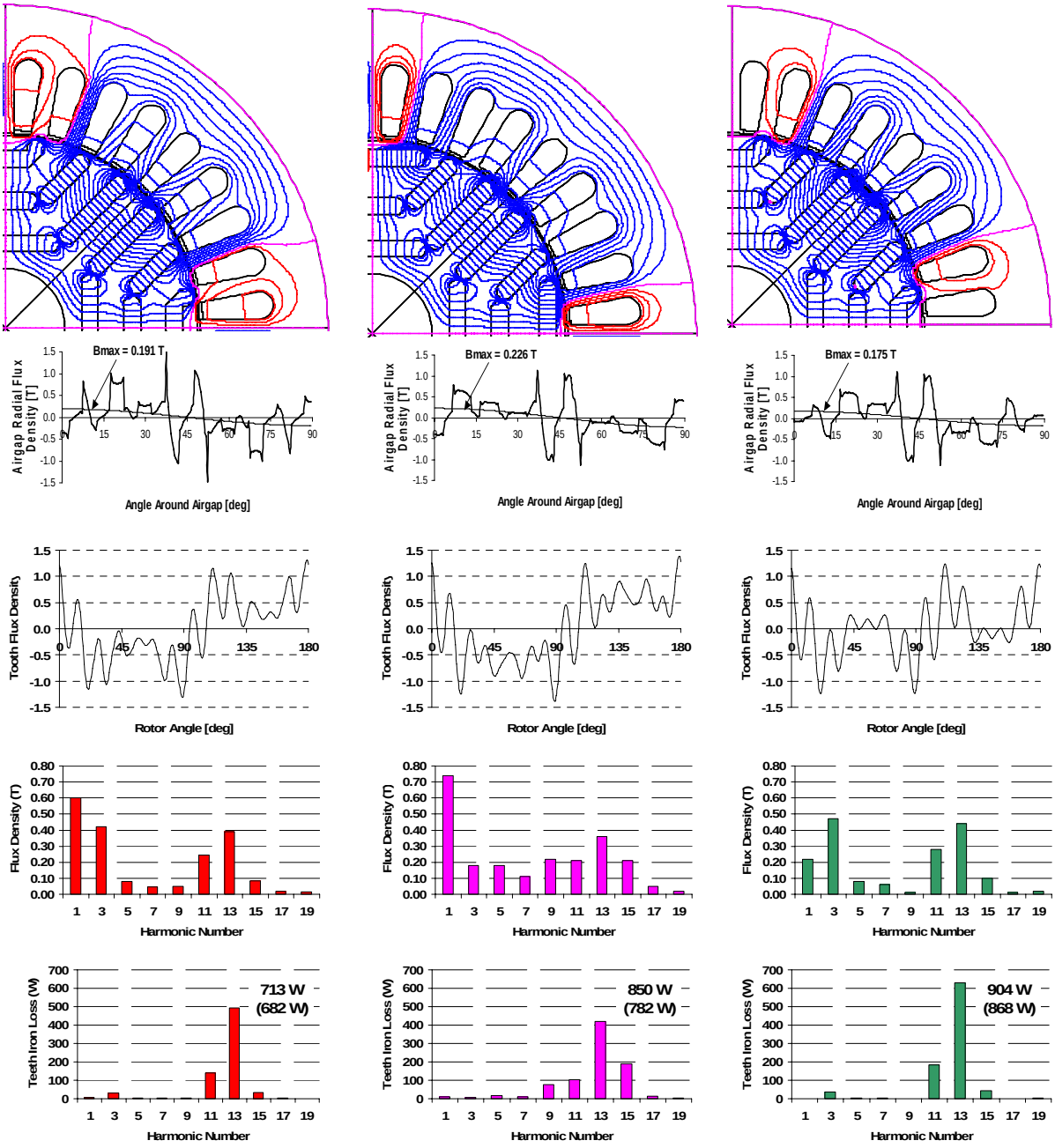

a) Flat tooth stator

b) New rotor design

c) Ideal stator winding equivalent to concept demonstrator.

Figure 5-5 Short-circuit performance. Comparison of a) flat tooth stator, b) new rotor design, and c) ideal stator winding designs. FEA flux plots (top), air gap radial flux distribution with fundamental component, tooth flux density as a function of rotor angle, harmonic components of the calculated tooth flux density and harmonic components of the calculated teeth eddy-current loss at 6000rpm.

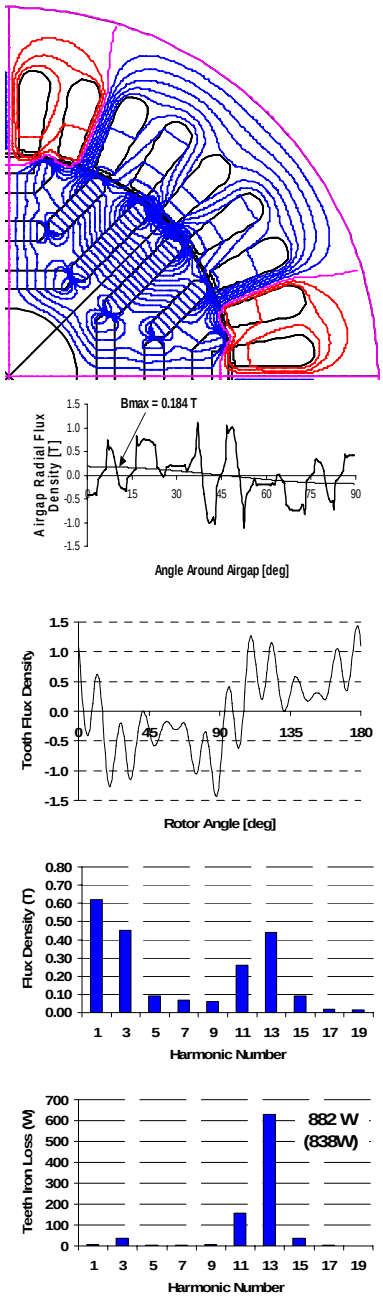

a) Concept demonstrator

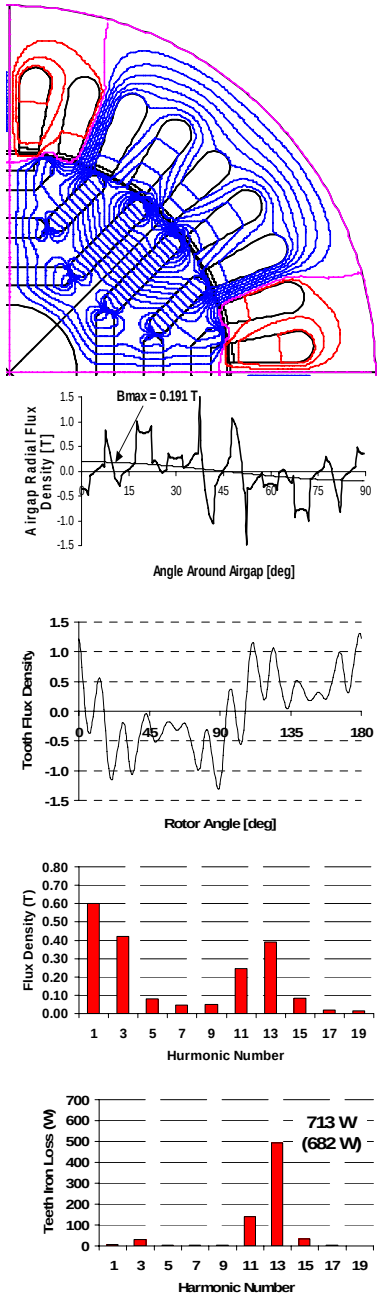

b) Flat tooth stator

Figure 5-6 Short-circuit performance. Comparison of a) concept demonstrator and b) flat tooth stator design. FEA flux plots (top), air gap radial flux distribution with fundamental component, tooth flux density as a function of rotor angle, harmonic components of the calculated tooth flux density and harmonic components of the calculated teeth eddy-current loss at 6000rpm.

The calculated frequency spectra of the eddy-current iron loss for all four designs show the dominant 13th harmonic component that represents more than half of the total eddy-current losses. The 11th harmonic component is generally next except for the new rotor design. The 13th harmonic of the eddy-current loss is the largest for the concept demonstrator and ideal stator winding designs, but drops significantly to 500W for the flat teeth and to 400W for the new rotor design. As the new rotor design has a significant 15th harmonic component of 200W, the flat tooth stator design has the lowest total eddy-current loss of all.

Figure 5-7 presents a comparison of the calculated iron loss between the new designs and the concept demonstrator under short-circuit conditions as a function of speed. The calculated short-circuit stator teeth iron loss results for the new designs show that compared to the original design, the iron loss increases by 3.3% for the ideal stator winding, reduces by 12% for the new rotor design and reduces by 19% with the flat teeth stator design. These calculations show that a significant reduction of iron loss is possible by using flat stator teeth and changing the rotor barrier shape.

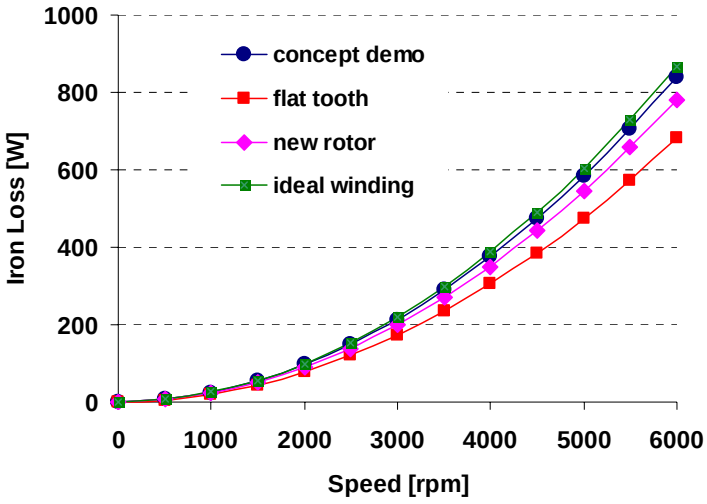

Figure 5-7 Short-circuit case. Comparison of calculated stator tooth iron loss between the three new designs with the calculated concept demonstrator result.

Table 5-1 Comparison of the effect of machine design changes on the calculated iron losses and fundamental air gap components.

Parameter	Case	Concept Demo	Flat Teeth	New Rotor	Ideal Stator Winding
Calculated peak fundamental air gap magnetic flux density	open-circuit case	0.663 T	0.647 T	0.674 T	same as concept demo
	reluctance case *d*-axis stator flux only	0.512 T	0.502 T	0.495 T	0.525 T
	short-circuit case	0.184 T	0.191 T	0.226 T	0.175 T
Open-circuit loss at 6 krpm	Measured (iron+windage)	371 W	-	-	-
	Calculated (teeth only)	103 W	97.6 W	96 W	same as concept demo
Short-circuit loss at 6 krpm	Measured (iron+windage)	834 W	659 W*	-	-
	Calculated (teeth only)	838 W	682 W	782 W	868 W

* Measured value of the short-circuit iron loss (659W) for the flat teeth design is placed in the Table 5-1 for comparison and it will be discussed later.

Figure 5-7 and Table 5-1 present a comparison of the calculated iron loss between the three different designs and the concept demonstrator under short-circuit conditions. Table 5-1 also shows the fundamental component of the flux densities under open-circuit, reluctance, and short-circuit conditions. Note that the changes of the fundamental component of the flux density for the open-circuit and short-circuit cases from Table 5-1 do not correspond to the change in values of the calculated iron loss. For instance, although the calculated peak fundamental air gap magnetic flux densities of the concept demonstrator and the flat teeth designs under the short-circuit case are very close (0.184 T and 0.191 T), the calculated iron loss for the concept demonstrator is 838 W and 682 W for the flat teeth stator design. The new flat teeth design achieved a calculated total iron loss reduction of 19% at 6000 rpm under short-circuit conditions. It can be concluded that the presence of high-frequency harmonic flux components, particularly in the stator teeth during field weakening operation (equivalent to the short-circuit condition) are major contributors to the iron loss. By cutting the stator teeth the magnitude of these harmonics has been reduced, and hence reduced the iron losses.

5.4 Detailed Stator Tooth Flux Density Waveforms

It has been found that using flat stator teeth (open slots) in the concept demonstration machine design significantly reduces the iron losses in the stator teeth under field weakening operation. To investigate this further, the flux density waveforms were examined at a number of locations within the stator teeth as shown in Figure 5-8 for both the concept demonstrator and flat-tooth machine:

- point A – left hand side close to the tip of the tooth,
- point B – in the middle of the tooth, close to the air gap,
- point C – in the middle of the tooth, and
- point D – in the middle of the tooth, close to the root of the tooth.

The tangential and radial flux density waveforms were calculated for the short-circuit case in order to investigate the changes in the flux density direction and amplitude for each of the points mentioned above. These are presented in Figure 5-9. Table 5-2 presents a comparison of the corresponding calculated peak values of the tangential and radial flux density components for the two designs. Note that the flux density results presented were analysed at exactly the same geometrical points for both the concept demonstrator and flat stator teeth designs.

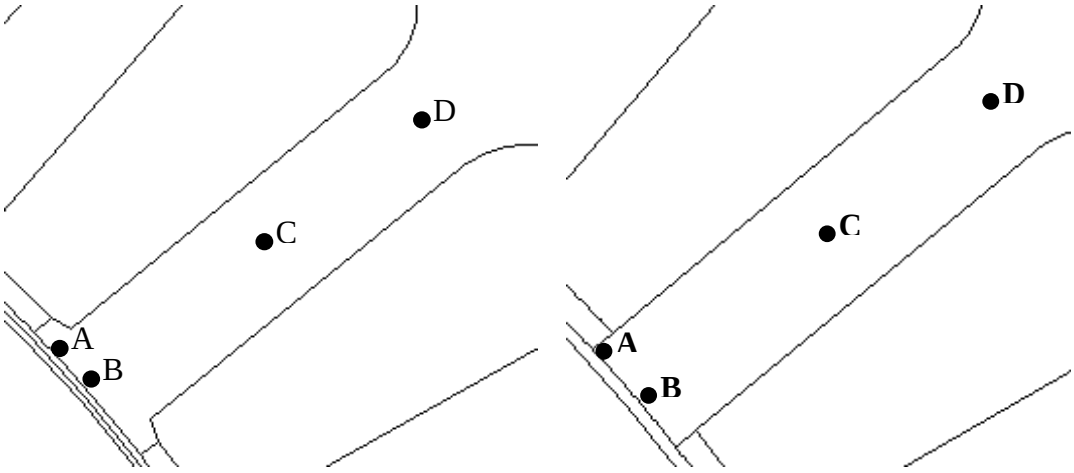

a) Concept Demonstrator b) Flat Teeth

Figure 5-8 Points of the flux density observations of a) the concept demonstrator machine and b) the flat teeth machine.

The comparison of the results at point A reveals that the major flux axis has an angle of 45° for the concept demonstrator but around 65° for the flat stator tooth design, with overall similar magnitude flux density and moderate rotational components.

At point B, both designs show large rotational components, although the flat tooth design shows a slightly more smooth and symmetrical pattern.

At point C, the radial component is dominant and the tangential component and rotational components are both small. The radial component has slightly smaller magnitude in the case of the flat teeth stator design.

At point D, there is nearly zero tangential component for both machines with a slight drop of the radial amplitude in the case of the flat teeth design similar to what was seen with point C.

Cutting the tips of the stator teeth increases the stator slot opening, which enlarges the effective air-gap, and results in the reduction of the rotor flux. The increased slot opening also reduces the stator slot leakage flux. Both these effects result in the reduction of the stator tooth flux.

Table 5-2 Comparison of the calculated peak values of the tangential and radial flux density components for the concept demonstrator and flat stator teeth designs.

MACHINE DESIGN	**Concept Demo Machine:**		**Flat Stator Teeth Machine:**	
Point of observation*:*	Tangential[T]	Radial [T]	Tangential [T]	Radial [T]
A	1.96	1.21	1.80	1.37
B	1.43	1.19	1.20	1.20
C	0.10	1.44	0.10	1.31
D	0.07	1.42	0.06	1.31

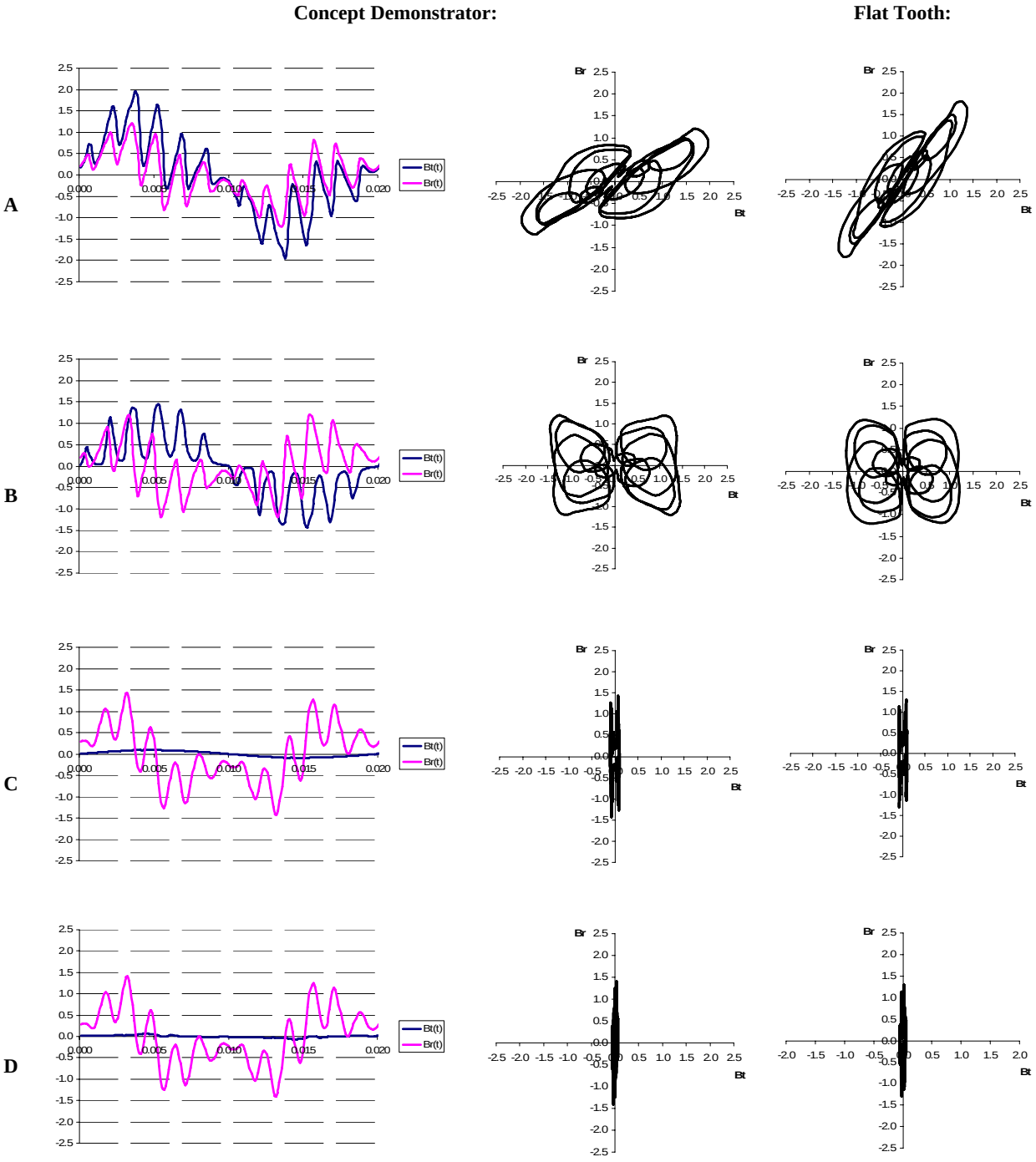

Figure 5-9 Short-circuit case. From the left to the right - points of the observation: A, B, C & D of both designs; Tangential $B_t(t)$ and radial $B_r(t)$ components of the flux density as a functions of time (concept demonstrator); Tangential $B_t(t)$ versus radial $B_r(t)$ characteristic (for both concept demonstrator and flat tooth designs).

5.5 Conclusions and Findings

In this chapter three machine design modifications to the concept demonstrator were examined using finite-element analysis including: flat stator teeth, new rotor and ideal stator winding. The main findings were as follows:

- There are no significant changes in the amplitudes of the back EMF frequency components for the three designs.
- Under the open-circuit condition, the flat stator teeth case compared to the concept demonstrator shows slightly higher iron loss, while the new rotor design shows slightly lower iron loss. The iron loss of the ideal stator winding design is identical to the concept demonstrator case.
- Under the short-circuit condition, the stator teeth iron loss results for the new designs show that compared to the concept demonstrator design, the iron loss increases by 3.3% for the ideal stator winding, reduces by 12% for the new rotor design and reduces by 19% with the flat teeth stator design. The significant iron loss reduction in the flat teeth design is due to reduction in the amplitudes of the high frequency stator tooth harmonics.
- The flux density waveforms examined at four different locations within the stator teeth showed that the radial and tangential components are both dominant on the side of the stator tooth close to the air gap, while the radial component becomes dominant near the yoke of the machine, while the tangential component becomes small.
- The stator slot opening is increased by cutting the tips of the stator teeth, which resulted in an enlarged effective air-gap. The stator slot leakage flux is reduced by the increased slot opening too. Both these effects result in the reduction of the stator tooth flux.

It can be concluded that using flat teeth in the concept demonstrator design can significantly reduce the calculated field-weakening iron losses.

The following chapter will cover the experimental testing and the further verification of the flat stator teeth design parameters and performance characteristics.

Chapter 6 Experimental Verification of Flat Stator Teeth Design

The FEA analysis in the previous chapter showed that the most significant calculated iron loss reduction under field weakening operation (the short-circuit condition) was obtained for the flat teeth design. This chapter describes the experimental verification of this result.

6.1 Experimental Procedure

The following series of experimental steps were performed, as shown in Figure 6-1. Firstly another stator, identical to that used in the concept demonstrator machine was obtained – see Figure 6-1a. Secondly the stator winding was heated in an oven to soften the varnish and slightly compressed into the slots to allow removing the tips of the stator teeth by machining without damaging the stator winding – see Figure 6-1b. Finally machining of the tips of the stator teeth was performed to produce flat teeth stator – see Figure 6-1c.

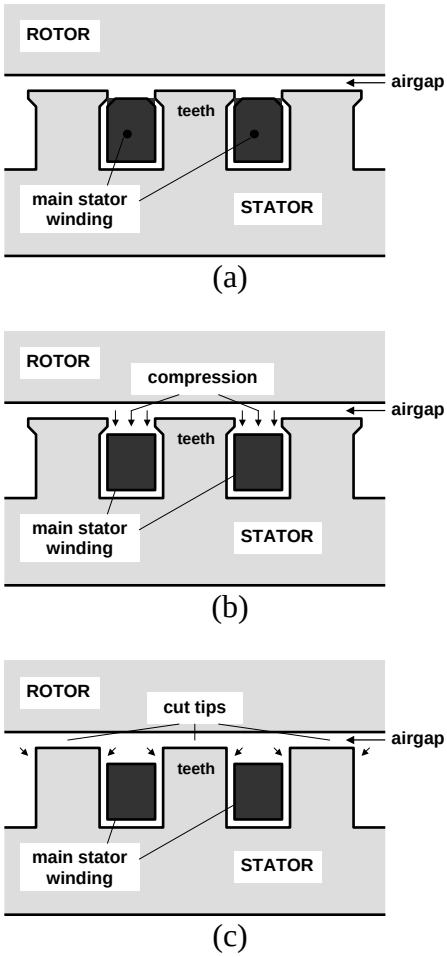

Figure 6-1 Diagrams showing a) original stator winding and teeth arrangement, b) after compression of stator winding and c) after cutting of stator teeth tips.

The inside of the stator showing the stator teeth: a) before compression of the stator winding and b) after compression and machining are presented in Figure 6-2. Note that in both cases search coils (not shown) have been wound to allow stator tooth flux measurements to be performed and compared with FEA calculated results.

Figure 6-2 The inside of the stator a) before compression of the stator winding and b) after compression and machining.

The concept demonstrator interior PM rotor was tested with each of the three stator configurations shown in Figure 6-1 to measure the following parameters: the *d*-axis inductance L_d, the *q*-axis inductance L_q, the back EMF magnitude, the open- and short-circuit iron losses, the tooth flux waveforms under open and short-circuit conditions, and the output power and efficiency versus speed characteristics.

6.2 Inductance Curves Comparison

The application of analytical methods is a useful first step in the prediction of the machine parameters and can give rough values for the *d*- and *q*-axis unsaturated inductances. Table 6-1 shows analytical estimates for the conventional teeth versus flat teeth stator design with a reluctance rotor. The conventional teeth stator analytical results were already presented in Chapter 3 (see Table 3-2), but do not include the end-winding inductance. The results presented in Table 6-1 include the end-winding inductances for both the conventional teeth and flat teeth stator and use the standard analytical inductance equations from [46]. The calculated FEA inductances are presented in Figure 6-3, while a comparison of the analytical, FEA and measured results is presented in Table 6-2.

Table 6-1 Comparison of the analytically calculated parameters - concept demonstrator versus flat stator teeth design with a reluctance rotor including end-winding inductances.

Parameter:	**Conventional Teeth Stator:**	**Flat Teeth Stator:**
Carter's coefficient:	1.315	1.507
Actual air gap [mm]:	0.39	0.39
Effective air gap *g"* [mm]:	0.513	0.588
Magnetising inductance L_m [mH]:	373	325
Slot-leakage inductance L_{slot} [mH]:	7.0	3.6
End winding inductance L_{end} [mH]:	5.6	5.6
Intrinsic *d*-axis inductance L_{dmi} [mH]:	21	21
Q-axis inductance $L_q = L_m + L_{slot} + L_{end}$ [mH]:	386	334
D-axis inductance $L_d = L_{dmi} + L_{slot} + L_{end}$ [mH]:	33.6	30.2

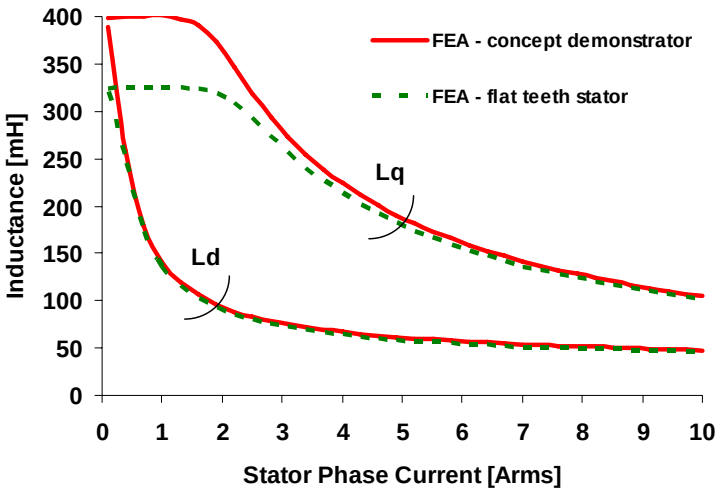

Figure 6-3 Reluctance rotor. Calculated (FEA) inductance curves for flat tooth stator and concept demonstrator.

Table 6-2 Reluctance rotor. Comparison of the obtained L_d and L_q parameters - concept demonstrator versus flat stator teeth design. The unsaturated inductances presented below are obtained for a stator current of 0.5A or less, while saturated operation corresponds to stator current of 9.4A including end-winding inductances.

Inductance [mH]:	**Conventional Teeth Stator:**			**Flat Teeth Stator:**		
	Analytical:	FEA:	Measured:	Analytical:	FEA:	Measured:
$L_{q\ (unsat)}$	380	399	355	329	324	-
$L_{q\ (sat)}$	-	104	100	-	101	-
$L_{d\ (unsat)}$	380	389	331	329	320	-
$L_{d\ (sat)}$	34	48	58	30	46	-

Firstly cutting the tips of the stator teeth increases the stator slot opening and by this means increases the Carter's coefficient (from 1.315 to 1.507 – see Table 6-1). This increase in the Carter's coefficient increases the value of the effective air gap of the machine by 15% (from 0.513 mm to 0.588 mm) and so reduces the magnetising inductance in the *q*-axis (from 373 mH to 325 mH). Secondly, cutting the tips of the stator teeth increases the width of the stator slot opening causing the slot leakage inductance to nearly halve (from 7 mH to 3.6 mH). These two effects cause a reduction in the calculated unsaturated *q*-axis inductance from 386 mH to 334 mH as shown in Figure 6-3. With increasing stator current the difference between the concept demonstrator and flat teeth designs becomes smaller due to saturation in the stator teeth.

The observed phenomenon in the *d*-axis is of a different nature. At low stator currents the rotor bridges are unsaturated and the reluctance rotor is equivalent to a solid rotor where the values of *q*- and *d*-axis inductances are similar. As the rotor bridges are narrow, they saturate very quickly as the stator current increases causing a significant drop in the *d*-axis inductance – see Figure 6-3. For the flat stator teeth design, the increase of the Carter's coefficient has little impact on the *d*-axis inductance due to the large air gap in this axis associated with the rotor magnets, however the decrease in slot leakage does cause a 10% reduction in the calculated *d*-axis inductance.

A comparison of the analytical, FEA and measured L_d and L_q parameters for the concept demonstrator versus the flat stator teeth design with a reluctance rotor was presented in Table 6-2. The finite-element and analytically obtained inductances correspond well. As was seen earlier, the measured unsaturated values for the concept demonstrator stator are slightly lower which could have been due to uncertainties in the air gap length.

An investigation of the effect of using the NdFeB rotor on the inductances in both axes is shown in Figure 6-4. It shows the FEA inductance predictions before and after compression and after the teeth were cut with the NdFeB rotor.

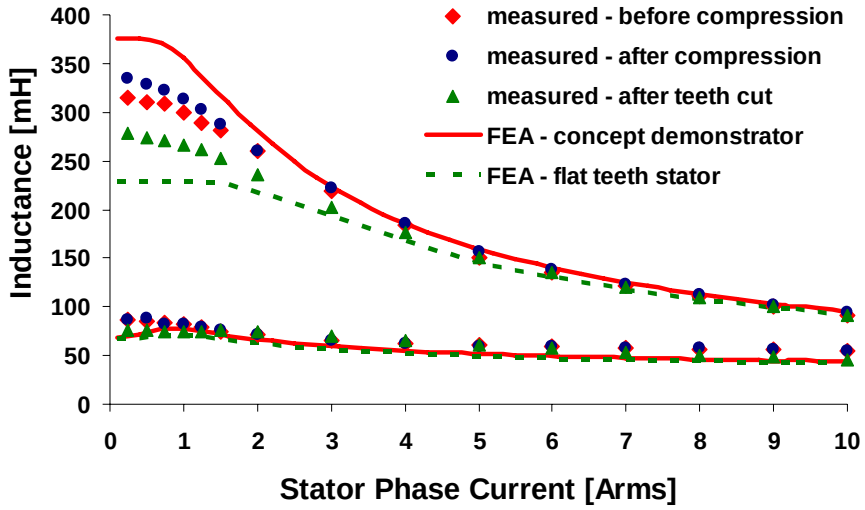

Figure 6-4 NdFeB rotor. Calculated from FEA (lines) and measured (symbols) inductance curves for flat tooth stator and concept demonstrator.

Table 6-3 NdFeB rotor. Comparison of the obtained L_d and L_q parameters - concept demonstrator (conventional teeth stator) versus flat stator teeth design. Unsaturated inductances presented below are obtained for the stator current of 0.5A or less, while saturated corresponds to the stator current of 9.4A – the end-winding inductance is not included in analytical and FEA results.

Inductances [mH]	**Conventional Teeth Stator:**			**Flat Teeth Stator:**		
	Analytical:	FEA:	Measured:	Analytical:	FEA:	Measured:
$L_{q\ (unsat)}$	380	377	312	329	228	278
$L_{q\ (sat)}$	-	97	92	-	98	92
$L_{d\ (unsat)}$	34	61	83	30	55	76
$L_{d\ (sat)}$	34	44	53	30	41	46

Compression of the stator winding pushed the stator coils towards the bottom of the stator slot and increased the slot leakage inductance and hence the *d*- and *q*-axis inductances. However the increase in the inductances after compression, particularly for the *q*-axis, is much larger than the *d*-axis. This is unexpected, as only the leakage inductance should be changed by compression and hence the increase should be the same in each axis. The observed effect is likely associated with a small reduction in the air gap due to the winding compression.

Cutting the stator tooth tips reduces both the magnetising and leakage inductances causing the *d*- and *q*-axis inductances to drop. The drop in the *q*-axis inductance is larger than the *d*-axis inductance due to the larger magnetising inductance in this axis.

The rotor magnets in the *d*-axis saturate the rotor bridges. This causes a large drop of the unsaturated *d*-axis inductances for the conventional teeth stator from 389 mH to 61 mH and for the flat teeth stator from 320 mH to 55 mH. Note that the rotor magnets have little effect on the *d*-axis inductance at high values of stator current.

The rotor magnets also produce a large value of *d*-axis flux which causes saturation of the stator teeth. This reduces the *q*-axis flux and hence produces a significant drop of the *q*–axis inductance (cross-saturation) which was discussed in Chapter 3. For the conventional teeth machine, cross-saturation causes a drop of the *q*-axis inductance from 399 mH to 377 mH. In the flat teeth stator, cross-saturation is even more significant and the inductance drops from 324 mH to 228 mH. At high currents the effect of cross-saturation is small.

6.3 Back EMF Comparison

Table 6-4 presents a comparison of the calculated and measured values of the back EMF at 1500 rpm for the new stators before compression, after compression and after the teeth were cut. Cutting the tips of the stator teeth increases the stator slot opening and hence increases Carter's coefficient. This results in an increase of the effective air gap of the machine and so reduces air gap flux density of the air gap produced by the rotor magnets. The back EMF is proportional to the rate of change of electro-magnetic flux with time and the reduced flux density will cause drop of the back EMF as has been shown in Table 6-4. The measured reduction in the back EMF (9 V) is comparable to the predicted reduction (7 V). Note, the compression of the stator winding has no impact on the value of the back EMF as expected.

Table 6-4 Comparison of the calculated and measured values of the back EMF for the new stator before compression, after compression and after teeth cut.

Back EMF [V_{rms}]:	**Method:**	
	FEA:	Measured:
Before compression:	300	273
After compression:	-	273
After teeth cut:	293	262

6.4 Search Coil Voltage and Tooth Flux Comparison

In order to measure the stator tooth flux waveforms under open- and short-circuit conditions, the search coil measurements are performed and compared to the finite element analysis results. The concept demonstrator results from Chapter 4 are reproduced for comparison purposes.

A comparison is also performed of the calculated stator teeth iron loss with the total machine iron and mechanical loss under both open and short-circuit conditions. Under open-circuit conditions, the iron and mechanical loss was obtained from the mechanical input power (using the measured input torque). Under short-circuit conditions, the iron and mechanical loss was found by subtracting the stator copper loss (determined from the measured stator current and resistance) from the mechanical input power.

6.4.1 Open-Circuit Case

Figure 6-5 and Figure 6-6 present a comparison of the calculated and measured search coil voltage and tooth flux for the concept demonstrator and flat tooth NdFeB machines under the open circuit condition at 1500 rpm (50 Hz).

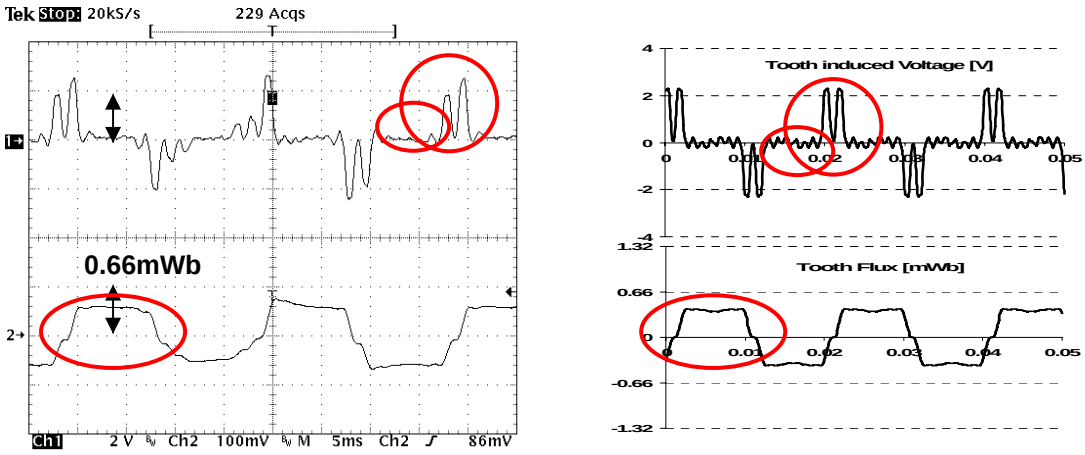

Figure 6-5 Concept demonstrator - open-circuit case. Search coil induced voltage (upper graphs) and corresponding stator tooth flux waveform (lower graphs) at 1500 rpm. (Left) measured and (right) calculated from FEA.

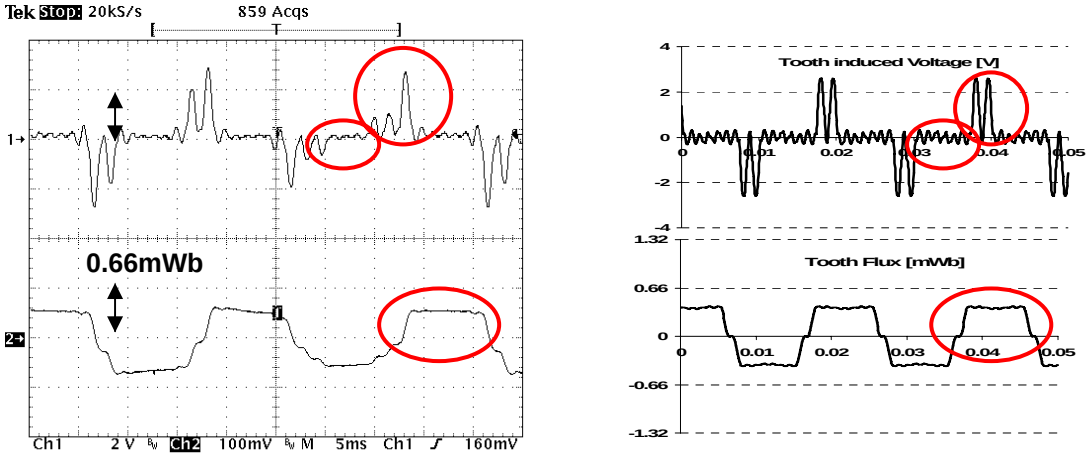

Figure 6-6 Flat teeth stator - open-circuit case. Search coil induced voltage (upper graphs) and corresponding stator tooth flux waveform (lower graphs) at 1500 rpm. (Left) measured and (right) calculated from FEA.

Under the open-circuit condition in Figure 6-5 and Figure 6-6, both measured and calculated flux waveforms are roughly rectangular but show significant asymmetry. As discussed earlier, this could be due to either an asymmetrical demagnetization/placement of the rotor magnets or local demagnetisation due to field-weakening operation. Apart from this asymmetry, the magnitudes and shapes of the calculated waveforms match well with the measured results. Note that the peak-to-peak values for the search coil flux and the tooth induced voltage waveforms (circled areas) are slightly higher in the case of the flat tooth stator construction, so the calculated FEA tooth iron loss should be higher for that case. This was confirmed with the FEA calculations presented in Figure 6-7. This figure also shows that the measured iron and mechanical losses (including the iron losses) for the entire machine - are nearly four times larger than the calculated iron losses for the stator teeth alone for both designs. This is expected due to the fact that the stator yoke has high flux densities under the open-circuit condition and as the stator yoke volume is significantly larger than the stator tooth volume.

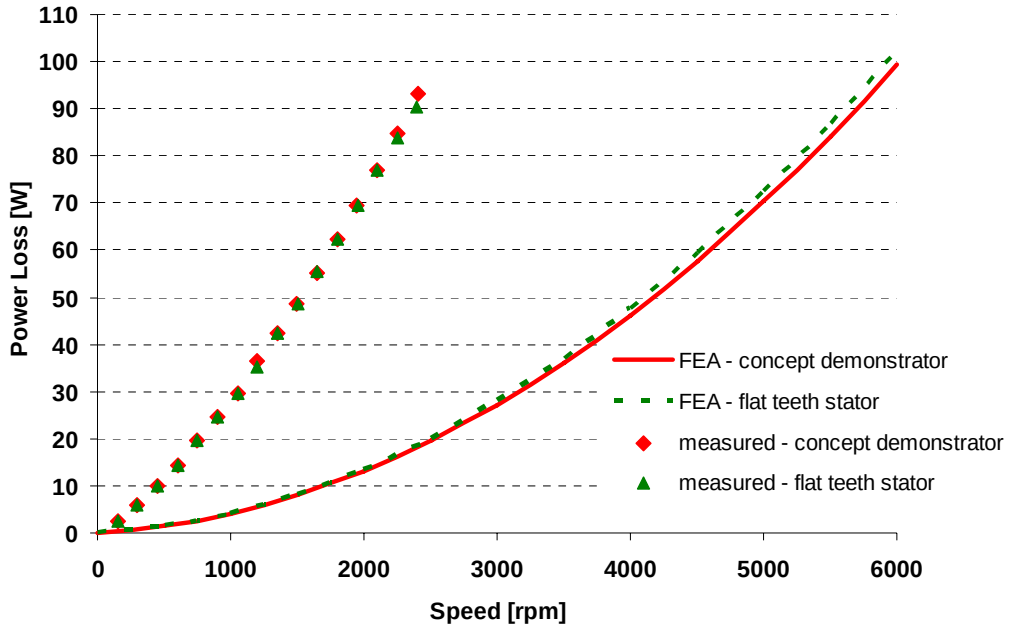

Figure 6-7 Comparison of the open-circuit losses versus speed versus finite-element predictions of stator tooth iron losses for concept demonstrator and flat teeth stator.

Figure 6-8 presents the measured open-circuit losses versus speed - before and after compression and after the teeth were cut. It is obvious that there is no significant impact on the machine open-circuit power loss due to compassion and cutting the tips of the stator tooth as it has been predicted in Figure 6-7.

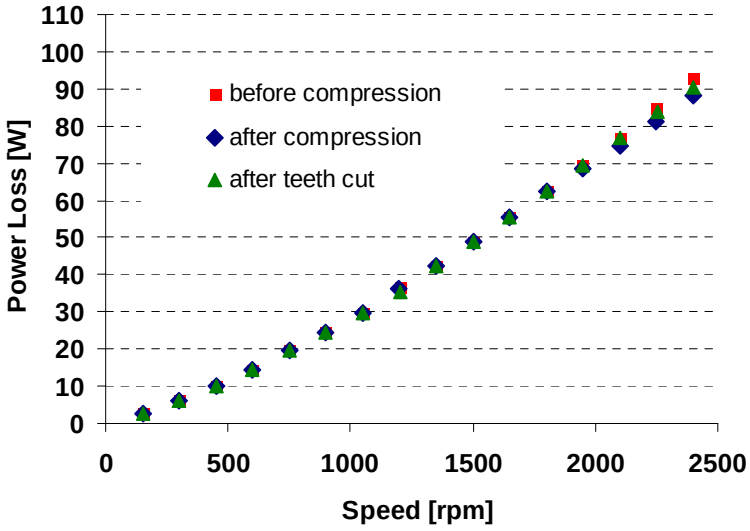

Figure 6-8 Measured open-circuit iron losses versus speed - before and after compression and after teeth cut.

6.4.2 Short-Circuit Case

Figure 6-9 and Figure 6-10 present a comparison of the calculated and measured search coil voltage and tooth flux for the flat tooth and concept demonstrator NdFeB machines under the short-circuit condition at 1500 rpm (50 Hz).

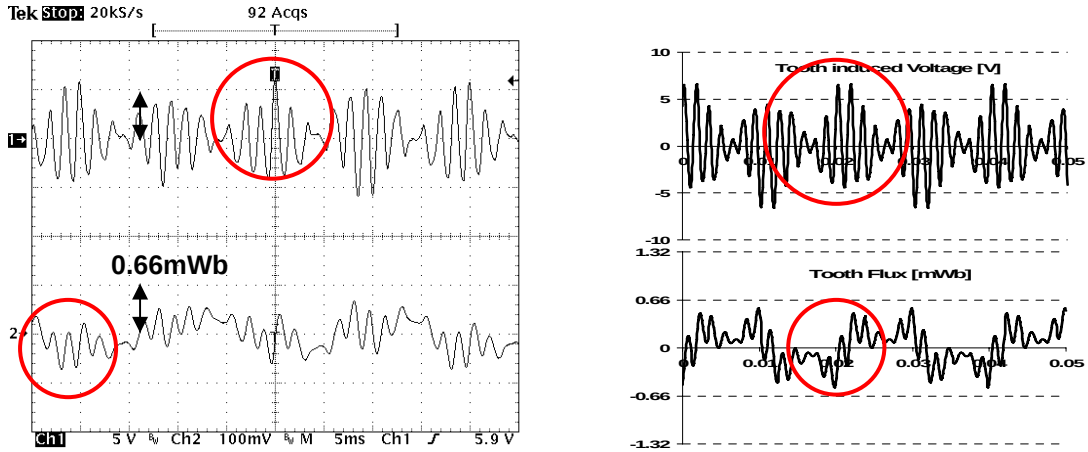

Figure 6-9 Concept demonstrator. Short-circuit case. Search coil induced voltage (upper graphs) and corresponding stator tooth flux waveform (lower graphs) at 1500 rpm. (Left) measured and (right) calculated from FEA.

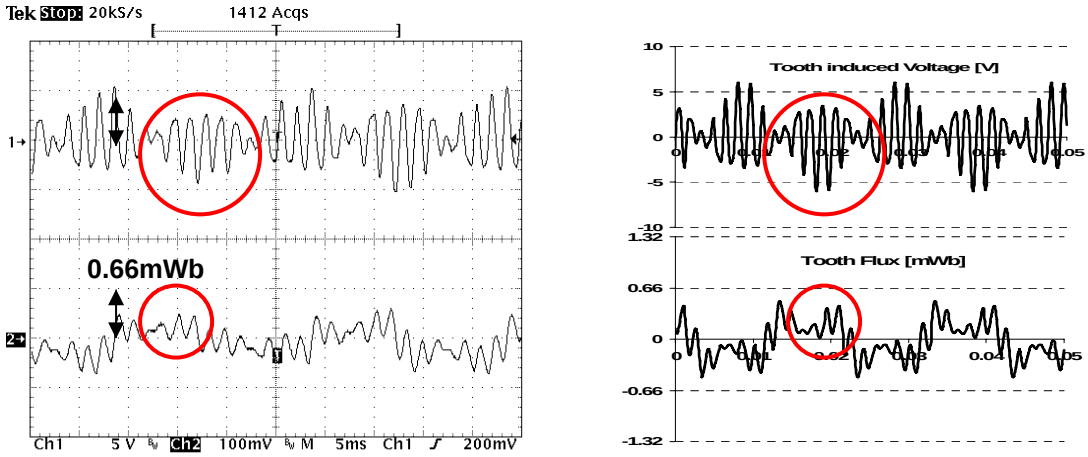

Figure 6-10 Flat stator teeth design. Short-circuit case. Search coil induced voltage (upper graphs) and corresponding stator tooth flux waveform (lower graphs) at 1500 rpm. (Left) measured and (right) calculated from FEA.

Under the short-circuit conditions presented in Figure 6-9 and Figure 6-10 ideally the fundamental component of the flux is reduced significantly compared to the open-circuit case, however the presence of large harmonic components becomes obvious. The higher the amplitude of these harmonic flux components are, the higher iron losses in stator teeth become. Once again the FEA results show a good correspondence in the magnitudes and shapes of calculated versus measured waveforms for both designs. This is confirmed in Figure 6-11 for this design both using FEA and experimentally.

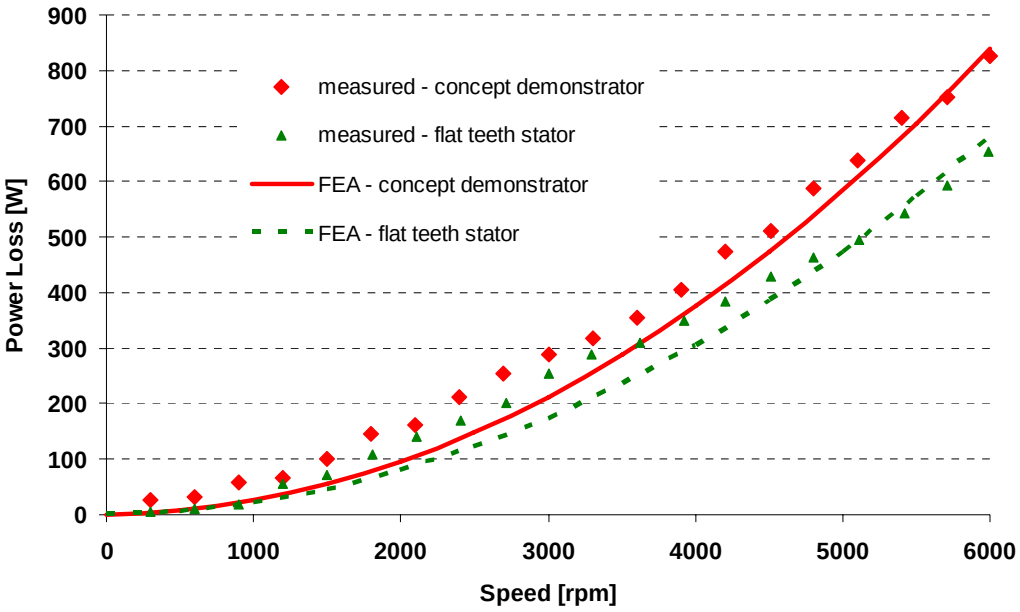

Figure 6-11 Comparison of short-circuit losses versus speed for the finite-element predictions and measurements for the concept demonstrator and flat teeth stator.

Figure 6-11 also shows that the measured short-circuit losses are very close to the calculated iron losses for the stator teeth alone for both designs. This is expected as the majority of the high stator flux density regions under the short-circuit condition are concentrated in the stator teeth. The measured short-circuit iron loss reduction is about 21% (averaged over speeds from 3000 rpm to 6000 rpm) and compares well with the final-element prediction of 19% obtained for the flat teeth compared to the conventional teeth design (concept demonstrator).

Figure 6-12 presents the measured short-circuit current versus speed - before and after compression and after the teeth were cut. It can be seen that compression of the stator winding did not cause significant change in the short-circuit current, however an increase in the short-circuit currents occurred after the teeth were cut. This could be roughly predicted as after the teeth were cut, the back-EMF dropped by 4% while the *d*-axis inductance dropped by 13%. As

the short-circuit current is proportional to the back-EMF divided by the *d*-axis inductance, so the expected increase in stator current is approximately 9%. The measured increase is 5%.

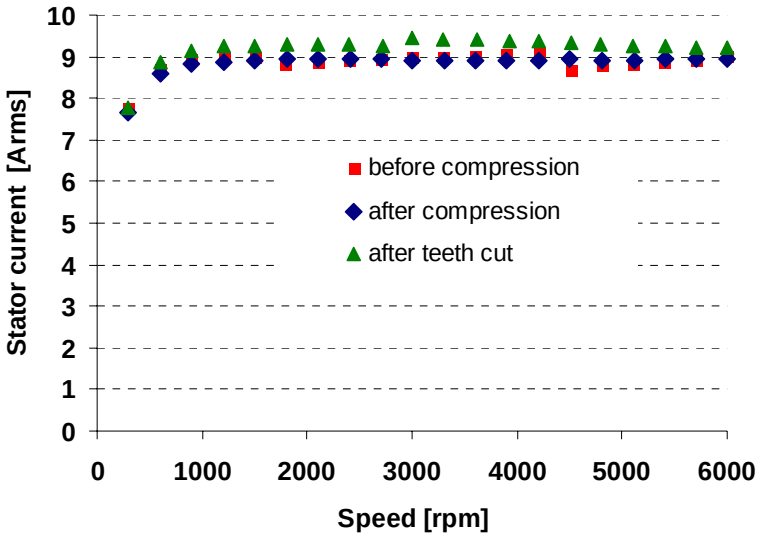

Figure 6-12 Measured short-circuit current versus speed - before and after compression and after teeth cut.

Figure 6-13 presents the measured short-circuit power loss versus speed - before and after compression and after the teeth were cut. The before compression and after the teeth cut curves were shown previously in Figure 6-11. The experimentally obtained results show that compression of the stator winding has little effect on the short-circuit power loss.

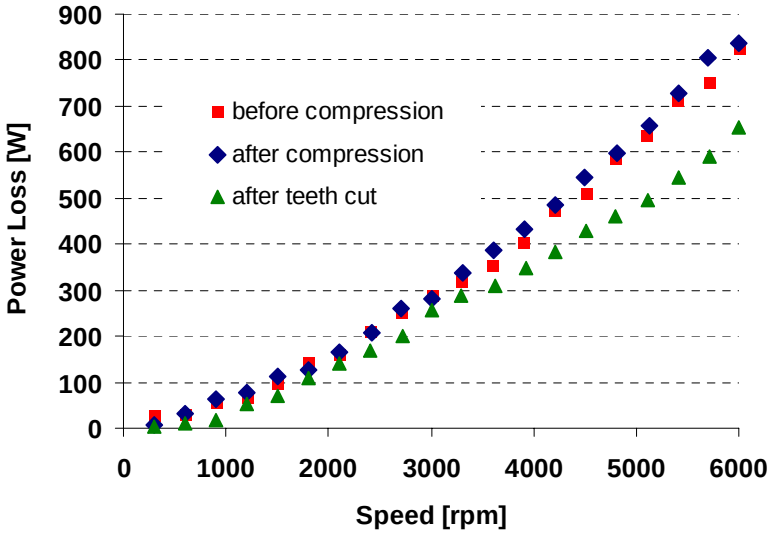

Figure 6-13 Measured short-circuit iron losses versus speed - before and after compression and after teeth cut.

The measured power output and efficiency versus speed before and after the teeth were cut are presented in Figure 6-14 and Figure 6-15. The before compression curve is not presented due to its similarity with after compression case.

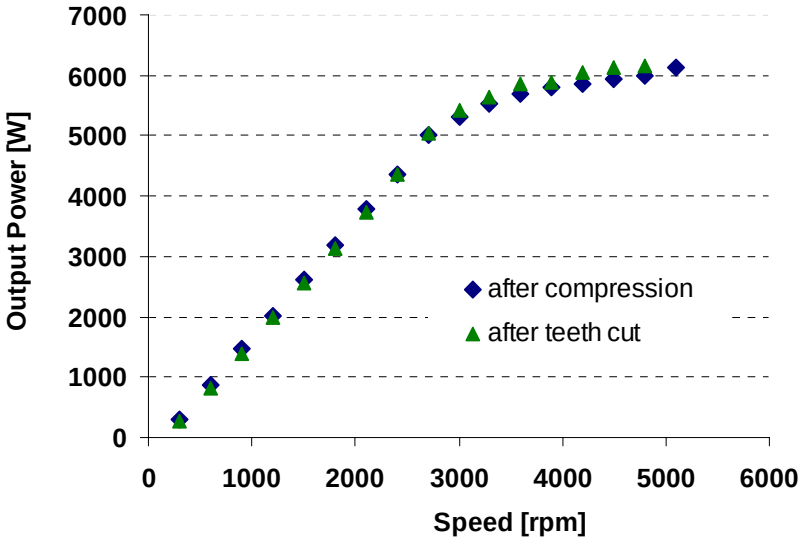

Figure 6-14 Measured power output versus speed before and after the teeth were cut.

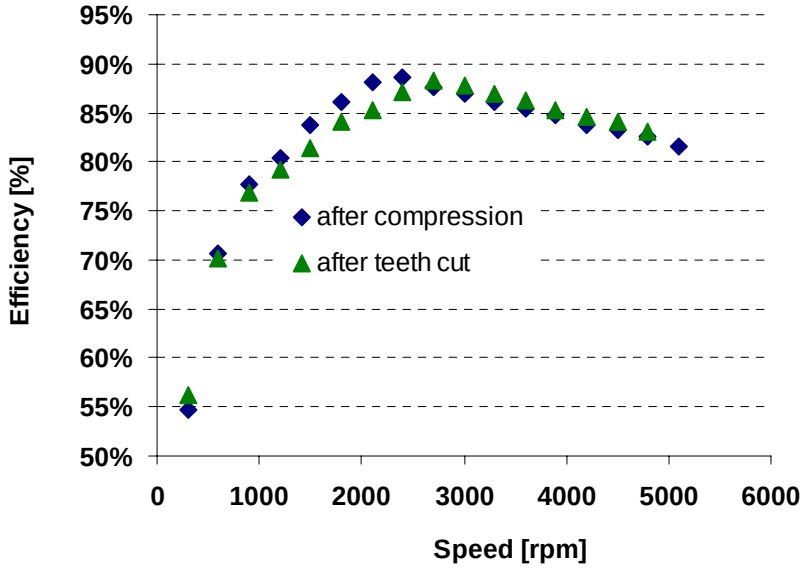

Figure 6-15 Measured efficiency versus speed before and after the teeth were cut.

For the speed range up to 2,500 rpm, the majority of the losses in the machine are caused by copper loss. For the flat teeth stator design it was experimentally confirmed that the short-circuit current increases – see Figure 6-12, so an increase in copper loss is expected. As a consequence, the total loss increases causing a slight drop in the output power and efficiency – see Figures 6-14 and 6-15. Above 2,500 rpm, the majority of the losses are the iron losses, while the copper

losses become relatively constant. It is not surprising that the reduction of the iron losses now results in slightly increased values of the output power and efficiency.

6.5 Conclusions

In order to test the concept of iron loss reduction from using flat stator teeth experimentally, the stator winding was compressed and all the stator teeth were cut. By measuring the machine performance before and after the change, it was found that the FEA calculated predictions showed a good correspondence with the measured results..

A comparison of the measured short-circuit iron losses before and after machining the stator teeth showed a reduction of about 21% (averaged over the speeds from 3000 rpm to 6000 rpm). This matched the finite-element prediction of 19%. Small improvements in the output power and efficiency at high speeds were also demonstrated.

Chapter 7 Conclusions and Findings

7.1 Background

A rare-earth 6 kW interior PM machine has been previously examined as a concept demonstrator for a high-power automotive alternator. It had been chosen due to its ability to meet the required 10:1 constant power speed range. The requirement for this particular application is a linearly increasing output power from 4 kW to a maximum of 6 kW as the alternator speed increases from an idle speed of 1.8 krpm to the maximum operating speed of 18 krpm (assuming a 3:1 belt ratio).

The machine was examined separately with a reluctance rotor and with interior PM rotors using ferrite and rare-earth magnets. For the rare-earth interior PM machine the initial experimental measurements reveal two key issues with regards to meeting the high power automotive alternator specification [43, 44]:

- Idle-speed power: at a speed of 1.8 krpm the machine was not capable of meeting the required 4 kW output power. It falls short by 14.5% (as it reaches only 3.36 kW).
- High iron losses. The measured open-circuit iron and mechanical losses at 6 krpm was around 0.8 kW. As the outer surface of the rotor is smooth, it is assumed that the major part of these losses is due to iron loss. It was found that they were not significantly affected by the output voltage and hence by the fundamental component of the flux.

These findings were the starting points for further analysis that required mathematical verification of the machine design/modelling and its performance.

7.2 Summary of Key Contributions

This thesis covers the detailed analysis of the interior PM concept demonstrator machine using finite element analysis (FEA) to examine the cause of the low idle-speed power and high iron loss. Then three changes to the concept demonstrator design were examined to reduce the iron loss in the machine. The most promising change was using flat stator teeth and the resulting iron loss reduction was experimentally verified.

7.2.1 Finite-Element Modelling and Idle Power Investigation

Due to symmetry reasons, only a quarter of the machine has been analysed. As the rare-earth magnets do not occupy the entire rotor slot area, they were modelled by reducing the magnet remanent flux density by the ratio of the magnet area to the slot area.

The finite-element model was used to predict the back-EMF magnitude and waveform and the *d*- and *q*-axis saturation curves. A good correspondence was found with the experimental results. It was found that the majority of the saturation occurred in the stator teeth. The finite-element model also predicted the presence of cross-saturation where the presence of magnet flux reduced the unsaturated *q*-axis inductance.

The measured saturation curves were used to examine the impact of saturation and cross-saturation effects on the idle-power characteristics of the rare-earth rotor machine and it was found that:

- Without saturation and cross-saturation the machine would be capable of meeting the high power alternator 4 kW idle speed requirement.
- The low speed output power was more affected by cross-saturation (6.1%) than by saturation (2.5%). Due to the non-linear nature of the phenomena, the combined effect of saturation and cross-saturation reduces the output power by 14.5%.
- The flux plots of the machine showed that the majority of saturation and cross-saturation occur in the stator teeth. Under the open-circuit condition the highest flux densities occurs in the stator teeth, in parts of the stator back iron and in some of the rotor barriers. Under the short-circuit condition the flux in the machine is much lower in general, while there are still high flux densities around the immediate vicinity of the air gap, in two stator teeth in each pole and across the rotor bridges.

7.2.2 Iron Loss Investigation

7.2.2.1 Spatial Air gap Flux Distribution

FEA was used to investigate the variation of the spatial flux density distribution to determine the cause of the high iron loss. Four cases were considered: rotor flux only, *q*-axis stator flux, *d*-axis stator flux and a combination of rotor flux and *d*-axis stator flux simulating field-weakening conditions. It was found:

- The magnets produce an air gap flux density that has a rectangular waveform of approximately peak value of 0.7 T and the dips in the waveform correspond to the stator slotting.
- The rated stator *q*-axis current of 9.4 A produces a roughly sinusoidal air gap flux distribution, which is again modulated by the stator slotting.
- The rated stator *d*-axis current of 9.4 A produces an air gap flux distribution which shows the presence of high frequency spatial harmonics. These harmonics are caused by interaction between the stator and rotor slotting. This interaction is caused by zig-zag leakage flux which occurs when stator flux crosses the air gap to the rotor and then returns back to the stator without passing through the rotor flux-barriers. This phenomenon is especially evident near 45°.
- The air gap flux density waveform with both rotor magnets and *d*-axis stator currents is nearly equal to the sum of the waveforms produced by each alone. The expected fundamental component of the sum of the two opposing fields is 0.19 T, while the actual value is 0.224 T. The higher actual value is likely to be due to greater saturation under the magnet flux only condition. The rated stator current of 9.4 A was chosen to be equal to the forced-running short-circuit current at high speeds.

7.2.2.2 Stator Tooth Flux Waveforms

FEA and experimental tests were used to examine the stator tooth flux waveform. The stator tooth flux was measured by winding search coils around the stator teeth as close as possible to the air gap. The tooth flux waveform was obtained by integrating the search coil induced voltage. The calculated and measured waveforms reveal:

- In the open-circuit case although the measured flux waveform was roughly rectangular; it also showed a significant asymmetry due to either an asymmetrical magnetization/placement of the rotor magnets or local demagnetization caused by field-weakening operation. Apart from that asymmetry, the magnitude and shape of the calculated waveforms matched well with the measured results.
- In theory the short-circuit tooth flux should be zero. In practice, the fundamental component of the tooth flux was reduced significantly compared to the open-circuit case and the higher harmonic components increased significantly in amplitude. These

components are clearly apparent in the induced voltage waveform. Again the magnitudes and shapes of the calculated waveforms matched well with the measured results.

7.2.2.3 Stator Tooth Iron Loss Calculation

The calculated tooth flux waveforms for the open-circuit and short-circuit cases were used to calculate the iron loss in the stator teeth by using two methods: *dB/dt* and Fourier series analysis. Using the *dB*/*dt* method it was found that:

- The eddy-current loss was dominant in this machine at higher speeds. At 6 krpm (200 Hz) the hysteresis loss under open-circuit conditions was around 10% of the iron loss, while under the short-circuit case it was only about 2% of the total iron loss.
- In the open-circuit condition, the measured machine iron and mechanical losses were nearly four times larger than calculated iron losses for the stator teeth only as there were high flux densities in the stator yoke.
- In the short-circuit condition, the calculated stator tooth iron losses are close to the total measured iron and mechanical losses as in this condition the highest flux densities are in the stator teeth.

An alternative method of iron loss calculation was to perform a Fourier series analysis of the FEA calculated stator tooth flux density in order to obtain the amplitude of each flux density harmonic component. Note that only odd harmonics are present due to symmetry of the waveforms. This analysis showed the following:

- Under the open-circuit condition, the tooth flux density waveform has a predominant fundamental component, while the other harmonics are relatively small in amplitude. Although the fundamental iron loss component is the largest, it only made up one third of the total eddy-current losses. The third, ninth, eleventh, thirteenth and fifteenth harmonic iron loss components are still significant. The total calculated eddy-current loss of 89W using harmonic analysis was comparable to the calculated eddy-current iron loss of 86W using the *dB/dt* method.
- As it was seen before, under the short-circuit condition, the fundamental component of the tooth flux density was halved in comparison to the open-circuit case, while the higher harmonic components increased in amplitude. The Fourier series analysis shows the thirteenth harmonic became almost comparable in magnitude to the fundamental

component. That resulted in an extremely large iron loss due to that harmonic (it caused two-thirds of the total eddy-current loss). The total calculated eddy-current loss of 900 W using harmonic analysis was comparable to the calculated eddy-current iron loss of 820 W using the *dB/dt* method.

7.2.2.4 Machine Design Change Investigation

To reduce the high stator tooth iron losses, three minor design modifications were investigated:

1. Flat stator teeth: The stator teeth geometry was changed to become flat-sided (open-slot) to reduce the zigzag leakage flux.
2. New rotor design: The shapes of the rotor barriers were modified in an attempt to improve the rotor flux distribution.
3. Ideal stator winding: a nine-phase winding was used to improve the shape of stator *d*-axis air gap flux distribution.

An investigation using FEA was performed to establish how each of these changes would affect the total iron loss under both open-circuit and short-circuit conditions. Under open-circuit conditions there were only slight differences between the open-circuit iron losses. Relative to the concept demonstrator machine, under short-circuit conditions, the ideal stator winding increases the iron loss by 3%, the new rotor reduces the iron loss by 12% and the flat stator teeth reduces iron loss the most, by 19%. The main difference between the flux distributions in these three cases was that the flux in the flat stator teeth design was more evenly distributed.

7.2.2.5 Flat Tooth Experimental Validation

In order to verify the FEA analysis, a flat tooth stator was used to experimentally obtain the iron loss measurements. This was done by firstly measuring the machine performance with conventional stator teeth, and then performing a careful machining operation (with the stator windings still in place) to open the slot openings to produce flat-sided stator teeth. This resulted in the following experimental findings:

- For the speed range between 3 krpm and 6 krpm the measured iron loss reduction of 21% was recorded and matched well with the finite-element prediction of 18.6%.

- Using flat stator teeth reduced the measured back-EMF voltage by 3.6% due to the increased Carter's coefficient and also reduced the *d*-axis inductance by 6.4% due to reduced stator slot leakage.
- A slight increase in the measured short-circuit current was also recorded which caused both slightly higher output power and copper losses.
- The output power versus speed and efficiency versus speed characteristics both improved slightly at high speeds.

It was thus found that finite element analysis was a useful tool in the parameter prediction, performance prediction and optimisation of this machine.

7.3 Influence of Work

Key results from this work include the identification of large amplitude, high order spatial harmonic airgap flux densities in this machine under field-weakening conditions. This produces large amplitude, high order harmonic components in the stator teeth and is the cause of the high iron loss. These results were first published in 2005.

The research work in this thesis significantly influenced the work done by Sam Han at the University of Wisconsin, Madison. Sam went on to develop generalised methods for selecting the rotor geometry to tailor the spatial airgap harmonic components to minimise the interaction with the stator teeth and hence the stator tooth losses [38]. He also investigated the trade-off between iron loss reduction and torque ripple minimisation in these type of machines [39]. The publication of his work, in turn, resulted in a number of other papers further investigating these topics [35, 40 ,41].

7.4 Future Work

This work did not address the idle power performance for the flat stator teeth design. Future investigation could reveal the impact of the cutting of the stator teeth on the idle power characteristics. The question of the idle power improvement could also lead to two different directions: redesigning of the machine geometry or finding appropriate solution on the power electronics control.

The work carried out in this effort relates to iron loss calculations, but was also limited by the following two assumptions:

- The calculated iron loss in the stator teeth was found to be close to the measured loss in the machine under short-circuit conditions, so the iron loss in machine was associated to the calculated stator teeth iron loss only.
- The *dB*/*dt* value was calculated as an average of the rms values of the rated change of the flux density over one cycle of the fundamental frequency in all stator teeth due to limitations of the finite-element package used.

In this effort the calculated short-circuit stator teeth iron loss results for two minor design changes show that compared to the original design, the iron loss reduces by 12% for the new rotor design and reduces by 19% with the flat teeth stator design. It would be interesting to investigate the short-circuit stator teeth iron loss reduction if both changes are applied at the same time.

More advanced finite-element packages can provide point-by-point calculations of the *dB*/*dt* in each element of the machine model. This would allow an investigation of the iron losses occurring in all parts of the machine. Future work could also consider the following paths:

- Optimisation of the machine design with regards to iron loss and torque performance [50, 51, 52].
- dynamic analysis based on a magnetic circuit modelling [53],
- electrical loss and temperature analysis [54], and/or
- mechanical design considerations [4].

References

[1] D.J. Perreault and V. Caliskan, "Automotive power generation and control," *IEEE Transactions on Power Electronics,* Volume 19, Issue 3,pp. 618 – 630, May 2004.

[2] J. G. Kassakian, H. –C. Wolf, J.M. Miller and C. J. Hurton, "Automotive electrical systems circa 2005," *IEEE Spectrum,* Volume: 33 , Issue: 8, pp. 22 – 27, 1996.

[3] W. L. Soong, N. Ertugrul, E.C. Lovelace and T.M. Jahns, "Investigation of interior permanent magnet offset-coupled automotive integrated starter/alternato," *Conference Record of the 2001 IEEE Industry Applications Conference, Thirty-Sixth IAS Annual Meeting.* Volume 1, pp. 429 – 436, 30 Sept.-4 Oct. 2001.

[4] E.C. Lovelace, T.M. Jahns, T.A. Keim and J.H. Lang, "Mechanical design considerations for conventionally laminated, high-speed, interior PM synchronous machine rotors," *IEEE Transactions on Industry Applications,* Volume 40, Issue 3, pp. 806 – 812, May-June 2004

[5] D.C. Giancoli, "Physics: Principles with applications," *5th ed., Upper Saddle River, NJ: Prentice Hall*, pp 630-631, 1998.

[6] M. Naidu and J. Walters, "A 4-kW 42-V induction-machine-based automotive power generation system with a diode bridge rectifier and a PWM inverter," *IEEE Transactions on Industry Applications,* Volume: 39 , Issue: 5, pp. 1287 – 1293, September 2003.

[7] A.L. Julian and G. Oriti, "New brushless alternator for automotive applications," *Conference Record of the 2001 IEEE Industry Applications Conference, Thirty-Sixth IAS Annual Meeting.* Volume 1, pp. 443 – 448, 30 Sept.-4 Oct. 2001.

[8] N. Schofield and S. Long, "Generator Operation of a Switched Reluctance Starter/Generator at Extended Speeds," *IEEE Transactions on Vehicular Technology*, Volume: 58 , Issue: 1, pp. 48 – 56, January 2009.

[9] A.M. EL-Refaie and T.M. Jahns, "Comparison of synchronous PM machine types for wide constant-power speed operation: converter performance," *IET Electric Power Applications*, Volume 1, Issue 2, pp. 217 – 222, March 2007.

[10] F. Caricchi, F. Crescimbini, F.G. Capponi and L. Solero, "Permanent-magnet, direct-drive, starter/alternator machine with weakened flux linkage for constant-power operation over extremely wide speed range," *Conference Record of the 2001 IEEE Industry Applications Conference, Thirty-Sixth IAS Annual Meeting*, Volume 3, pp. 1626 – 1633, 30 Sept.-4 Oct. 2001.

[11] F. Magnussen, Y.K. Chin, J. Soulard, J, A. Broddefalk, S. Eriksson and C. Sadarangani, "Iron losses in salient permanent magnet machines at field-weakening operation," *Conference Record of the 2004 IEEE Industry Applications Conference, 39th IAS Annual Meeting*, Volume 1, pp. 40 - 47, 3-7 Oct. 2004.

[12] E. C. Lovelace, "Optimization of a magnetically saturable interior permanent -magnet synchronous machine drive," *Ph.D. dissertation, Dept. Elect. Eng. Comput. Sci., University of Wisconsin-Madison,* 2000.

[13] E.C. Lovelace, T.M. Jahns and J.H. Lang, "Impact of saturation and inverter cost on interior PM synchronous machine drive optimization," *IEEE Transactions on Industry Applications*, Volume 36, Issue 3, pp. 723 – 729, May-June 2000.

[14] E.C. Lovelace, T.M. Jahns and J.H. Lang, "A saturating lumped-parameter model for an interior PM synchronous machine," *IEEE Transactions on Industry Applications*, Volume 38, Issue 3, pp 645 – 650, May-June 2002.

[15] E.C. Lovelace, T. Keim, J.H. Lang, D.D. Wentzloff, T.M. Jahns, J. Wai, and P.J. McCleer, "Design and experimental verification of a direct-drive interior PM synchronous machine using a saturable lumped-parameter model," *Conference Record of the 2002 IEEE Industry Applications Conference, 37th IAS Annual Meeting*, Volume 4, pp. 2486 – 2492, 13-18 Oct. 2002.

[16] B. Stumberger, A. Hamler and B. Hribernik, "Analysis of iron loss in interior permanent magnet synchronous motor over a wide-speed range of constant output power operation," *IEEE Transactions on Magnetics*, Volume 36, Issue 4, Part 1, pp. 1846 – 1849, July 2000.

[17] B. Stumberger, A. Hamler, M. Trlep and M. Jesenik, "Analysis of interior permanent magnet synchronous motor designed for flux weakening operation," *IEEE Transactions on Magnetics*, Volume 37, Issue 5, Part 1, pp. 3644 – 3647, Sept. 2001.

[18] B. Stumberger, G. Stumberger, M. Hadziselimovic, T. Marcic, P. Virtic, M. Trlep and V. Gorican, "Design and Finite-Element Analysis of Interior Permanent Magnet Synchronous Motor With Flux Barriers," *IEEE Transactions on Magnetics*, Volume 44, Issue 11, Part 2, pp. 4389 – 4392, Nov. 2008.

[19] W.L. Soong and N. Ertugrul, "Inverterless high-power interior permanent-magnet automotive alternator," *IEEE Transactions on Industry Applications*, Volume 40, Issue 4, pp. 1083 – 1091, July-Aug. 2004.

[20] http://www.eleceng.adelaide.edu.au/research/power/pebn/Power Engineering Briefing Note Series.pdf

[21] T. Senjyu, N. Urasaki and K. Uezato, "Influence of stator iron loss in flux weakening region for interior PMSM," *International Conference on Power Electronic Drives and Energy Systems for Industrial Growth, Proceedings 1998.* Volume 1, pp. 20 - 25 ,1-3 Dec. 1998.

[22] R. Schiferl and T.A. Lipo, "Core loss in buried magnet permanent magnet synchronous motors," *IEEE Transactions on Energy Conversion*, Volume 4, Issue 2, pp, 279 – 284, June 1989.

[23] P. Niazi,H.A. Toliyat and A. Goodarzi, " Robust Torque per Ampere (MTPA) Control of PM-Assisted SynRM for Traction Applications," *IEEE Transactions on Vehicular Technology*, Volume 56, Issue 4, Part 1, pp. 1538 – 1545, July 2007

[24] D.D. Reigosa, P. Garcia, D. Raca, F. Briz and R.D. Lorenz, "Measurement and Adaptive Decoupling of Cross-Saturation Effects and Secondary Saliencies in Sensorless Controlled IPM Synchronous Machines," *IEEE Transactions on Industry Applications*, Volume 44, Issue 6, pp. 1758 – 1767, Nov.-Dec. 2008

[25] C.E. Nino, A.R. Tariq; S. Jurkovic and E.G. Strangas, "Optimal speed control of an Interior Permanent Magnet Synchronous Motor including cross saturation," *IEEE International Electric Machines and Drives Conference, 2009. IEMDC '09,* pp. 292 – 298, 3-6 May 2009.

[26] K.J. Meessen, P. Thelin, J. Soulard and E.A. Lomonova, "Inductance Calculations of Permanent-Magnet Synchronous Machines Including Flux Change and Self- and Cross-Saturations," *IEEE Transactions on Magnetics,* Volume 44, Issue 10, pp. 2324 – 2331, Oct. 2008.

[27] J.K. Tangudu, T.M. Jahns, A. EL-Refaie and Z.Q. Zhu, "Lumped parameter magnetic circuit model for fractional-slot concentrated-winding interior permanent magnet machines," *IEEE Energy Conversion Congress and Exposition, 2009. ECCE.* Pp. 2423 – 2430, 20-24 Sept. 2009.

[28] P. Niazi and H.A. Toliyat, "On-line parameter estimation of permanent magnet assisted synchronous reluctance motor drives," *2005 IEEE International Conference on Electric Machines and Drives*, pp.1031 – 1036, May 2005.

[29] E. Armando, P. Guglielmi, G. Pellegrino, M. Pastorelli and A. Vagati, "Accurate Modeling and Performance Analysis of IPM-PMASR Motors," *IEEE Transactions on Industry Applications,* Volume 45, Issue 1, pp. 123 – 130, Jan.-Feb. 2009

[30] P. Guglielmi, M. Pastorelli and A. Vagati, " Cross saturation effects in IPM motors and related impact on zero-speed sensorless control," *Conference Record of the 2005 IEEE Industry Applications Conference, Fourtieth IAS Annual Meeting*, Volume 4, pp. 2546 – 2552, 2-6 Oct. 2005.

[31] L. Chedot, G. Friedrich, J.-M. Biedinger and P. Macret, "Integrated Starter Generator: The Need for an Optimal Design and Control Approach. Application to a Permanent Magnet Machine," *IEEE Transactions on Industry Applications*, Volume 43, Issue 2, pp. 551 – 559, March-April 2007.

[32] L. Chedot and G. Friedrich, "A cross saturation model for interior permanent magnet synchronous machine. Application to a starter-generator," *Conference Record of the 2004 IEEE Industry Applications Conference, 39th IAS Annual Meeting*, Volume 1, pp. 64-70, 3-7 Oct. 2004.

[33] J. Weigel and P. Mutschler, "Modelling and control of a permanent magnet linear synchronous motor featuring unbalance and saturation including cross-saturation," *IEEE 35th Annual Power Electronics Specialists Conference,*
Volume 3, pp. 2204 – 2210, 20-25 June 2004.

[34] B. Stumberger, G. Stumberger, D. Dolinar, A. Hamler and M. Trlep, "Evaluation of saturation and cross-magnetization effects in interior permanent-magnet synchronous motor," *IEEE Transactions on Industry Applications,* Volume 39, Issue 5, pp. 1264 – 1271 Sept.-Oct. 2003.

[35] N. Bianchi and M. Barcaro, "Iron Losses Reduction in Synchronous Motors with Anisotropic Rotor," *34th Annual Conference of IEEE Industrial Electronics -IECON 2008*, pp. 1258 – 1263, 10-13 Nov. 2008.

[36] M. Barcaro, N. Bianchi and F. Magnussen, "Rotor flux-barrier geometry design to reduce iron losses in synchronous IPM motors under FW operations," *IEEE International Electric Machines and Drives Conference, IEMDC '09.* pp. 928 – 935, 3-6 May 2009.

[37] K. Yamazaki, S. Ohki, A. Nezu and T. Ikemi, "Development of Interior Permanent Magnet Motors Reduction of Harmonic Iron Losses by Optimizing Rotor Structures," *IEEE International Electric Machines & Drives Conference, 2007. IEMDC '07*, Volume 1, pp. 489 – 494, 3-5 May 2007.

[38] S. -H. Han, W.L. Soong and T.M. Jahns, "An Analytical Design Approach for Reducing Stator Iron Losses in Interior PM Synchronous Machines During Flux-Weakening Operation," *Conference Record of the 2007 IEEE Industry Applications Conference, 2007. 42nd IAS Annual Meeting*, pp. 103 – 110, 23-27 Sept. 2007

[39] S. -H. Han, T.M. Jahns and Z. Q. Zhu, "Design Tradeoffs Between Stator Core Loss and Torque Ripple in IPM Machines," *IEEE Transactions on Industry Applications*, Volume 46, pp. 187 – 195, Issue 1, Jan.-Feb. 2010.

[40] J. –H. Seo, S. –Y. Kwak, S. –Y. Jung, C. –G. Lee, T. –K. Chung and H. –K. Jung, "A Research on Iron Loss of IPMSM With a Fractional Number of Slot Per Pole," *IEEE Transactions on Magnetics*, Volume 45, Issue 3, pp. 1824 – 1827, March 2009.

[41] G. Pellegrino, P. Guglielmi, A. Vagati and F. Villata, "Core loss and torque ripple in IPM machines: dedicated modeling and design trade off," *IEEE Energy Conversion Congress and Exposition, ECCE 2009*, pp. 1911 – 1918, 20-24 Sept. 2009.

[42] W. L. Soong, S.H. Han, T. M. Jahns and N. Ertugrul, "Reducing Iron Loss in Interior PM Machines under Field-Weakening Conditions," *42nd IAS Annual Meeting. Conference Record of the 2007 IEEE Industry Applications Conference, 2007*, pp. 111 – 118, 23-27 Sept. 2007.

[43] W. L. Soong, N. Ertugrul, E. C. Lovelace and T. M. Jahns, "Investigation of interior permanent magnet offset-coupled automotive integrated starter/alternator," *Conference Record of the 2001 IEEE Industry Applications Conference, 2001. Thirty-Sixth IAS Annual Meeting*, Volume 1, pp. 429 – 436, 30 Sept.-4 Oct. 2001.

[44] W. L. Soong and N. Ertugrul, "Field-weakening performance of interior permanent-magnet motors," *IEEE Transactions on Industry Applications*, Volume 38, Issue 5, pp. 1251 – 1258, Sept.-Oct. 2002.

[45] www.cogent-power.com

[46] W. L. Soong, "Design and modelling of axially-laminated interior PM machines," *University of Glasgow, UK, Thesis*, 1993.

[47] Cedrat, "Flux2D Version 7.60 - User's guides: Volumes: 1-7,*Cedrat, France*, November 2001.

[48] V. Gourishanker, "Electro-Mechanical Energy Conversion," *Scranton,PA: International Textbook*, 1965.

[49] J. R. Hendershot and . J. E. Miller, "Design and Performance of Brushless Permanent-Magnet Motors," *London, UK: Oxford Univ. Press*, 1994.

[50] K. Yamazaki.and H. Ishigami, "Reduction of harmonic iron losses in interior permanent magnet motors by optimization of rotor structures," *International Conference on Electrical Machines and Systems, ICEMS 2008*, pp. 2870 – 2875, 17-20 Oct. 2008.

[51] K. Yamazaki and Y. Kanou, "Rotor Loss Analysis of Interior Permanent Magnet Motors Using Combination of 2-D and 3-D Finite Element Method;" *IEEE Transactions on Magnetics*, Volume 45, Issue 3, pp. 1772 – 1775, March 2009.

[52] C. M. Siguimoto, N. Sadowski, M. Luz and C. A. Cezario, " Design and analysis of interior permanent magnet synchronous motors with optimized," *International Conference on Electrical Machines and Systems, ICEMS 2008*, Page(s):1 – 5, 6-9 Sept. 2008.

[53] K. Nakamura, K. Saito and O. Ichinokura, "Dynamic analysis of interior permanent magnet motor based on a magnetic circuit model," *IEEE Transactions on Magnetics*, Volume 39, Issue 5, Part 2, pp. 3250 – 3252, Sept. 2003.

[54] Y. Kawase, T. Yamaguchi, Z. Tu, M. Mizuno, N. Minoshima, M. Watanabe, "Electrical loss and temperature analysis of interior permanent magnet motor with divided magnets," *International Conference on Electrical Machines and Systems, ICEMS 2009*, pp. 1 – 4, 15-18 Nov. 2009.

Appendix A. Material Properties of Polycor

The following are the numerical values of the BH curve for Polycor 0.3% Si, 0.5 mm which correspond to the graph in Fig. 2-5.

H [A/m]:	B [T]:
0	0
30	0.1
41	0.2
47	0.3
53	0.4
59	0.5
65	0.6
71	0.7
78	0.8
86	0.9
94	1
104	1.1
118	1.2
140	1.3
200	1.4
370	1.5
1200	1.6
3600	1.7
7000	1.8
12000	1.9
20000	2
38000	2.1
80000	2.2
159580	2.3
239150	2.4
318730	2.5
398310	2.6

The iron loss coefficients are as follows: $C_h = 0.02094$

$C_{e1} = 1.296 \times 10^{-5}$

$a = 1.321$

$b = 0.462$

which when used in equations (4-3) and (4-10), yields an iron loss in watts per kilogram.

Appendix B. Published Papers

The following pages of this appendix include two published journal papers from this work:

1 V. Zivotic-Kukolj, W.L. Soong, N. Ertugrul, "Modelling of Saturation and Cross-saturation Effects in an Interior PM Automotive Alternator," *Australian Journal of Electrical and Electronics Engineering*, Vol 2, No 3, pp. 209 - 216, 2005.

2 V. Zivotic-Kukolj, W.L. Soong, N. Ertugrul, "Iron Loss Reduction in an Interior PM Automotive Alternator," *IEEE Transactions on Industrial Applications*, Vol 42, No 6, pp. 1478 - 1486, Nov – Dec 2006.

Zivotic-Kukolj, V., Soong, W.L. & Ertugrul, N. (2005) Modelling of Saturation and Cross-saturation Effects in an Interior PM Automotive Alternator (Conference Paper).
Australian Journal of Electrical and Electronics Engineering, v. 2(3), pp. 209 - 216

Zivotic-Kukolj, V., Soong, W.L. & Ertugrul, N. (2006) Iron Loss Reduction in an Interior PM Automotive Alternator.
IEEE Transactions on Industrial Applications, v. 42(6), pp. 1478 - 1486